Magnet Operating Point Estimation Using Flux Linkage Observer and Magnetic and Thermal Equivalent Circuit in PMSM

A DISSERTATION SUBMITTED TO THE GRADUATE
SCHOOL OF FUNCTIONAL CONTROL SYSTEMS OF
SHIBAURA INSTITUTE OF TECHNOLOGY

BY

MINHO JANG

IN PARTIAL FULFILLMENT OF THE REQUIREMENTS
FOR THE DEGREE OF

DOCTOR OF PHILOSOPHY

SEPTEMBER 2021

To my wife Mikyung
and my daughter Seoyun

Abstract

Electric vehicles (EV), which are currently being studied and interested with various cases as eco-friendly vehicles, are heavily applied with electric machines along with batteries. Many automakers adopt an interior permanent magnet synchronous motor (IPMSM) as an electric machine for EV, as it is easy to realize, higher-power density, and higher-efficiency. In addition, a variable flux interior permanent magnet synchronous motor (VF-IPMSM) with low coercive force magnet have been studied to achieve a wide speed region. To identify and control the magnetization status of the permanent magnet, a study to estimate the magnet operating point representing the current magnetization state is required.

In this study, an effective combination of methods to estimate the magnet operating points in a permanent magnet synchronous motor (PMSM) is proposed. First, a method of estimating the magnetic flux density of a permanent magnet is designed to estimate using a magnetic equivalent circuit reflecting the value of the estimated magnet temperature. Second, the proposed Flux Linkage Observer is that motor parameters can be estimated independently using the modified model reference adaptive system with additional current sampling points. Finally, the magnet temperature estimation is compensated with the estimated magnet loss based on the error between the estimated magnet temperature obtained using the thermal equivalent circuit and the estimated magnet temperature obtained using the Flux Linkage Observer. The stator iron loss is also compensated based on the error between the measured winding temperature and estimated winding temperature obtained using the thermal equivalent circuit. Unlike the rotor temperature, the stator and winding temperature can be easily measured, and the magnet operating point estimation can be designed as a more accurate and error-resistant estimation method. Furthermore, the simulation and experimental verification demonstrate the effectiveness of the proposed method.

The proposed method is relatively simple and can identify the operating point of the permanent magnet in real time. Therefore, it is expected that this study will help in terms of the protective logic design for permanent magnet and an improvement of efficiency in PMSM. In addition, using the estimated temperature and magnetic flux density of the magnet, moving the magnet operating point can improve the precision of the torque control of the motor and the efficiency of the system.

Contents

Symbol List

λ_m	: magnetic flux linkage of magnet
L_s	: motor inductance
R_s	: motor inductance
B_r	: residual magnetic flux density
B_m	: magnetic flux density of magnet
θ_m	: magnet temperature
v_{uvw}	: instantaneous values of the stator voltages in phase u, v, w, respectively
i_{uvw}	: instantaneous values of the stator current in phase u, v, w, respectively
θ_w	: measured winding temperature
$\hat{B}_m$	: estimated magnetic flux density of magnet using magnetic equivalent circuit
$\hat{\lambda}_m$	: estimated magnetic flux linkage of magnet using flux linkage observer
$\hat{\theta}_{m-FO}$	: estimated temperature of magnet using flux linkage observer
$\hat{\theta}_m$	: estimated temperature of magnet using thermal equivalent circuit
$\hat{\theta}_w$	: estimated temperature of winding using thermal equivalent circuit
Q_w, Q_{ro}	: loss values of winding and rotor core, respectively
$\hat{Q}_m$, $\hat{Q}_{st}$	: estimated loss values of magnet and stator core, respectively
$\boldsymbol{\lambda}_{\mathbf{abc}}$	: magnetic flux linkage vector in phase a, b, c, respectively
$\mathbf{v}_{\mathbf{abcs}}$	: stator voltage vector in phase a, b, c, respectively
$\mathbf{i}_{\mathbf{abcs}}$	: stator current vector in phase a, b, c, respectively
$\mathbf{T}(\boldsymbol{\theta})$	: rotational transformation matrix
v_d, v_q	: stator voltage in the d-q reference frame
i_d , i_q	: stator current in the d-q reference frame
L_d, L_q	: motor inductance in the d-q reference frame
ω_r	: motor angular speed
P_{in}	: input motor power
T_e	: motor torque
$\Re$	: the magnetic resistance
μ	: the magnetic permeability
A, l	: the area and length of the material, respectively

F_m	: the magneto-motive force (MMF) by magnet
H_e	: the coercive force of the magnet
l_m	: the length of magnet
F_w	: the magneto-motive force (MMF) by instantaneous current
N	: the number of winding turns per the teeth
i	: the instantaneous current
R_{by}	: the magnetic resistance of stator back yoke
R_{teeth}	: the magnetic resistance of stator teeth
R_{gap}	: the magnetic resistance of airgap
R_{core_d}, R_{core_q}	: the magnetic resistance of rotor core in the d-q reference frame
R_m	: the magnetic resistance of the magnet
R_{tt}	: the magnetic resistance between stator teeth and teeth
R_{cc}	: the magnetic resistance between rotor core and core
R_{FB}	: the magnetic resistance of the rotor flux barrier
P	: the magnetic permeance
$\mathbf{P}$	: the magnetic permeance matrix
$\overrightarrow{\mathbf{F}}$	: the magnetic potential (MMF) vector of the nodes
$\overrightarrow{\boldsymbol{\Phi}}_{\mathbf{s}}$	: the magnetic flux source vector
$\mathbf{P^{-1}}$	: inverse permeance matrix
$\boldsymbol{\phi_{s,w}}$	: magnetic flux source by instantaneous current of stator winding
$\boldsymbol{\phi_{s,m}}$	: magnetic flux source by permanent magnet
$\phi_{i,j}$	: the magnetic flux between nodes i and j
$B_{i,j}$	: the magnetic flux density between nodes i and j
B_{r0}	: the residual magnetic flux density of magnet at initial temperature
α_{PM}	: the temperature coefficient of residual magnetic flux density
θ_0	: initial temperature 25degC
T_s	: current sampling period time
T_1	: additional current sampling period time
$\hat{R}_s$, $\hat{L}_d$, $\hat{L}_q$, $\hat{\lambda}_m$	: estimated values of resistance, d-q inductances, flux linkage of magnet using flux linkage observer, respectively
$\mathbf{v_s}$, $\mathbf{i_s}$	: the d-q axis voltage and current vectors of applied during T_s
$\mathbf{v_{s1}}$, $\mathbf{i_{s1}}$	: the d-q axis voltage and current vectors of applied during T_1
$k_{i\_L_d}$, $k_{i\_L_q}$	: integral gains of estimated inductances

k_{i_R} , k_{i_K}	: integral gains of estimated resistance and flux linkage of magnet
ω_{LC}, ω_{RC}, ω_{KC}	: the bandwidths of estimated inductance, resistance, flux linkage of magnet
ω_{CC}	: the bandwidths of current controller
R_{sm}	: calculated resistance value at winding temperature θ_w
α_{cu}	: the temperature coefficient of copper
R_{s0}	: the initial resistance value at initial temperature θ_0
V_{dc}	: the DC link voltage
V_{an}	: the pole voltage in phase a
V_d	: the pole voltage error by dead-time
T_{on}, T_{off}	: the turn on/off delay of inverter switch
T_d	: the dead-time of inverter switch
ΔV_{an}	: the pole voltage error in command voltage and actual voltage
β_{PM}	: temperature coefficient of coercive force
H_{ci}	: the intrinsic coercive force
H_{ci0}	: the initial intrinsic coercive force at initial temperature θ_0
λ_{m0}	: the initial magnetic flux linkage of magnet at initial temperature θ_0
α_m	: the temperature coefficient of magnetic flux linkage of magnet
C_{th}	: thermal capacitance
ρ, V, c	: density, volume, specific heat, respectively
R_{cond}	: thermal resistance of conduction
k	: thermal conductivity
R_{conv}	: thermal resistance of convection
h	: convective heat transfer coefficient
V_{air}	: velocity of airflow
$\theta_{winding}$	: winding temperature
θ_{stator}	: stator core temperature
θ_{rotor}	: rotor core temperature
θ_{magnet}	: permanent magnet temperature
θ_{air}	: ambient air temperature
C_w, C_{st}, C_{ro}, C_m	: thermal capacitance of winding, stator core, rotor core and magnet, respectively
Q_w, Q_{st}, Q_{ro}, Q_m	: motor loss of winding, stator core, rotor core and magnet, respectively
$R_{winding-stator}$	: conductive thermal resistance between winding and stator core
$R_{magnet-rotor}$	: conductive thermal resistance between winding and stator core

$R_{stator-airgap}$: convective thermal resistance between stator core and airgap

$R_{rotor-airgap}$: convective thermal resistance between rotor core and airgap

$R_{winding-air}$: convective thermal resistance of winding

$R_{stator-air}$: convective thermal resistance of stator core

$R_{rotor-air}$: convective thermal resistance of rotor core

$R_{magnet-air}$: convective thermal resistance of magnet core

h_{airgap} : convective heat transfer coefficient in the air gap

N_{Nu} : Nusselt Number

l_g : length of the airgap

k_{air} : thermal conductivity of the air

N_{Ta} : Taylor Number

N_{Pr} : Prandtl Number

V_{rotor} : the velocity of rotor

v_a : the dynamic viscosity of air

c_p : the specific heat of air

$\vec{\boldsymbol{\theta}}$: the node temperature vector

$\vec{\mathbf{Q}}_{\mathbf{th}}$: the heat generation vector

$\mathbf{G}_{\mathbf{th}}$: the node conductance matrix

$\mathbf{C}_{\mathbf{th}}$: the thermal capacitance matrix

$\Delta\theta_w$: the error between the measured and estimated coil temperature

$\Delta\dot{\theta}_w$: the differential error between the measured and estimated coil temperature

$\hat{k}_{capa}$: the estimated thermal capacitance ratio

$\hat{k}_{conv}$: the estimated heat transfer coefficient ratio

g_1, g_2 : integral gains for the estimated thermal capacitance and heat transfer coefficient, respectively

w_1, w_2 : weight coefficients for the estimated thermal capacitance and heat transfer coefficient, respectively

τ : the time constant of the thermal equivalent circuit

x : the time constant ratio which is divided by time constant τ

h_{frame} : convective heat transfer coefficient of motor frame

h_{endcap} : convective heat transfer coefficient of end winding

Figure List

Table List

Chapter 1 Introduction

1.1 Research background

1.1.1 Social background

With unstable supply and demand of energy resources and growing interest in environmental issues, various industries are continuing to replace existing mechanical drives with electric drives, and research into these fields is becoming active. Miniaturization and high output of motors are essential to meet the needs of these social environments. Among the technologies that support this are motor design technology and material technology for automobiles. Various optimization techniques have been studied, and the advancement of material technologies such as electric steel plates used in motors has allowed motors to obtain higher power than in the past in a limited space. Furthermore, permanent magnets with high residual magnetic flux density have been developed and popularized, and this improvement in magnetic performance has led to active efforts to use

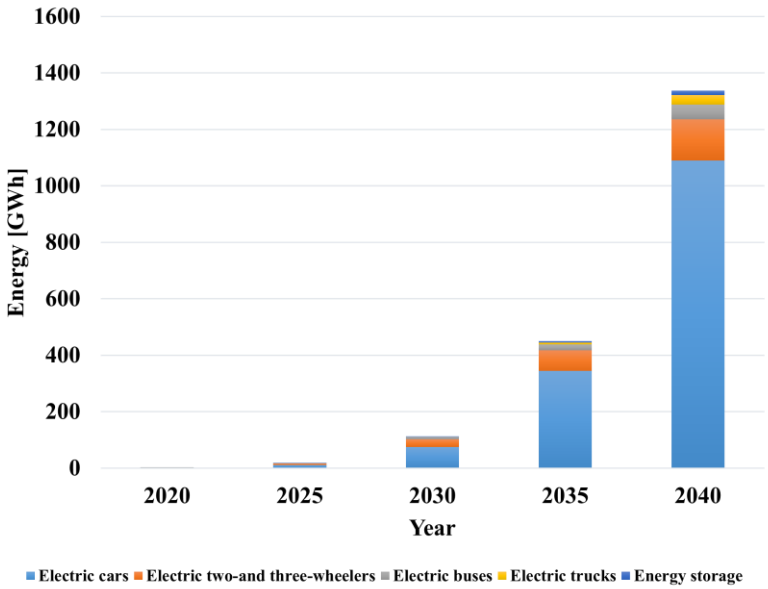

Fig. 1.1 Amount of spent lithium-ion batteries from electric vehicles and storage in the Sustainable Development Scenario, 2020-2040 [1]

permanent magnet motor systems for various purposes instead of conventional mechanical systems.

Also, as shown in the Fig. 1.1, energy consumption for lithium-ion batteries applied to electric vehicles (EV) is expected to increase significantly in the near future [1]. Therefore, electric motor vehicles require not only high torque performance but also high efficiency. Although many control methods have been studied on motor efficiency, many research on motor temperature and magnetic flux as well as control are required to obtain higher motor efficiency to be applied to EV battery systems.

1.1.2 Technical background

Electric vehicles (EV), which are currently being studied and interested with various cases as eco-friendly vehicles, are heavily applied with electric machines along with batteries [2][3]. In particular, many automakers adopt an interior permanent magnet synchronous motor (IPMSM) as an electric machine for EV, as it is easy to realize, higher-power density, and higher-efficiency than induction motors (IM) or synchronous reluctance motors (Syn. RM). In addition, a variable flux interior permanent magnet synchronous motor (VF-IPMSM) with low coercive force magnet have been studied to achieve a wide speed region [4]. The characteristics of this motor are that it can achieve an operation of a wide speed region by changing the magnet magnetization state using

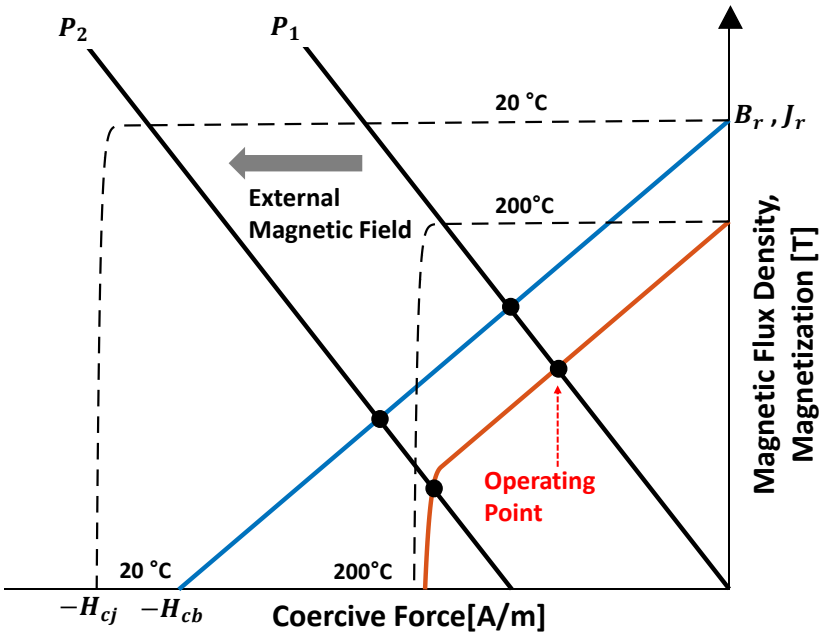

Fig. 1.2 Demagnetization phenomenon by magnet temperature and the external magnetic field

either a negative d-axis current or a positive d-axis current. In order to identify and control the magnetization status of the permanent magnet, a study to estimate the magnet operating point representing the current magnetization state is required.

As shown in Fig. 1.2, the magnet operating point represents the current state on the B-H demagnetization curve, it consists of magnetic field and flux density that is changed by the temperature of the magnet body and by the external magnetic field. The magnet operating point estimation is simplified by estimating two factors: the temperature and magnetic flux density of the magnet. Since IPMSM applied to EVs has many high-speed and high-power operating points. These operations increase the motor losses, the magnetic flux density often changes rapidly due to the high motor temperature. In the case of using a neodymium magnet, NdFeB, high temperature of magnet reduces the magnetic flux density which leads to decrease the overall efficiency of EV, and the risk of irreversible demagnetization due to the decrease of the permanent magnetic flux density by excessive temperature exists [5]-[8].

1.2 Research purpose and method

Against this background, there are three main methods to indirectly estimate the magnet temperature as shown in Table 1.1. The first is to estimate the temperature using heat transfer theory, such as the thermal equivalent circuit [9]-[13]. This method can easily estimate the temperature of the entire components of the motor. However, it requires different calculations depending on the shape or structure of the motor, and the estimated temperature error also increases with errors under initial temperature, motor loss, and convection conditions. The second method is to observe the magnetic flux linkage of permanent magnet with temperature-varying properties to estimate the temperature of the magnet [14]-[16]. It has an advantage in estimating the initial temperature and instantaneous temperature in medium to high-speed regions, without being affected by motor geometry or loss and convection conditions. However, the use of voltage equations requires precision in voltage and current information, and it effects on parameter errors such as motor resistance and inductance, as well as temperature estimation errors in low-speed region with low voltages. The third method is to estimate the temperature of the magnet using a high-frequency signal injection method [17]-[18]. It uses a method of converting high frequency impedance values that change linearly with the magnet temperature. However, there is also a limitation that must be used in a limited manner due to the additional loss caused by high frequency injection and the acoustic noise is not negligible.

Therefore, an effective combination of these methods is proposed in this paper, the temperature estimation method based on a combination of the thermal equivalent circuit and the magnetic flux observer is proposed. This proposed combination can reduce the estimated temperature error under individual initial temperature, motor losses, convection conditions. It also has the advantage of reducing the impact on the voltage error and motor parameter error at low-speed region, which are weaknesses in the flux observer method. While the temperature of the permanent magnet inserted in the rotor is not easy to measure, the fixed windings temperature can be easily measured, which is widely applied throughout the industry in the form of temperature checks and insulation protection [19]. In this paper, using this measured winding temperature, the magnet operation point estimation can be designed as a more accurate and error-resistant estimation method.

Meanwhile, various methods have been studied to estimate the magnetic flux density of permanent magnet, which is an important second factor in estimating magnet operating point. It can be divided into two main methods: finite element analysis (FEA) base and magnetic equivalent circuits base. The FEA is often used in the initial design of motors and in the

interpretation of static motor characteristics, as they have the advantage of obtaining magnetic flux relatively accurately due to their high computational capacities. Analysis based on the magnetic equivalent circuit has the advantage of being able to estimate magnetic flux in real time because it is easy to operate magnetic flux and has a small amount of computation compared to the FEA [20]-[25]. The proposed magnetic equivalent circuit reflected changes in the residual flux density according to the magnet temperature, using the temperature estimated by the thermal equivalent circuit, to consider the effect on the magnet temperature.

Fig. 1.3 shows the ideation for the magnet operating point estimation. As shown in this figure, the magnetic flux linkage of magnet, λ_m, is the most important parameter that is affected by electrical, magnetic, and thermal phenomenon. Thus, the Flux Linkage Observer is firstly used to

Table 1.1 Comparison of motor temperature estimation method

	Flux observer	**Thermal modelling**	**Impedance analysis**
Benefits	✓applicable in the entire torque range ✓permanent magnet flux value directly available ✓applicable for IPMSM and SPMSM during normal operation ✓capable of tracking magnet ageing effects	✓applicable in the entire torque and speed range ✓estimation of multiple temperatures possible ✓applicable for IPMSM and SPMSM during normal operation ✓robust against measurement and parameter variations	✓applicable in the entire torque range ✓capable of tracking magnet ageing effects ✓good performance at standstill and low speeds
Drawbacks	✓not applicable at standstill and low speeds ✓highly sensitive to measurement errors and parameter variations ✓precise inverter model or voltage measurement required	✓additional temperature sensor required (coolant or stator core) ✓ageing and irreversible demagnetization cannot be tracked	✓increases current and flux harmonics and losses ✓not applicable at high electric fundamental frequencies ✓precise inverter model or voltage measurement required ✓only SPMSM considered so far, validation only at thermal and electrical steady states

identify the magnetic flux linkage of magnet. In addition, the motor inductance, L_s, resistance, R_s, and residual magnetic flux density, B_r, are selected as parameters that combine magnetic and thermal equivalent circuits with Flux Linkage Observer. Consequently, the magnet operating point is estimated by the magnetic flux density, B_m, estimated by the magnetic equivalent circuit and the magnet temperature, θ_m, estimated by the thermal equivalent circuit.

As shown in an effective combination of methods to estimate the magnet operating points in a permanent magnet synchronous motor (PMSM) is proposed. First, a method of estimating the magnetic flux density of a permanent magnet is designed to estimate using a magnetic equivalent circuit reflecting the value of the estimated magnet temperature. Second, the proposed Flux Linkage Observer is that motor parameters can be estimated independently using the modified model reference adaptive system with additional current sampling points. Finally, the magnet temperature estimation is compensated with the estimated magnet loss based on the error between the estimated magnet temperature obtained using the thermal equivalent circuit and the estimated magnet temperature obtained using the Flux Linkage Observer. The stator iron loss is also compensated based on the error between the measured winding temperature and estimated winding temperature obtained using the thermal equivalent circuit. Unlike the rotor temperature, the stator and winding temperature can be easily measured, and the magnet operating point estimation can be designed as a more accurate and error-resistant estimation method. Furthermore,

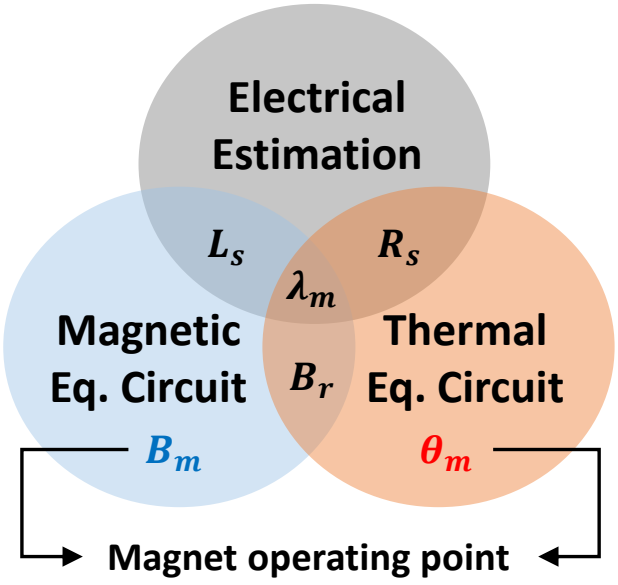

Fig. 1.3 The ideation for the magnet operating point estimation

the simulation and experimental verification demonstrate the effectiveness of the proposed method.

In this paper, Chapter 2 shows characteristic of IPMSM. Chapter 3 introduces magnetic flux density estimation using Magnetic Equivalent Circuit, and Chapter 4 describes the magnet temperature estimation using Flux Linkage Observer, and Chapter 5 magnet temperature estimation using Thermal Equivalent Circuit. Finally, Chapter 6 describes the proposed Magnet Operating Point Estimation method. The experimental results of the estimation of the operating point of the magnet according to each motor temperature condition are verified in Chapter 6. The simulation and experimental verification have been provided to demonstrate the effective-ness of the proposed method.

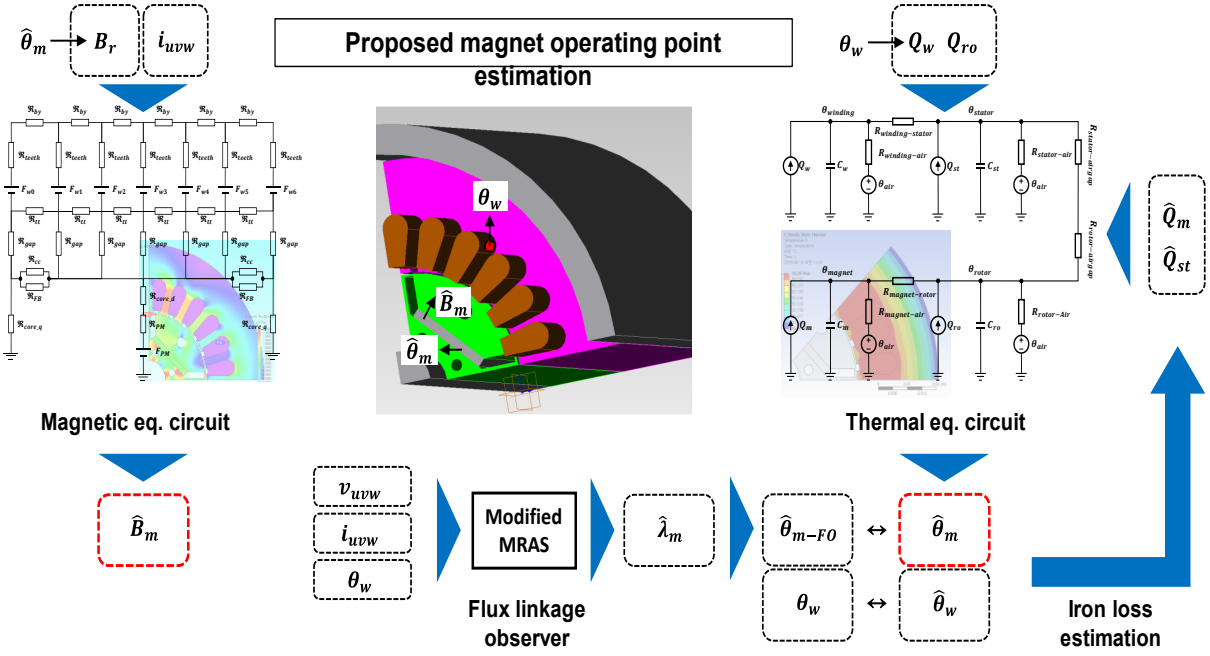

Fig. 1.4 Schmetic of the proposed magnet operating point estimation

Chapter 2 Characteristic of IPMSM

2.1 Structure of IPMSM

As shown in Fig. 2.1, Permanent Magnet Synchronous Motors are divided into Surfaced Permanent Magnet Synchronous Motor (SPMSM) with permanent magnet attached to the rotor surface and Interior Permanent Magnet Synchronous Motor (IPMSM) with permanent magnet inserted inside the rotor. The magnetic permeability of permanent magnets is almost the same as that of air in a vacuum, so the existing portion of permanent magnets is self-equivalent to the air gap. Furthermore, the magnetic reluctance of the surface magnet structure in Fig. 2.1 (a) is independent of the position of the rotor, so the d-axis inductance L_d and q-axis inductance L_q of the armature winding become the same non-saliency. However, in the inserted magnet structure of Fig. 2.1 (b), the path of the magnetic flux in the d-axis direction has a large magnetic reluctance equal to that of the air gap, which is difficult to flow, but the magnetic flux in the q-axis direction has a small magnetic reluctance to the iron core, resulting in a saliency of $L_d > L_q$ as shown in Fig. 2.2. In this case, the IPMSM has the following characteristics [26][27].

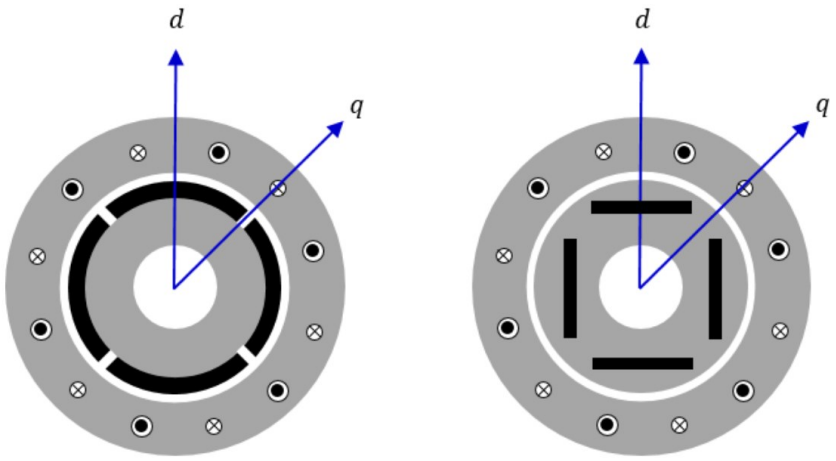

(a) SPMSM ($L_d = L_q$) (b) IPMSM ($L_d < L_q$)

Fig. 2.1 Structure of PMSM

(1) High-speed SPMSMs are equipped with non-magnetic protective tubes (SUS pipes, etc.) on the outer diameter to prevent the spread of magnets by centrifugal force, but IPMSMs are fixed inside the rotor, so mechanical strength is required, but protective tubes are not required.

(2) In a protective tube, an eddy current loss by slot ripple and a harmonic loss by carrier frequency of the inverter result in a decrease in efficiency, but in IPMSM the rotor surface is a silicon steel plate, so the problem becomes relatively small.

(3) The equivalent air gap becomes smaller in IPMSM where no protective tubes are needed, but the permeance is higher than in SPMSM when the same amount of magnet is used, thus improving the magnetic flux density of the magnet.

(4) Magnetic flux leakage from the magnetic end is generated.

(5) The degree of freedom in the shape and placement of magnets is large.

(6) SPMSM requires a magnet in the form of an arc, but IPMSM uses a magnet in the form of a flat plate to reduce production costs.

(7) Since magnetic torque and reluctance torque are used, high torque can be obtained.

(8) In IPMSM, the q-axis armature reaction is large, especially due to the large q-axis inductance compared to SPMSM, and it is likely to be affected by the rise of terminal voltage and magnetic saturation.

(9) Since magnetic salience is used, it is possible to operate sensor-less operation from the start.

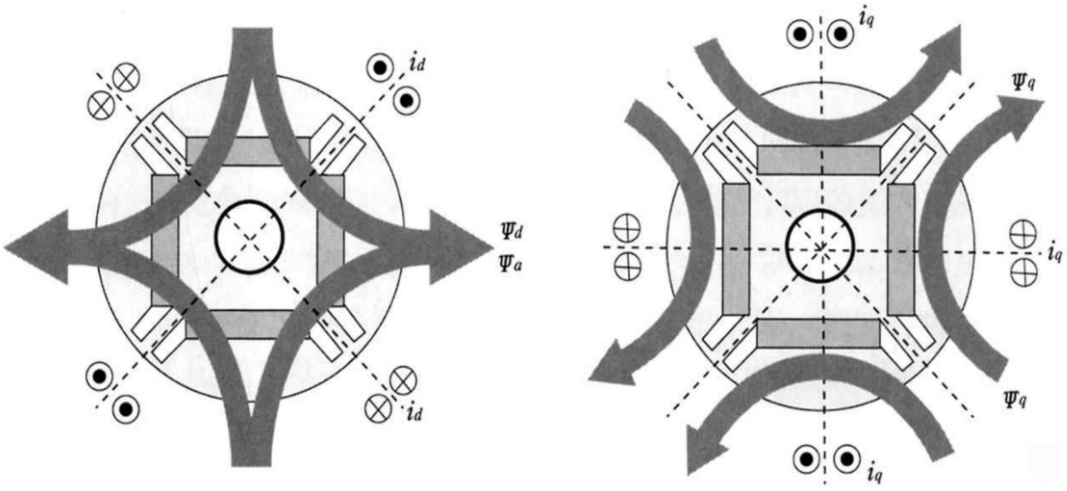

(a) Flow of the d-axis magnetic flux (b) Flow of the q-axis magnetic flux

Fig. 2.2 The d/q-axis armature reaction magnetic flux flow

In the SPMSM, magnetic reluctance does not change with respect to the rotor position, so magnetic inductance and mutual inductance are constant values. However, the flux linkage by the permanent magnet changes in a rotational angle of the rotor. Thus, in SPMSM, the torque is generated by the energy conversion caused by interaction between the flux linkage and armature. In this case, the torque is called magnetic torque. On the other hand, the magnetic inductance and mutual inductance of the IPMSM change to twice the rotation angle, and the flux linkage of the permanent magnet changes to once the rotation angle, as in the case of SPMSM. Thus, torque generation involves changes in armature magnetic inductance, mutual inductance, and the position of the flux linkage of permanent magnets.

2.2 Mathematical modeling of IPMSM

To derive the mathematical modeling of PMSM, the analysis model is defined as shown as Fig. 2.3. In this figure, the rotor is a permanent magnet, and the stator winding is electrically a three-phase Y-connection with a difference of 120 degree. The 3-phase stator winding consists of an equivalent resistance of R_s and equivalent inductance L_s, and is marked as, bs and cs, respectively. The magnetic flux linkage of each phase of the stator is defined as below,

$$\boldsymbol{\lambda}_{\mathbf{abcs}} = \boldsymbol{\lambda}_{\mathbf{abcs(s)}} + \boldsymbol{\lambda}_{\mathbf{abcs(r)}} \tag{2.1}$$

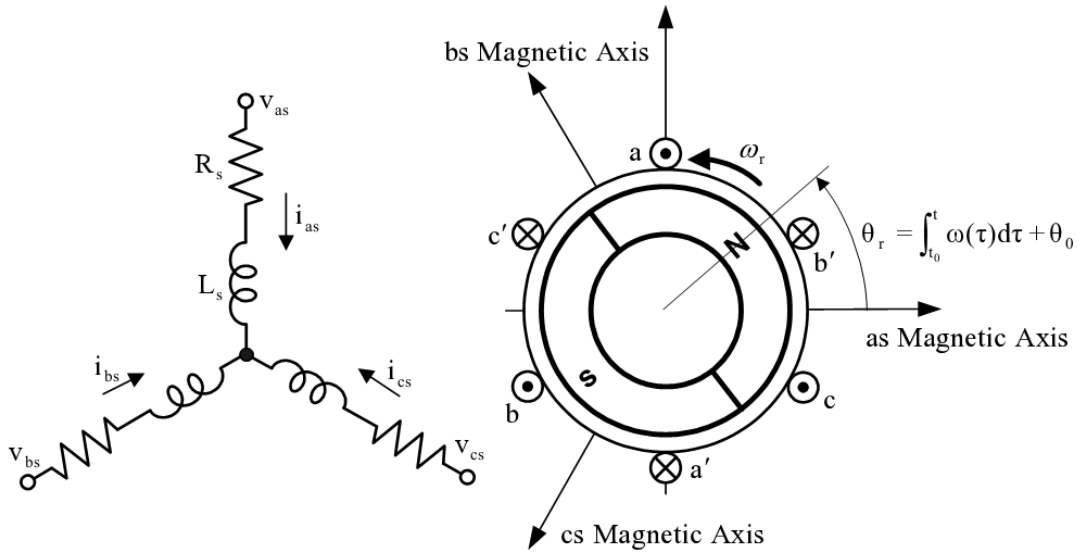

Fig. 2.3 Analysis model of PMSM

$\lambda_{abcs(s)}$ is the magnet flux linkage between stator windings, and $\lambda_{abcs(r)}$ is the magnet flux linkage between stator winding and rotor. First, the magnet flux linkage between stator windings $\lambda_{abcs(s)}$ is expressed by self-inductance and mutual-inductance, and the flux linkage by the permanent magnet $\lambda_{abcs(r)}$ changes in a rotor angle as below,

$$\begin{aligned}\boldsymbol{\lambda}_{\mathbf{abcs(s)}} &= \mathbf{L}_{\mathbf{s}} \cdot \mathbf{i}_{\mathbf{abcs}} = \begin{bmatrix} L_{aas} & L_{bas} & L_{cas} \\ L_{abs} & L_{bbs} & L_{cbs} \\ L_{acs} & L_{bcs} & L_{ccs} \end{bmatrix} \cdot \mathbf{i}_{\mathbf{abcs}} \\ &= \begin{bmatrix} L_{ls} + L_A - L_B \cos 2\theta & -\frac{L_A}{2} - L_B \cos 2\left(\theta - \frac{\pi}{3}\right) & -\frac{L_A}{2} - L_B \cos 2\left(\theta + \frac{\pi}{3}\right) \\ -\frac{L_A}{2} - L_B \cos 2\left(\theta - \frac{\pi}{3}\right) & L_{ls} + L_A - L_B \cos 2\left(\theta - \frac{2\pi}{3}\right) & -\frac{L_A}{2} - L_B \cos 2\theta \\ -\frac{L_A}{2} - L_B \cos 2\left(\theta + \frac{\pi}{3}\right) & -\frac{L_A}{2} - L_B \cos 2\theta & L_{ls} + L_A - L_B \cos 2\left(\theta + \frac{2\pi}{3}\right) \end{bmatrix} \cdot \mathbf{i}_{\mathbf{abcs}}\end{aligned} \tag{2.2}$$

$$\boldsymbol{\lambda}_{\mathbf{abcs(r)}} = \begin{bmatrix} \lambda_m \cos\theta \\ \lambda_m \cos\left(\theta - \frac{2\pi}{3}\right) \\ \lambda_m \cos\left(\theta + \frac{2\pi}{3}\right) \end{bmatrix} \tag{2.3}$$

The 3-phase voltage equation of PMSM obtained using the above flux linkage is as follows,

$$\begin{aligned}\mathbf{v}_{\mathbf{abcs}} &= R_s \cdot \mathbf{i}_{\mathbf{abcs}} + \frac{d}{dt}\boldsymbol{\lambda}_{\mathbf{abcs}} \\ &= R_s \cdot \mathbf{i}_{\mathbf{abcs}} + \frac{d}{dt}\left(\mathbf{L}_{\mathbf{s}} \cdot \mathbf{i}_{\mathbf{abcs}} + \boldsymbol{\lambda}_{\mathbf{abcs(r)}}\right)\end{aligned} \tag{2.4}$$

The reactance of a synchronous motor is a function of the motor speed, so it appears in the form of a time-variant differential equation except when the motor is stationary. Therefore, it is simple and easy to analysis by converting a 3-phase reference frame into a 2-phase reference frame using the transformation matrix $\mathbf{T}(\boldsymbol{\theta})$. Typical 2-phase coordinate systems are divided into 2-phase stationary frame based on the stator side and 2-phase synchronous frame based on the rotor rotating at the synchronous speed.

The transformation matrix is defined as below,

$$\mathbf{T}(\boldsymbol{\theta}) = \frac{2}{3}\begin{bmatrix} \cos\theta & \cos\left(\theta - \frac{2\pi}{3}\right) & \cos\left(\theta + \frac{2\pi}{3}\right) \\ -\sin\theta & -\sin\left(\theta - \frac{2\pi}{3}\right) & -\sin\left(\theta + \frac{2\pi}{3}\right) \\ \frac{1}{\sqrt{2}} & \frac{1}{\sqrt{2}} & \frac{1}{\sqrt{2}} \end{bmatrix} \tag{2.5}$$

Finally, the voltage equation in the d-q synchronous frame is represented by transformation matrix $\mathbf{T}(\boldsymbol{\theta})$

$$\mathbf{T}(\boldsymbol{\theta}) \cdot \mathbf{v}_{\mathbf{abcs}} = \mathbf{T}(\boldsymbol{\theta}) \cdot R_s \cdot \mathbf{i}_{\mathbf{abcs}} + \mathbf{T}(\boldsymbol{\theta}) \cdot \frac{d}{dt}\boldsymbol{\lambda}_{\mathbf{abcs}} \tag{2.6}$$

$$\begin{bmatrix} v_{ds}^r \\ v_{qs}^r \end{bmatrix} = \begin{bmatrix} v_d \\ v_q \end{bmatrix} = \begin{bmatrix} R_s + L_d p & -L_q \omega_r \\ L_d \omega_r & R_s + L_q p \end{bmatrix} \begin{bmatrix} i_d \\ i_q \end{bmatrix} - \begin{bmatrix} 0 \\ \lambda_m \omega_r \end{bmatrix} \tag{2.7}$$

Where v_d, v_q , i_d and i_q are the average voltage and current of the d-q axis respectively applied during the sampling period, and ω_r is the angular velocity of the rotor, p is differentiation for time, R_s is the resistance of the coil, L_d and L_q are the inductance of the d-q axis, and λ_m is the magnetic flux linkage by the magnet.

The torque equation of the synchronous motor can be obtained from the output of the motor. The instantaneous input power by a three-phase input is P_{in}, the value is as shown as below,

$$P_{in} = v_{as}\, i_{as} + v_{bs}\, i_{bs} + v_{cs}\, i_{cs} \tag{2.8}$$

Using transformation matrix $\mathbf{T}(\boldsymbol{\theta})$**,** the instantaneous input power P_{in} is defined in the d-q synchronous frame as below,

$$P_{in} = \frac{3}{2}\left(v_d\, i_d + v_q\, i_q\right) = \frac{3}{2}\left[R_s\left(i_d^{\,2} + i_q^{\,2}\right) + \frac{L_s}{2}\frac{d}{dt}\left(i_d^{\,2} + i_q^{\,2}\right) + \lambda_m \omega_r i_q \right] \tag{2.9}$$

Where P is the number of poles, the torque equation of PMSM is as below [28],

$$T_e = \frac{3}{2}\frac{P}{2}\left(\lambda_m i_q + \left(L_d - L_q\right) i_d i_q\right) \tag{2.10}$$

Chapter 3 Magnetic flux density estimation using Magnetic Equivalent Circuit

In this chapter, proposed magnetic equivalent circuit has been introduced. Analysis based on the magnetic equivalent circuit has the advantage of being able to estimate magnetic flux in real time because it is easy to calculate magnetic flux and has a small amount of computation compared to the FEA. The proposed magnetic equivalent circuit reflected changes in the residual flux density according to the magnet temperature, which is estimated by the thermal equivalent circuit, to consider the effect on the magnet temperature.

3.1 Magnetic Equivalent Circuit

To estimate the magnet operating point, the magnetic flux density of permanent magnet must be calculated. In this paper, the magnetic equivalent circuit, MEC, which allows the calculation of magnetic flux in real-time, is used thanks to the advantage of less computation than the finite elements analysis, FEA [20]-[25]. The magnetic equivalent circuit consists of the magnetic resistances and the magneto-motive forces, MMF. IPMSM has been selected for verifying the

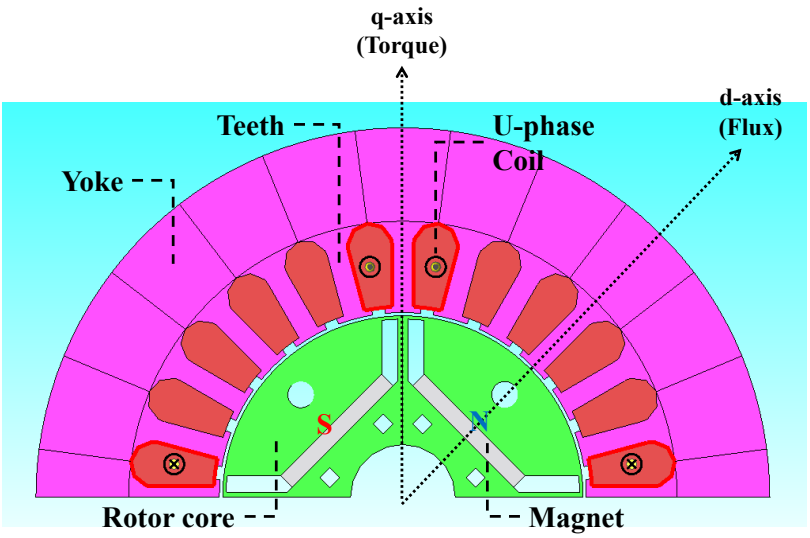

Fig. 3.1 Interior Permanent Magnet Synchronous Motor

proposed method as shown in Fig. 3.1 and the proposed magnetic equivalent circuit is shown in Fig. 3.2. Each value is calculated as following equations.

$$\Re = \frac{l}{\mu \cdot A} \tag{3.1}$$

$$F_m = H_e \cdot l_m \tag{3.2}$$

$$F_w = \sum N \cdot i \tag{3.3}$$

where $\Re$ is the magnetic resistance, μ is the magnetic permeability, A is the area and l is the length of the material, F_m is the MMF of the magnet, H_e is the coercive force of the magnet, l_m

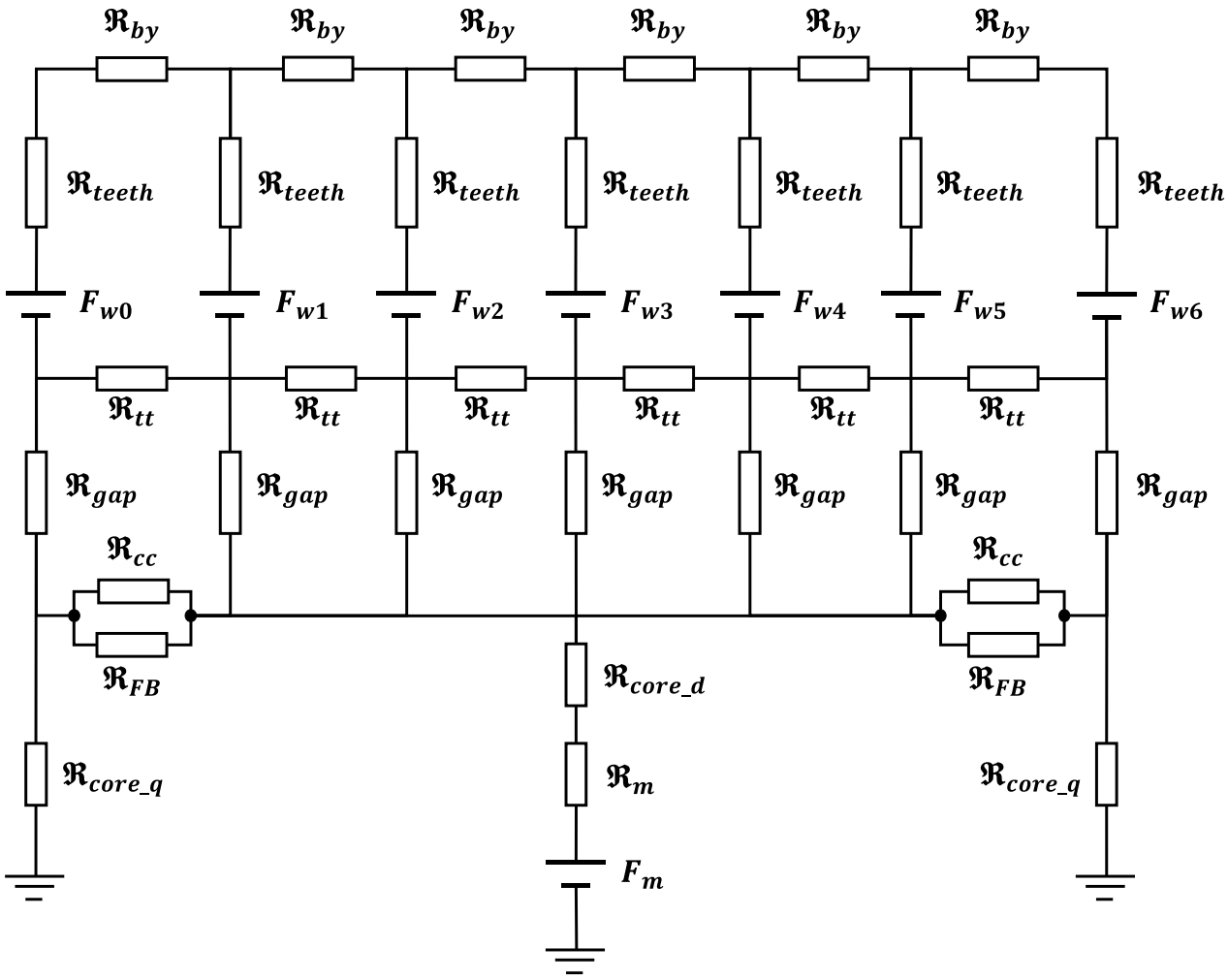

Fig. 3.2 Magnetic Equivalent Circuit for IPMSM

is the length of the magnet, F_w is the MMF by the flowing current to the armature winding, N is the number of winding turns per the teeth, i is the instantaneous current. R_{by} is the magnetic resistance of stator back yoke, and R_{teeth} is that of stator teeth, and R_{gap} is that of airgap. R_{core_d} and R_{core_q} are the magnetic resistance of rotor core in the d-q reference frame, and R_m is that of the magnet. In magnetic resistance of the angular direction, R_{tt} is the magnetic resistance between stator teeth and teeth, R_{cc} is the magnetic resistance between rotor core and core, and R_{FB} is the magnetic resistance of the rotor flux barrier.

3.2 Calculation of Magnetic Flux Density

To reduce the number of nodes, as shown in Fig. 3.3, a MMF source can be substituted by an equivalent magnetic flux source. To solve this circuit in real time, it is converted to the following matrix using Nodal analysis.

$$\mathrm{P} = \frac{1}{\Re} = \frac{\mu \cdot A}{l} \tag{3.4}$$

$$\mathbf{P} \times \vec{\mathbf{F}} = \vec{\mathbf{\Phi}}_{\mathbf{s}} \tag{3.5}$$

$$\vec{\mathbf{F}} = \mathbf{P}^{-1} \times \vec{\mathbf{\Phi}}_{\mathbf{s}} \tag{3.6}$$

where P is the magnetic permeance, $\mathbf{P}$ is the permeance matrix, $\vec{\mathbf{F}}$ is the magnetic potential (MMF) vector of the nodes, and $\vec{\mathbf{\Phi}}_{\mathbf{s}}$ is the magnetic flux source vector.

The magnetic equivalent circuit can be mathematically converted into a matrix equation through the Nodal-analysis. In other words, it can be easily interpreted using Laws of KVL and KCL in electrical circuits. The magnetic flux density is calculated to solve inverse permeance matrix $\mathbf{P^{-1}}$ and solving magnetic potential and flux values. To solve this inverse matrix $\mathbf{P^{-1}}$, the

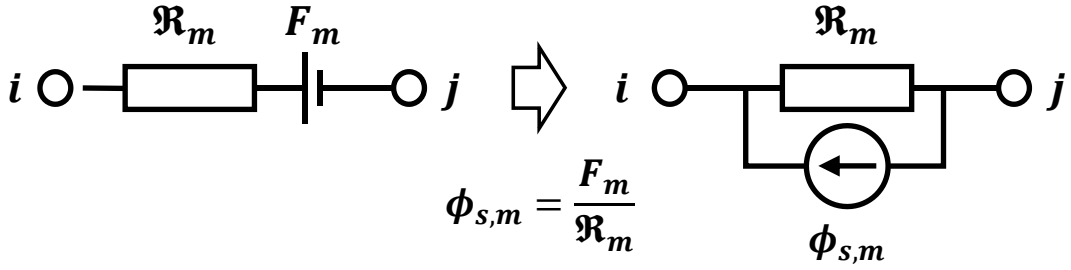

Fig. 3.3 Transformation for reduction of the number of nodes

direct inverse matrix solution, Gauss-Jordan elimination method, which is generally used when there are fewer nodes, are used, whereas when there are many nodes and complex calculations are required, Gauss-Seidel methods are used using repetition and residuals. In this paper, the number of nodes is 14, which is relatively small, so the Gaussian method is used.

In this equation, the inverse operation of the permeance matrix allows the magnetic potential value of each node, and the magnetic flux and magnetic flux density of each branch are obtained by the following equation.

$$\phi_{i,j} = P_{ij} \times \left(F_j - F_i \right) + \phi_S \tag{3.7}$$

$$B_{i,j} = \frac{\phi_{i,j}}{A_{ij}} \tag{3.8}$$

where $\phi_{i,j}$ is the magnetic flux and $B_{i,j}$ is the magnetic flux density between nodes i and j.

As shown Fig. 3.4 (a), the iron core, which is usually applied to stator and rotor of the IPMSM, has nonlinear properties. It is important to note here that the magnetic permeability of the core, μ, is not a fixed value, but rather a nonlinear value that varies with the magnetic flux density value on the B-H curve of iron core. The magnetic permeability of each node depends on the flux density of that node. Obtaining the permeability of a node as a function of magnetic flux density requires a data table or a regression equation of relative permeability.

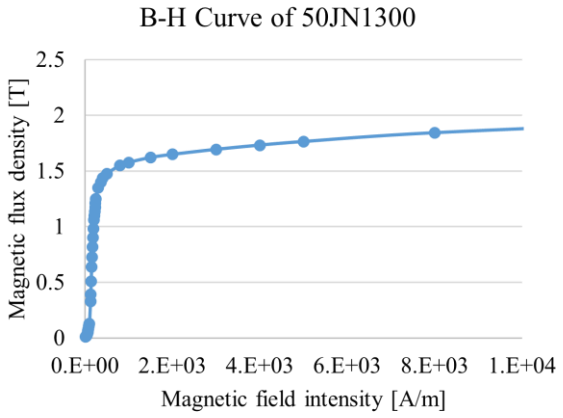

(a) B-H Curve of iron core

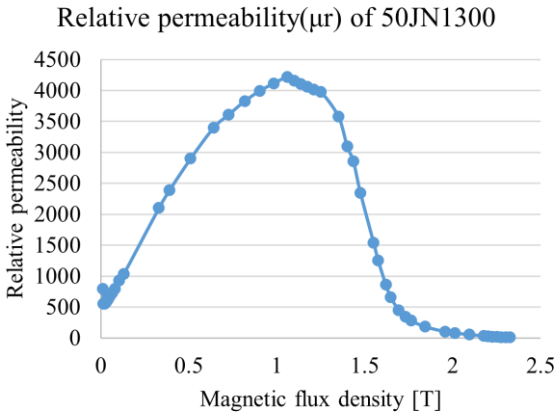

(b) Relative magnetic permeability of iron core

Fig. 3.4 Magnetic permeability of the stator and rotor core

$$\mu = B / H \tag{3.9}$$

The magnetic permeability is obtained through k+1 iteration. Therefore, it is calculated repeatedly to satisfy the reference residual error, ε, that set the magnetic flux density and permeability of the core.

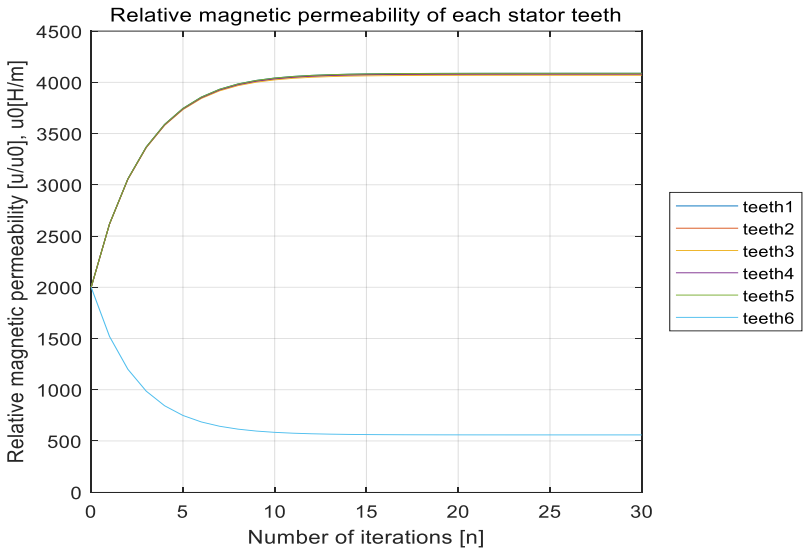

(a) Relative permeability of stator teeth

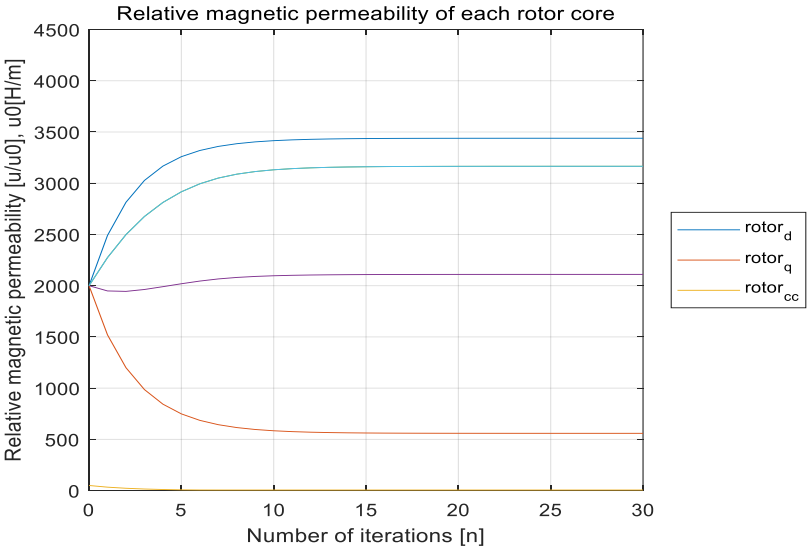

(b) Relative permeability of rotor core

Fig. 3.5 Iterative calculation of magnetic permeability, no load

$$\left|\frac{\mu^{k}-\mu^{k-1}}{\mu^{k-1}}\right| \le \varepsilon \tag{3.10}$$

For the IPMSM model applied in this paper, the value of the magnetic permeability converges to a constant value when the number of iterations is 15 or higher as shown Fig. 3.4 (b). Finally, the magnetic flux density of a permanent magnet, a component of the operating point of a permanent magnet, may be obtained as follows,

$$B_m = \frac{\phi_m}{A_m} \tag{3.11}$$

where B_m is the magnetic flux density of magnet, ϕ_m is the magnetic flux of magnet and A_m is the area of magnet.

The block diagram of magnetic flux density Estimation using MEC is shown in Fig. 3.6 . To analysis the proposed magnetic equivalent circuit, the following sequences are required:

(1) Solve the inverse of the obtained magnetic permeance matrix $\mathbf{P^{-1}}$.

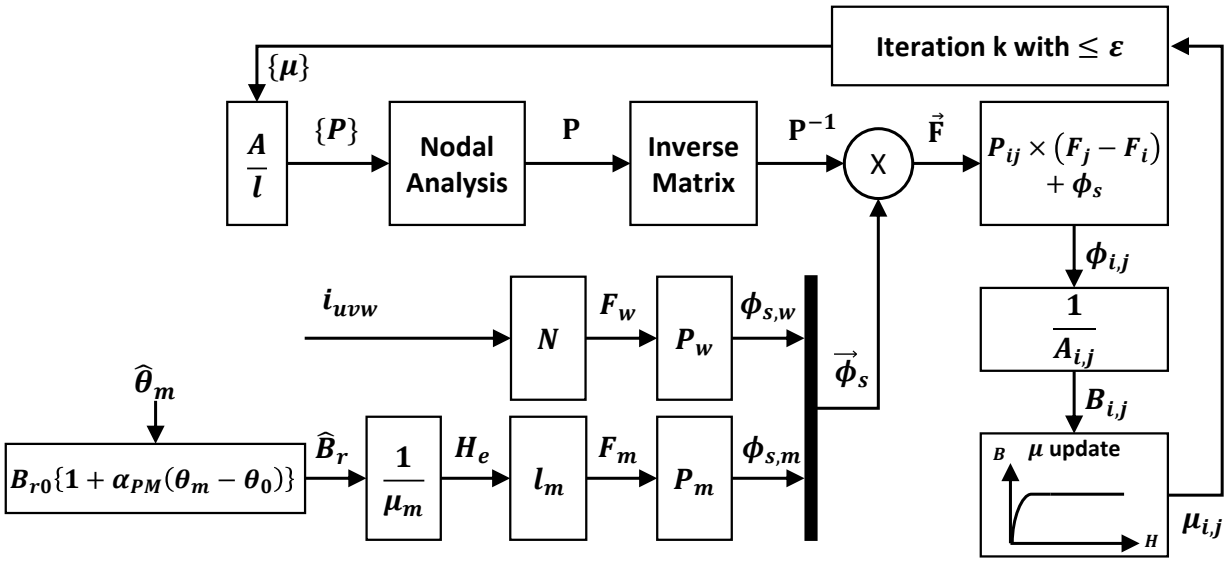

Fig. 3.6 Magnetic flux density Estimation using MEC

(2) Convert to magnetic flux source by instantaneous current of stator winding $\boldsymbol{\phi_{s,w}}$.

(3) Convert to magnetic flux source by permanent magnet $\boldsymbol{\phi_{s,m}}$ using the residual flux density $\boldsymbol{B_r}$ changed by the magnet temperature $\widehat{\boldsymbol{\theta}}_{\boldsymbol{m}}$. (The estimated temperature is used in this paper)

(4) Magnetic potential of each node $\overrightarrow{\mathbf{F}}$ is obtained by multiplying the magnetic flux source vector $\overrightarrow{\boldsymbol{\Phi}}_{\mathbf{s}}$ by the inverse permeance matrix $\mathbf{P^{-1}}$.

(5) Calculate the magnetic flux $\phi_{i,j}$ and the magnetic flux density $B_{i,j}$ flowing through each branch.

(6) Determine the magnetic permeability $\mu_{i,j}$ according to this magnetic flux density $B_{i,j}$ (using the B-H curve of the stator core and rotor core).

(7) Recalculate the magnetic permanence matrix $\mathbf{P}$ using the magnetic permeability obtained $\{\mu\}$.

(8) Repeat 1 to 7 until the residuals of magnetic permeability are satisfied.

where B_{r0} is the residual magnetic flux density of magnet at initial temperature, α_{PM} is the temperature coefficient of residual magnetic flux density, θ_m is the magnet temperature and θ_0 is the initial temperature 25degC.

3.3 Calculation of Motor Inductances

Another advantage of the magnetic equivalent circuit is that it can calculate the motor inductances L_{dq} and the magnetic flux linkage of magnet λ_m. Therefore, motor parameters highly influenced by magnetic flux saturation, such as inductances, can be reflected in control or observer block. The motor inductances reflecting the saturation of iron cores can be obtained using the superposition of the magnetic flux sources in stator windings $\boldsymbol{\phi_{s,w}}$ and permanent magnet $\boldsymbol{\phi_{s,m}}$. As shown in Fig. 3.7, the magnetic flux source of the magnet $\boldsymbol{\phi_{s,m}}$ is removed from the magnetic flux source vector and the d-q axis inductances are obtained from following equation.

$$L_{dq} = \frac{N\phi_{dq}}{i_{dq}} = \frac{\lambda_{dq}}{i_{dq}} \tag{3.12}$$

where L_{dq} are the d-q axis inductances, ϕ_{dq} is the d-q axis magnetic flux, λ_{dq} are the d-q axis flux linkage and i_{dq} are the d-q axis current.

It should be noted that if motor current is zero, inductance calculation is not possible and the minimum current value for the calculation must be determined. Usually, even if the current is zero under no-load conditions, the ripple component of the current exists. Therefore, the minimum current value for inductance calculation can be determined as the ripple value of the motor control current. In this paper, the minimum current value is selected as 0.1A. Another consideration is the skin effect on the stator windings when calculating inductance. The skin effect is the property of an electric current flowing outside the conductor as frequency increases. This skin effect can increase the resistance and inductance of stator windings. However, it is not easy to consider it because magnetic equivalent circuit is simply lump-type calculations. This is the limit of magnetic equivalent circuit.

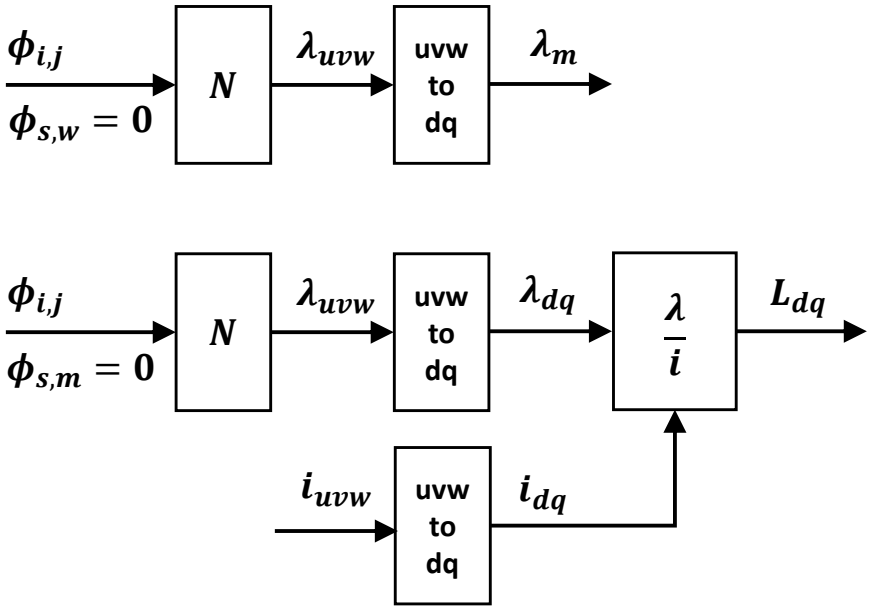

Fig. 3.7 Estimated inductances and magnetic flux linkage using MEC

3.4 Simulation result of Magnetic Equivalent Circuit

To validate the proposed magnetic equivalent circuit for IPMSM, the comparison between the FEA (JMAG®) and MEC results of the 3-phase magnetic flux linkages are shown in Fig. 3.8. The simulation results have been compared under conditions with a speed of 1500 min^{-1}, current 5A and current angle 25deg. The error of magnitude and angle has been found to be acceptably small. Therefore, the effectiveness of the proposed magnetic equivalent circuit, which is called MEC in this paper, has been demonstrated.

The comparison of d-q axis inductances estimation results between FEA and MEC as shown in Fig. 3.9. The simulation results have been compared under conditions with a speed of 1500 min^{-1}, current 1 to 9A and current angle 5 / 25 / 45deg. As shown in this result, the magnetic flux saturation of the iron core decreases the q-axis inductance as the current increases. The higher current and the higher speed, the greater the impact on inductances, so it is important to reflect the exact inductance value in the estimation of the magnetic flux linkage.

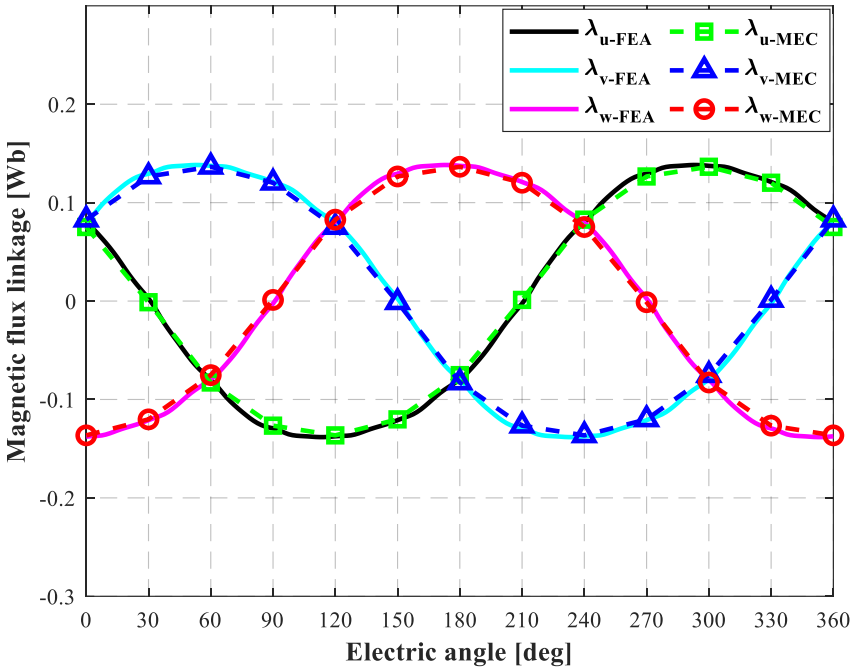

Fig. 3.8 The comparison of results between the FEA and MEC of the 3-phase flux linkages, Current 5A, Current angle 25deg at 1500 min^{-1}

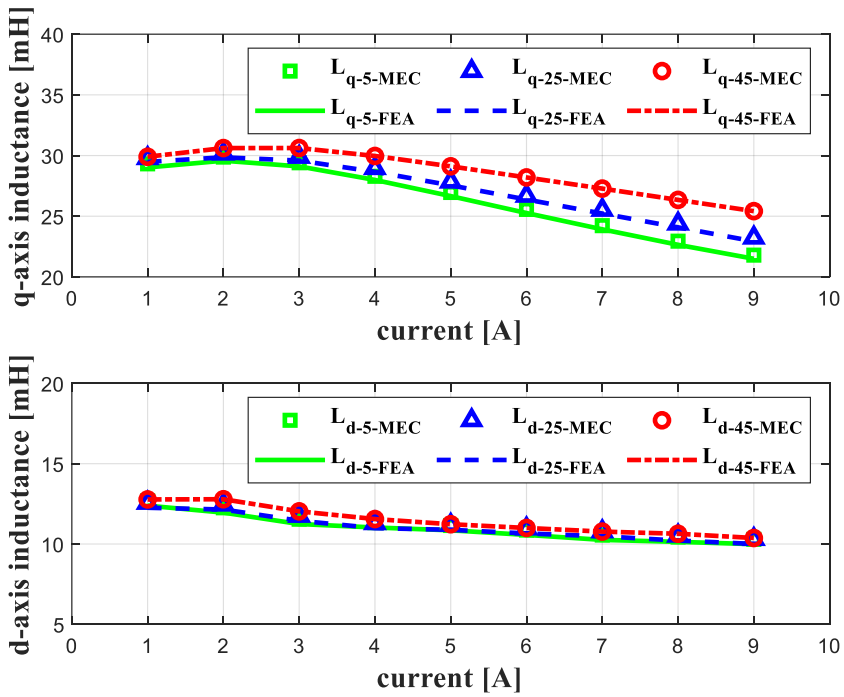

Fig. 3.9 The comparison of results between the FEA and MEC of d-q axis inductances, Current 1 to 9A, Current angle 5, 25 and 45deg at 1500 min^{-1}

Chapter 4 Temperature estimation using Flux Linkage Observer

In this chapter, proposed Flux Linkage Observer is introduced for magnet temperature estimation. The proposed method is that the electrical parameters of the motor can be estimated independently using the modified model reference adaptive system with additional current sampling points. The modified MRAS method with additional current samplings can estimate all four motor parameters simultaneously. The proposed Flux Linkage Observer allows the estimation of the temperature of the rotor's permanent magnet.

4.1 Proposed Flux Linkage Observer

4.1.1 Adaptive control

Adaptive Control covers a set of techniques which provide a systematic approach for automatic adjustment of controllers in real time, in order to achieve or to maintain a desired level of control system performance when the parameters of the plant dynamic model are unknown and/or change in time [29]. Adaptive control systems can be viewed as real-time implementations

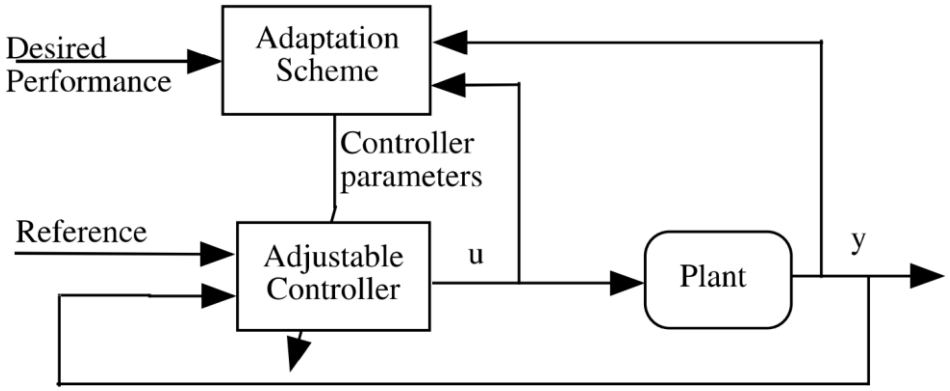

Fig. 4.1 An adaptive control system

of the design and tuning procedures. Controller tuning is performed in real time from data collected in real time from the system. The corresponding adaptive control methods are shown in Fig. 4.1. It features a variety of adaptive techniques that process information in real time to tune controllers to achieve desired performance.

When adaptive control techniques are used in estimating motor parameters, it is difficult to implement because the algorithm itself is complex, but many motor parameters can be estimated simultaneously as well as excellent estimation performance is being studied throughout the estimation techniques. Among them, the Model Reference Adaptive System (MRAS) technique is relatively simple in its algorithm, which is applied not only to the constant estimation of motors but also to address voltage inequalities in inverters or converters.

4.1.2 Model Reference Adaptive System in PMSM

As shown in the previous chapter, the voltage equation in PMSM is converted d-q axis and expressed in the current equation in the form of discrete time, as follows.

$$\begin{bmatrix} v_d \\ v_q \end{bmatrix} = \begin{bmatrix} R_s + L_d p & -L_q \omega_r \\ L_d \omega_r & R_s + L_q p \end{bmatrix} \begin{bmatrix} i_d \\ i_q \end{bmatrix} - \begin{bmatrix} 0 \\ \lambda_m \omega_r \end{bmatrix} \tag{4.1}$$

$$\frac{1}{T_s} \begin{bmatrix} i_d^{n+1} - i_d^n \\ i_q^{n+1} - i_q^n \end{bmatrix} = \begin{bmatrix} L_d & 0 \\ 0 & L_q \end{bmatrix}^{-1} \left(\begin{bmatrix} v_d \\ v_q \end{bmatrix} - \begin{bmatrix} R_s & -L_q \omega_r \\ L_d \omega_r & R_s \end{bmatrix} \begin{bmatrix} i_d \\ i_q \end{bmatrix} - \begin{bmatrix} 0 \\ \lambda_m \omega_r \end{bmatrix} \right) \tag{4.2}$$

where T_s is the sampling time, i_d^n and i_q^n are the current of the d-q axis at the nth sampling time. v_d, v_q , i_d and i_q are the average voltage and current of the d-q axis respectively applied during the sampling period, and ω_r is the angular velocity of the rotor, p is differentiation for time, R_s is the resistance of the coil, L_d and L_q are the inductance of the d-q axis, and λ_m is the magnetic flux linkage by the magnet. The model reference adaptive system, MRAS, method uses the difference between actual and estimated current to estimate motor parameters [30]-[33]. To obtain the next n+1 estimated current using the nth actual current value, the current equation using the estimated parameters is expressed as follows.

$$\frac{1}{T_s} \begin{bmatrix} \hat{i}_d^{n+1} - i_d^n \\ \hat{i}_q^{n+1} - i_q^n \end{bmatrix} = \begin{bmatrix} \hat{L}_d & 0 \\ 0 & \hat{L}_q \end{bmatrix}^{-1} \left(\begin{bmatrix} v_d \\ v_q \end{bmatrix} - \begin{bmatrix} \hat{R}_s & -\hat{L}_q \omega_r \\ \hat{L}_d \omega_r & \hat{R}_s \end{bmatrix} \begin{bmatrix} i_d \\ i_q \end{bmatrix} - \begin{bmatrix} 0 \\ \hat{\lambda}_m \omega_r \end{bmatrix} \right) \tag{4.3}$$

where $\hat{\imath}_d^{n+1}$ and $\hat{\imath}_q^{n+1}$are the estimated current of the n+1 d-q axis. And $\hat{R}_s$, $\hat{L}_d$, $\hat{L}_q$ and $\hat{\lambda}_m$ are estimates of each parameter. The equation of the actual current and the equation of the estimated current are simply expressed using the matrix as shown below.

$$\begin{aligned}\frac{1}{T_s}\left(\mathbf{i_s^{n+1}}-\mathbf{i_s^{n}}\right)&=\mathbf{L}^{-1}\left(\mathbf{v_s}-\mathbf{A}\mathbf{i_s}-\mathbf{k}\right)\\ \frac{1}{T_s}\left(\hat{\mathbf{i}}_\mathbf{s}^{\mathbf{n+1}}-\mathbf{i_s^{n}}\right)&=\hat{\mathbf{L}}^{-1}\left(\mathbf{v_s}-\hat{\mathbf{A}}\mathbf{i_s}-\hat{\mathbf{k}}\right)\end{aligned} \tag{4.4}$$

Using the above equation, the differential equation of the actual current and the estimated current at the sampling point of the T_s is expressed as follows.

$$\frac{\boldsymbol{\Delta}\hat{\mathbf{i}}_\mathbf{s}^{\mathbf{n+1}}}{T_s}=\left(\hat{\mathbf{L}}^{-1}-\mathbf{L}^{-1}\right)\mathbf{v_s}-\left(\hat{\mathbf{L}}^{-1}\hat{\mathbf{A}}-\mathbf{L}^{-1}\mathbf{A}\right)\mathbf{i_s}-\left(\hat{\mathbf{L}}^{-1}\hat{\mathbf{k}}-\mathbf{L}^{-1}\mathbf{k}\right) \tag{4.5}$$

where the error between the n+1[th] actual and estimated current at T_s is defined as $\boldsymbol{\Delta\hat{\mathbf{i}}_\mathbf{s}^{\mathbf{n+1}}}$ = $\hat{\mathbf{i}}_\mathbf{s}^{\mathbf{n+1}}-\mathbf{i_s^{n+1}}$. The above equation is an important basic equation that can estimate motor parameters by MRAS method. However, this equation alone does not satisfy sufficient conditions to estimate all four motor parameters. Eq. (4.5) consists of two linear equations, and since there are four estimated parameters that are unknown, it does not satisfy the uniqueness of solution of the linear equation. To solve this, the proposed method is to add two separate current sampling points within one sampling period, so that there are four differential linear equations of the actual current and estimated current.

4.1.3 Modified MRAS method with additional current sampling

As described above, the proposed method of estimating motor parameters requires two more current samples. Therefore, the timing of the additional current sampling points is determined. As shown in Fig. 4.2, the voltages applied to the motor, usually using a widely applied the pulse width modulation inverter, is divided by the sum of the effective and zero voltages within one sampling period. Normally controlled current is sampled at the midpoint of the zero voltage, and in this paper the additional two current sampling points are set at the two ends of the effective voltage, at which the change of current is relatively large, at T_1. The differential equations for the actual and estimated current at the T_1 point are as follows.

$$\frac{\Delta\hat{\mathbf{i}}_{\mathbf{s1}}^{\mathbf{n+1}}}{T_1} = \left(\hat{\mathbf{L}}^{-1} - \mathbf{L}^{-1}\right)\mathbf{v}_{\mathbf{s1}} - \left(\hat{\mathbf{L}}^{-1}\hat{\mathbf{A}} - \mathbf{L}^{-1}\mathbf{A}\right)\mathbf{i}_{\mathbf{s1}} - \left(\hat{\mathbf{L}}^{-1}\hat{\mathbf{k}} - \mathbf{L}^{-1}\mathbf{k}\right) \tag{4.6}$$

where the error between the actual and estimated current at T_1 is defined as $\Delta\hat{\mathbf{i}}_{\mathbf{s1}}^{\mathbf{n+1}} = \hat{\mathbf{i}}_{\mathbf{s1}}^{\mathbf{n+1}} - \mathbf{i}_{\mathbf{s1}}^{\mathbf{n+1}}$, $\mathbf{v_{s1}}$ and $\mathbf{i_{s1}}$ represent the vector of the averaged voltage and current of the d-q axis applied during T_1. If the averaged current applied during T_s and the averaged current applied during T_1 are assumed to be the same, the two equations obtained above can be used to express the error of the inductances as follows.

$$\frac{\Delta\hat{\mathbf{i}}_{\mathbf{s1}}^{\mathbf{n+1}}}{T_1} - \frac{\Delta\hat{\mathbf{i}}_{\mathbf{s}}^{\mathbf{n+1}}}{T_s} = \left(\hat{\mathbf{L}}^{-1} - \mathbf{L}^{-1}\right)\left(\mathbf{v}_{\mathbf{s1}} - \mathbf{v}_{\mathbf{s}}\right) \tag{4.7}$$

In the above equation, it can be confirmed that the terms of the resistance and the flux linkage of magnet in Eq. (4.6) have been removed. Thus, even if the errors of the resistance and flux linkage of magnet exist, the inductances can be estimated independently. Therefore, the error equations of d-q axis inductance are as follows.

$$\begin{bmatrix}\Delta L_d \\ \Delta L_q\end{bmatrix} \simeq \frac{1}{T_s}\begin{bmatrix}\hat{L}_d{}^2/\Delta v_d & 0 \\ 0 & \hat{L}_q{}^2/\Delta v_q\end{bmatrix}\left(\frac{T_s}{T_1}\begin{bmatrix}\Delta\hat{i}_{d1}^{n+1} \\ \Delta\hat{i}_{q1}^{n+1}\end{bmatrix} - \begin{bmatrix}\Delta\hat{i}_{d}^{n+1} \\ \Delta\hat{i}_{q}^{n+1}\end{bmatrix}\right) \tag{4.8}$$

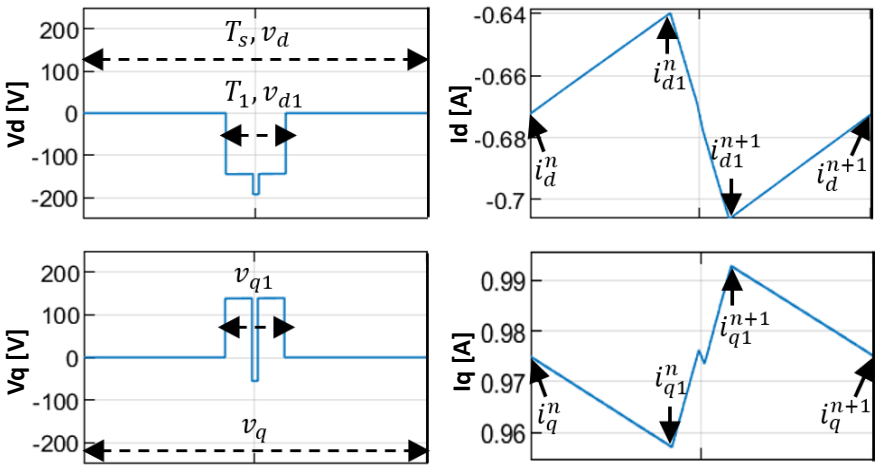

Fig. 4.2 Additional current samplings at T_1

where the inductance errors of the d-q axis are defined as $\Delta L_d = L_d - \hat{L}_d$ and $\Delta L_q = L_q - \hat{L}_q$, respectively. The difference between the voltages of T_1 and T_s are expressed as $\Delta v_d = v_{d1} - v_d$ and $\Delta v_q = v_{q1} - v_q$. The update laws of the estimated inductances are as follows.

$$\begin{bmatrix} \hat{L}_d{}' \\ \hat{L}_q{}' \end{bmatrix} = \begin{bmatrix} k_{i\_L_d}\Delta v_d & 0 \\ 0 & k_{i\_L_q}\Delta v_q \end{bmatrix} \left(\frac{T_s}{T_1} \begin{bmatrix} \Delta\hat{i}_{d1}^{n+1} \\ \Delta\hat{i}_{q1}^{n+1} \end{bmatrix} - \begin{bmatrix} \Delta\hat{i}_{d}^{n+1} \\ \Delta\hat{i}_{q}^{n+1} \end{bmatrix} \right) \tag{4.9}$$

where $k_{i\_L_d}$ and $k_{i\_L_q}$ integral gains of estimated inductances, and the differential mark is ($'$). Next, in the same way as the above inductance estimation process, the resistance and the flux linkage of magnet can be estimated using Eq. (4.6). The error expressions of resistance and flux linkage of magnet are as follows.

$$\begin{bmatrix} \Delta R_s \\ \Delta\lambda_m \end{bmatrix} \simeq \frac{1}{T_s} \begin{bmatrix} \hat{L}_d i_d / i_s{}^2 & \hat{L}_q i_q / i_s{}^2 \\ 0 & \hat{L}_q / \omega_r \end{bmatrix} \begin{bmatrix} \Delta\hat{i}_{d}^{n+1} \\ \Delta\hat{i}_{q}^{n+1} \end{bmatrix} \tag{4.10}$$

where $i_s^2 = i_d^2 + i_q^2$, the estimated errors are defined as $\Delta R_s = R_s - \hat{R}_s$ and $\Delta\lambda_m = \lambda_m - \hat{\lambda}_m$, respectively. The update laws of the estimated resistance and flux linkage of magnet are as follows.

$$\begin{bmatrix} \hat{R}_s{}' \\ \hat{\lambda}_m{}' \end{bmatrix} = \begin{bmatrix} k_{i\_R} i_d & k_{i\_R} i_q \\ 0 & k_{i\_K}\omega_r \end{bmatrix} \begin{bmatrix} \Delta\hat{i}_{d}^{n+1} \\ \Delta\hat{i}_{q}^{n+1} \end{bmatrix} \tag{4.11}$$

where k_{i_R} and k_{i_K} are integral gains of estimated resistance and flux linkage of magnet. Finally, all estimated parameters have an integral gain of:

$$\begin{bmatrix} k_{i\_L_d} \\ k_{i\_L_q} \\ k_{i\_R} \\ k_{i\_K} \end{bmatrix} = \frac{1}{T_s} \begin{bmatrix} \frac{\hat{L}_d{}^2\omega_{LC}}{\Delta v_d{}^2} & \frac{\hat{L}_q{}^2\omega_{LC}}{\Delta v_q{}^2} & \frac{\hat{L}_s\omega_{RC}}{i_s{}^2} & \frac{\hat{L}_q\omega_{KC}}{\omega_r{}^2} \end{bmatrix}^{\mathrm{T}} \tag{4.12}$$

where $\hat{L}_s = (\hat{L}_d + \hat{L}_q)/2$, the bandwidths of estimated motor parameters are ω_{LC}, ω_{RC} and ω_{KC}. The modified MRAS method using additional current sampling proposed in this paper can estimate all four parameters of the motor simultaneously.

Fig. 4.3 shows the simulation result of modified estimation laws (4.9) and (4.10). Motor parameter errors have not affected each other. The parameter estimation performance is stable, and the steady state error converges to zero. The modified MRAS method with additional current samplings can estimate all four motor parameters simultaneously.

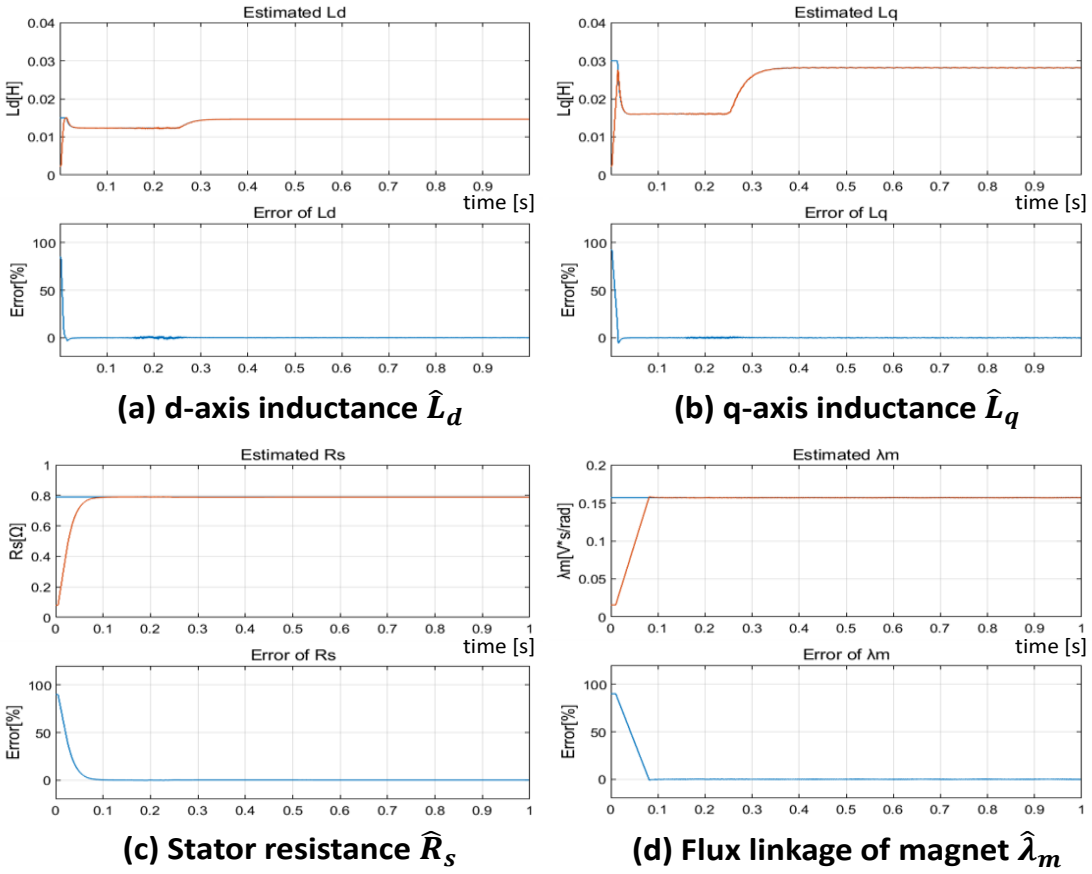

Fig. 4.3 The simulation result of the modified MRAS for motor parameter estimation

4.1.4 Stability of Flux Linkage Observer

In this paper, the estimation of inductance can easily be confirmed to be a stable estimation because it is a method of obtaining solutions to the equation using additional sampling. Therefore, the error of inductance is determined to be eliminated. To determine the stability of the system, the Lyapunov function is considered as follows [33].

$$V = \frac{1}{2}\left(\mathbf{\Delta i}^{\mathrm{T}}\mathbf{L}\mathbf{\Delta i} + \mathbf{\Delta \eta}^{\mathrm{T}}\mathbf{Q}\mathbf{\Delta \eta}\right) \tag{4.13}$$

Where $\mathbf{\Delta i}$, $\mathbf{\Delta \eta}$, $\mathbf{L}$ and $\mathbf{Q}$ are as follow,

$$\mathbf{\Delta i} = \begin{bmatrix} \hat{i}_d - i_d \\ \hat{i}_q - i_q \end{bmatrix} = \begin{bmatrix} \Delta i_d \\ \Delta i_q \end{bmatrix}, \quad \mathbf{\Delta \eta} = \begin{bmatrix} \Delta R_s - \hat{R}_s \\ \Delta \lambda_m - \hat{\lambda}_m \end{bmatrix} = \begin{bmatrix} \Delta R_s \\ \Delta \lambda_m \end{bmatrix}, \quad \mathbf{L} = \begin{bmatrix} L_d & 0 \\ 0 & L_q \end{bmatrix}, \quad \mathbf{Q} = \begin{bmatrix} q_1 & 0 \\ 0 & q_2 \end{bmatrix}$$

$\mathbf{Q}$ is positive diagonal matrix where the i[th] diagonal element q_i is a positive value used as weight value for $\mathbf{\Delta \eta}$.

Using $\mathbf{L} = \mathbf{L}^{\mathbf{T}}$, the differential ($'$) of V is obtained as follows.

$$\begin{aligned} V' &= \frac{1}{2}\left\{\mathbf{\Delta i}^{\mathrm{T}}\mathbf{L}\mathbf{\Delta i}' + \left(\mathbf{L}\mathbf{\Delta i}'\right)^{\mathrm{T}}\mathbf{\Delta i} + \mathbf{\Delta \eta}^{\mathrm{T}}\mathbf{Q}\mathbf{\Delta \eta}' + \left(\mathbf{Q}\mathbf{\Delta \eta}'\right)^{\mathrm{T}}\mathbf{\Delta \eta}\right\} \\ &= \mathbf{\Delta i}^{\mathrm{T}}\mathbf{L}\mathbf{\Delta i}' + \mathbf{\Delta \eta}^{\mathrm{T}}\mathbf{Q}\mathbf{\Delta \eta}' \\ &= -R_s\left(\Delta i_d{}^2 + \Delta i_q{}^2\right) + \Delta R_s\left(i_d\Delta i_d + i_q\Delta i_q\right) + \Delta\lambda_m\omega_r\Delta i_q - q_1\Delta R_s\hat{R}_s' - q_2\Delta\lambda_m\hat{\lambda}_m' \end{aligned} \tag{4.14}$$

The update laws of resistance and flux linkage of magnet are set as follows.

$$\begin{aligned} \hat{R}_s' &= \frac{1}{q_1}\left(i_d\Delta i_d + i_q\Delta i_q\right) \\ \hat{\lambda}_m' &= \frac{1}{q_2}\left(\omega_r\Delta i_q\right) \end{aligned} \tag{4.15}$$

Then, comparing Eq. (4.11) and Eq. (4.15), q_1 and q_2 are represented by the integral gain below.

$$\frac{1}{q_1} = k_{i\_R}, \quad \frac{1}{q_2} = k_{i\_K}$$

Finally, Eq. (4.14) is expressed as follows.

$$V' = -R_s \left(\Delta i_d^{\,2} + \Delta i_q^{\,2} \right) \tag{4.16}$$

Here, if Δi_d and Δi_q do not converge to 0, V diverges to $-\infty$. Since V is always a positive value, it can be seen that Δi_d and Δi_q must always converge to 0. The stability of this estimation has been demonstrated.

For the stability of the estimation performance, the bandwidth of the inductance estimation ω_{LC}, which requires relatively fast response because it is immediately changed by stator current, is selected as 1/10 of the bandwidth of the current controller ω_{CC}. On the other hand, resistance and magnetic flux linkage of magnet are characterized by relatively slow response performance, mainly due to temperature variations. Therefore, the bandwidths of resistance and flux linkage ω_{RC}, ω_{KC} are selected as 1/100 of the bandwidth of the current controller.

$$Current\ Controller\ Bandwidth: \ \omega_{CC} = 2\pi * 1000 \left[\frac{rad}{s}\right]$$

$$=> \ \omega_{LC} = \frac{\omega_{CC}}{10}, \qquad \omega_{RC} = \omega_{KC} = \frac{\omega_{CC}}{100}$$

4.1.5 Practical Considerations

(1) Small stator resistance

To reduce the error of the proposed Flux Linkage Observer, several factors must be considered. When estimating temperature at high speeds, temperature is basically estimated based on magnetic flux. Therefore, it is important to know the exact winding resistance component when calculating magnetic flux linkage. If the stator resistance value is very small, the estimated resistance may have a relatively large error due to low voltage drop component. In this paper, the calculated resistance value R_{sm} uses the values measured at the temperature of the winding as follows.

$$R_{sm} = R_{s0} \cdot \left\{1 + \alpha_{cu}\left(\theta_w - \theta_0\right)\right\} \tag{4.17}$$

where R_{sm} is calculated resistance value at winding temperature θ_w, and $\alpha_{cu} = 0.0040$ [K^{-1}] is the temperature coefficient of copper, and R_{s0} is the initial resistance value at initial temperature θ_0, and θ_w is the stator winding temperature.

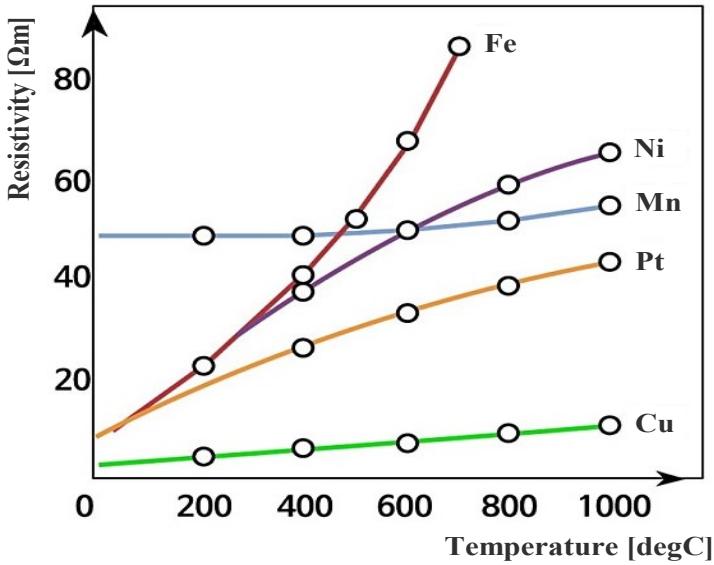

Fig. 4.4 Magnet temperature estimation using flux linkage observer

(2) Dead time compensation

To prevent arm-short of an inverter power switch, a dead time (0.1~3us) is usually applied at the on/off time of inverter switching. However, on the actual switch, parasitic components appear to cause delays within the on/off operation and short-circuit the serial switch to the DC link. A short circuit allows excessive current through the serial switch, causing a serious system failure. Therefore, the reliability of the system can be ensured by injecting sufficient dead-time T_d until the switch reaches a stable state [34] -[36]. The voltage error affected by dead time can be calculated as follows.

$$V_d = \frac{T_{on} + T_d - T_{off}}{T_s} V_{dc} \tag{4.18}$$

$$\Delta v_{an} = \left\{ \begin{array}{l} -V_d \ \ (i_a > 0) \\ +V_d \ \ (i_a < 0) \end{array} \right\} \tag{4.19}$$

Where V_{dc} is DC link voltage, V_{an} is the pole voltage in phase a, V_d is pole voltage error, T_s is switching period time and T_{on} and T_{off} are switch turn on/off delay. As shown in Fig. 4.5, this dead time results in an error in command voltage and actual voltage, which also results in an error in estimating motor parameters. Therefore, for accurate estimation, dead-time compensation should be applied [36].

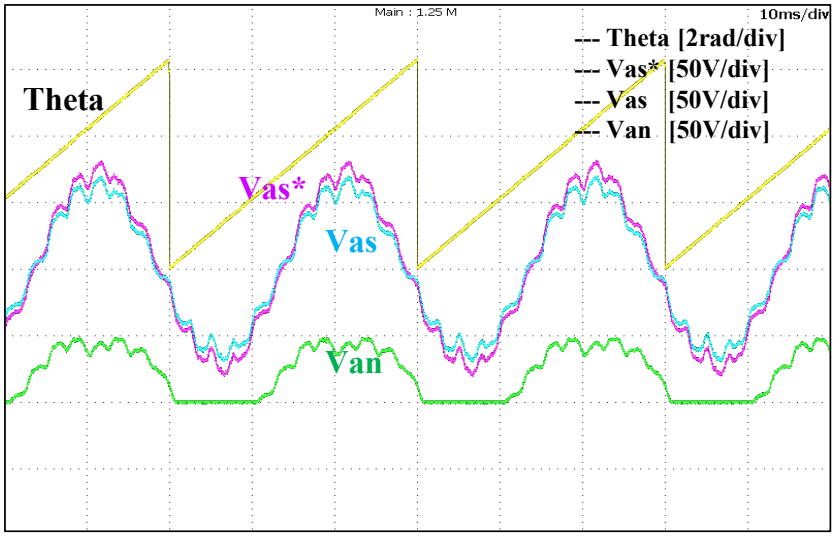

Fig. 4.5 Magnet temperature estimation using flux linkage observer

4.2 Temperature estimation using Flux Linkage Observer

4.2.1 Temperature coefficient of magnet

As shown in Table 4.1, the permanent magnet shows that the residual magnetic flux density varies according to its characteristic temperature [37]. Especially for the widely used a neodymium magnet, NdFeB, the residual magnetic flux density decreases as the temperature increases.

$$\begin{aligned} B_r &= B_{r0}\left(1+\alpha_{PM}\left(\theta_m-\theta_0\right)\right) \\ H_{ci} &= H_{ci0}\left(1+\beta_{PM}\left(\theta_m-\theta_0\right)\right) \end{aligned} \tag{4.20}$$

where α_{PM} is the temperature coefficient of residual magnetic flux density, β_{PM} is the temperature coefficient of coercive force, H_{ci} is the intrinsic coercive force, θ_m is the magnet temperature and θ_0 is the initial temperature. This change due to temperature increase also reduces the flux linkage of permanent magnets during operation. Using this, the magnet temperature can be estimated by the Flux Linkage Observer.

Table 4.1 Temperature Coefficient of Magnet

Magnet type	**Grade**	$\boldsymbol{\alpha_{PM}}$**[%]**	$\boldsymbol{\beta_{PM}}$**[%]**
Alnico,cast	5	-0.02	-0.01
Sm_2Co_{17}	27MGOe	-0.035	-0.20
NdFeB, bonded	MQP-A, -O	-0.13	-0.40
NdFeB, bonded	MQP-B	-0.11	-0.40
NdFeB, sintered	L-38UHT	-0.10	-0.50
NdFeB, sintered	N38UJ	-0.12	-0.55
NdFeB, sintered	N48M	-0.12	-0.65
Ferrite, sintered	C-5, -8	-0.20	0.27

4.2.2 Convert flux linkage of magnet to temperature

PM materials can exhibit a significant decrease in the remanent flux density with respect to increasing temperature. Therefore, the magnet temperature can be estimated as follow,

$$\hat{\lambda}_m = \lambda_{m0} \cdot \left(1 + \alpha_m \left(\hat{\theta}_{m-FO} - \theta_0\right)\right) \tag{4.21}$$

$$\hat{\theta}_{m-FO} = \frac{1}{\alpha_m}\left(\frac{\hat{\lambda}_m}{\lambda_{m0}} - 1\right) + \theta_0 \tag{4.22}$$

where λ_{m0} is the initial flux linkage of magnet at 25degC, α_m is the temperature coefficient of flux linkage of magnet.

The block diagram of the proposed Flux Linkage Observer is shown in Fig. 4.6. The voltage is compensated using dead-time compensation and resistance is calculated by measured winding temperature. To analysis the proposed Flux Linkage Observer, the following sequences are required.

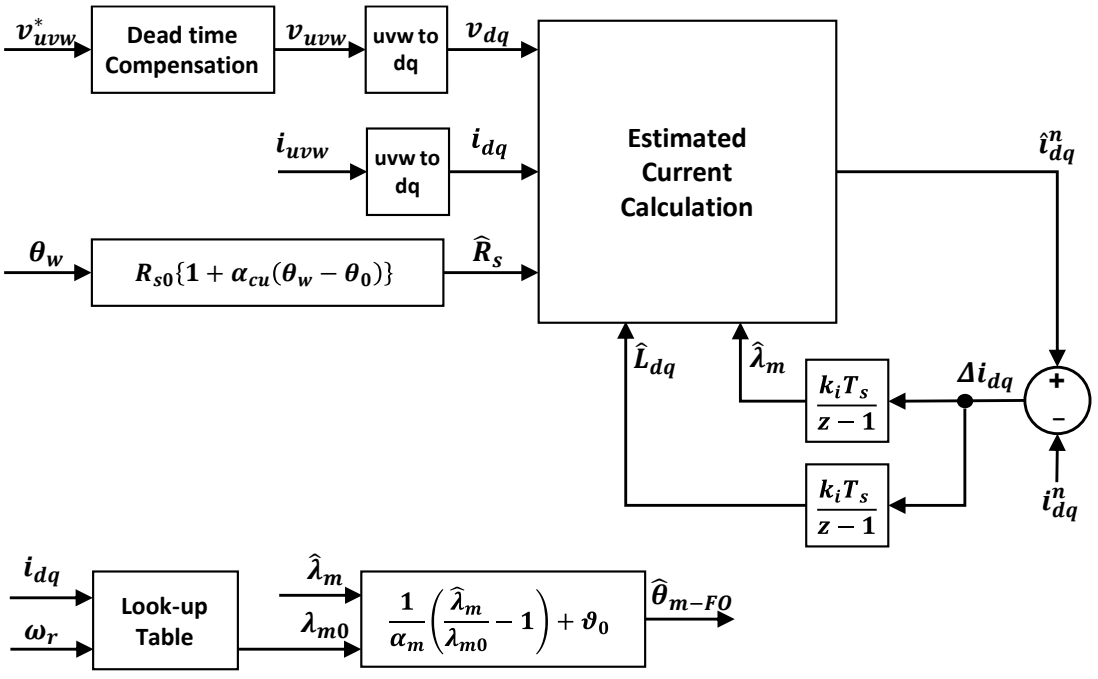

Fig. 4.6 Magnet temperature estimation using flux linkage observer

(1) The voltage is compensated using dead-time compensation.

(2) The currents are sampled additionally at T_s and T_1.

(3) The resistance $\hat{R}_s$ is calculated by measured winding temperature.

(4) The inductances $\hat{L}_{dq}$ are estimated by estimated current from Eq. (4.9).

(5) The flux linkage of magnet $\hat{\lambda}_m$ are estimated by estimated current from Eq. (4.11).

(6) The initial flux linkage of magnet λ_{m0} is a value that varies with current and speed, so it is stored and used in the look-up table (LUT).

(7) Finally, using Eq. (4.22), the magnet temperature $\hat{\theta}_{m-FO}$ is estimated by estimated flux linkage of magnet.

4.3 Experimental results of Flux Linkage Observer

In this section, the effectiveness of the proposed method is verified by experimental result. An interior permanent magnet synchronous motor (IPMSM) with 24 slots/4 poles and distributed windings is used for evaluation, and the specification and test condition are shown in Table 4.2 and Table 4.3. The temperature was measured by a k-type thermocouple and the non-contact measurement data transmission device using RF communication was used to measure the temperature of rotating rotor as shown in Fig. 4.7. The motor speed conditions are 1500 / 2000 / 2500 min^{-1} and the control current is from 1 to 9A and current angle is from 0 to 45deg.

Fig. 4.8, Fig. 4.9, and Fig. 4.10 show the experimental result of motor parameter and magnet temperature estimation at 1500, 2000 and 2500 min^{-1} respectively. (a) shows the experimental results of the estimated inductance. Inductance is observed to vary in value with the magnitude and angle of the current. It is confirmed that the larger the magnitude of the q-axis current, the stronger the magnetic saturation phenomenon, reducing the q-axis inductance. Comparing inductance estimates when the temperature is 25degC and 75degC, the inductance values rise slightly at 75degC. (b) shows the results of experiments in estimated magnetic flux linkage of magnet. It is also observed that the flux linkage of magnet changes in value with the magnitude and angle of the current. These results confirm that the reduction in flux linkage of magnet due to temperature is large and proportional, as shown in Eq. (4.20). (c) shows the result of converting estimated flux linkage of magnet using Eq. (4.22) into the temperature of the permanent magnet.

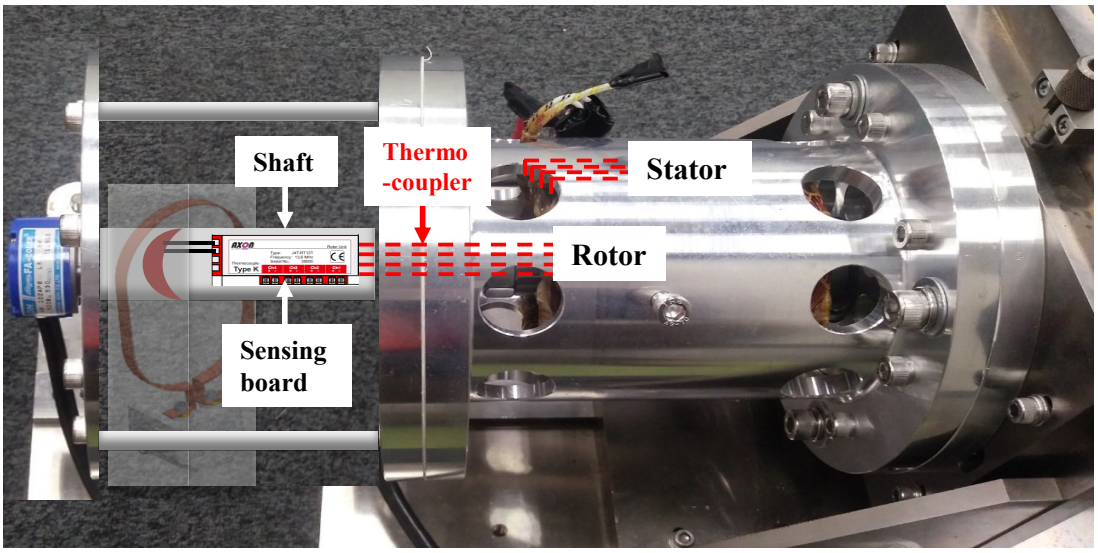

Fig. 4.7 Experimental Set of Proposed method

Through these results, the temperature coefficient of flux linkage α_m is determined to be -0.09125 · 10^{-2}. It is confirmed that the temperature estimation error of the permanent magnet is within ±7degC.

Table 4.2 Motor Specification of Flux linkage observer

Parameters	**Value**
Winding form	Distributed
Phase connection	Wye
Slots / Poles	24 / 4
Number of turns	140
Phase resistance	0.9 Ω
Magnetic flux linkage (no load)	0.08970 Wb

Table 4.3 Experimental Test Condition of Flux linkage observer

Condition	**Value**
Speed	1500 / 2000 / 2500min^{-1}
Control current	1 ~ 9Amax
Current angle	0 ~ 45degree
Minimum current measurement with AD7357, 14-bit	6.103mA
Response time to 90% of current measurement, t_r	< 1μs
Initial temperature	25degC

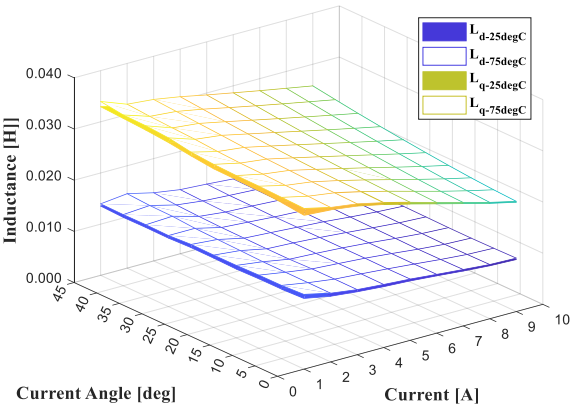

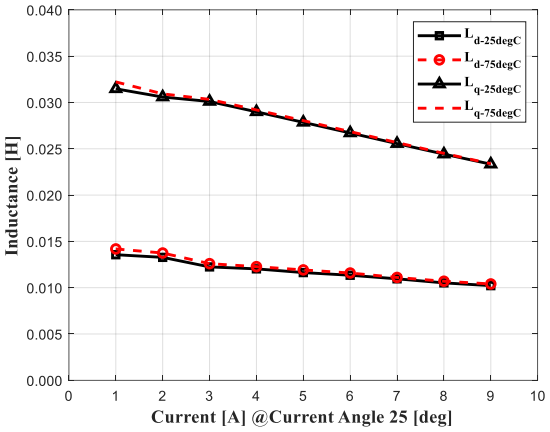

(a) Estimated inductance at Current angle 25deg

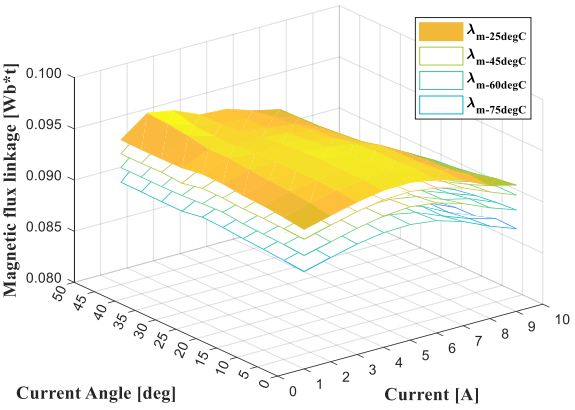

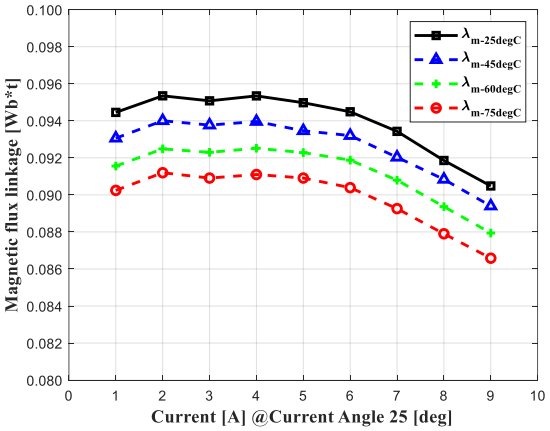

(b) Estimated flux linkage of magnet at Current angle 25deg

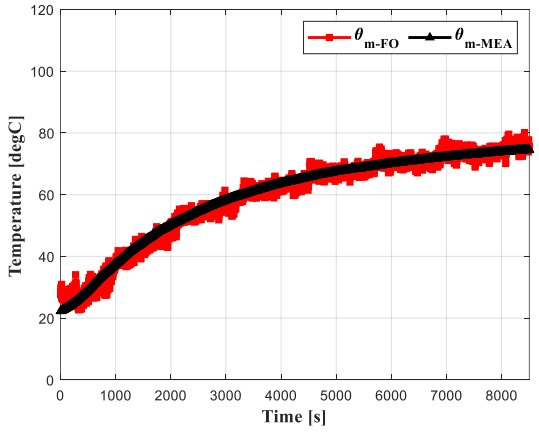

(c) Estimated magnet temperature at Current 7A, Current angle 25deg

Fig. 4.8 The experimental result of motor parameter and magnet temperature estimation at 1500min^{-1}

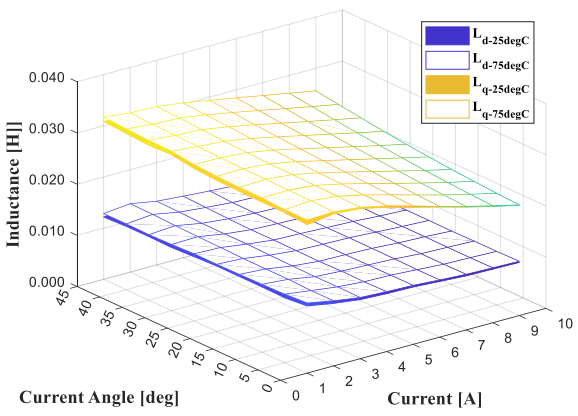

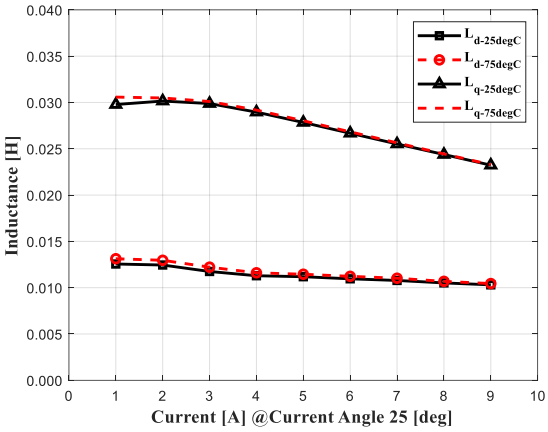

(a) Estimated inductance at Current angle 25deg

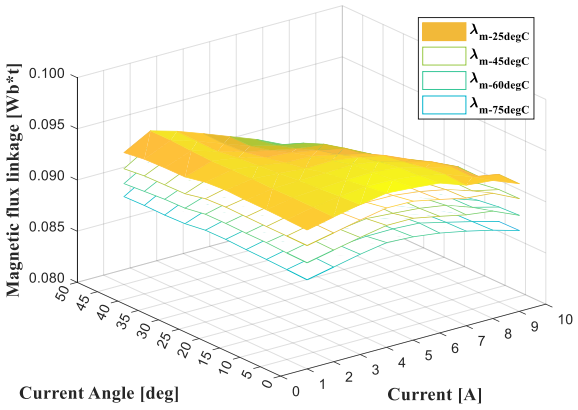

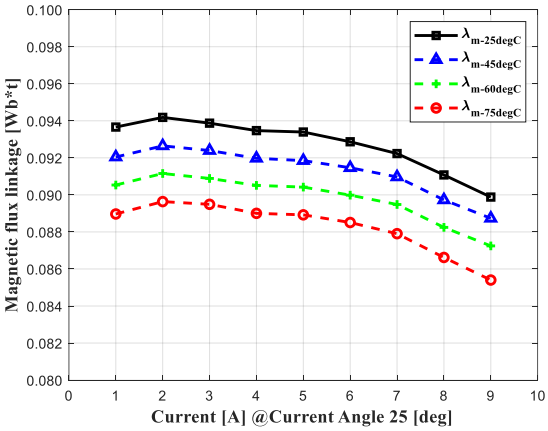

(b) Estimated flux linkage of magnet at Current angle 25deg

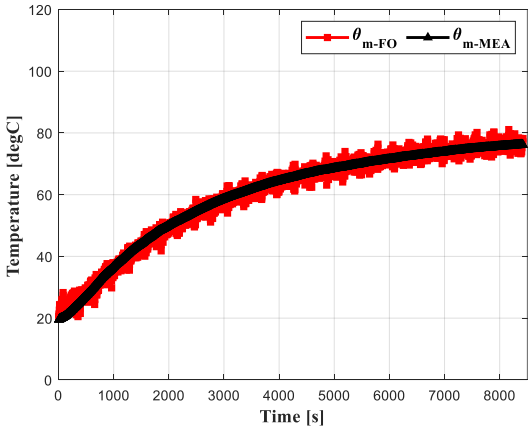

(c) Estimated magnet temperature at Current 7A, Current angle 25deg

Fig. 4.9 The experimental result of motor parameter and magnet temperature estimation at 2000min^{-1}

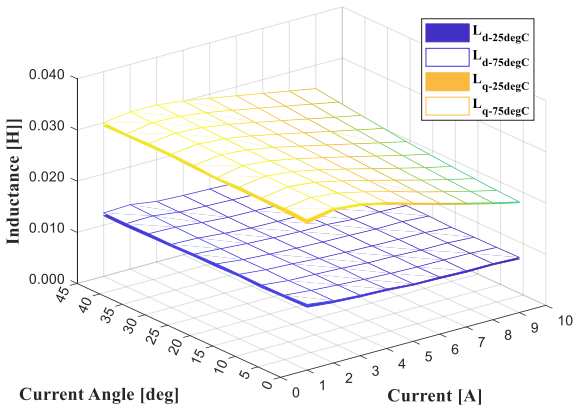

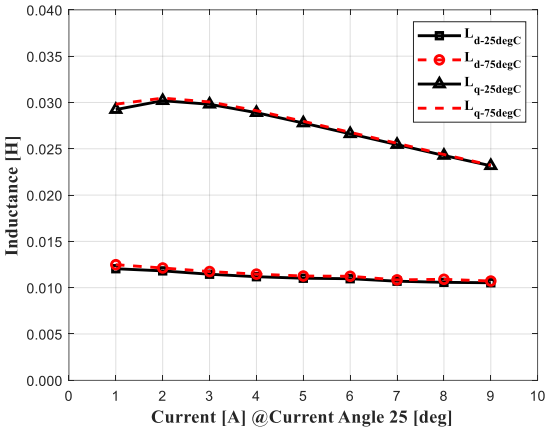

(a) Estimated inductance at Current angle 25deg

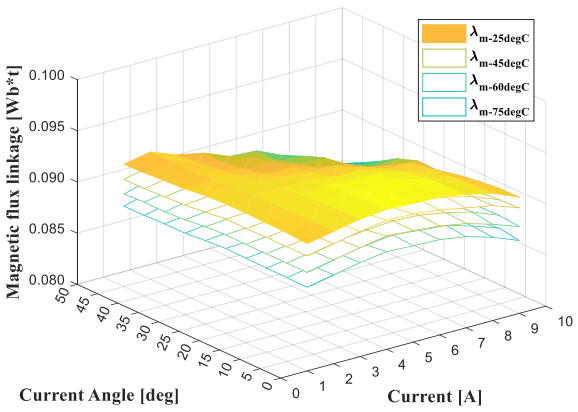

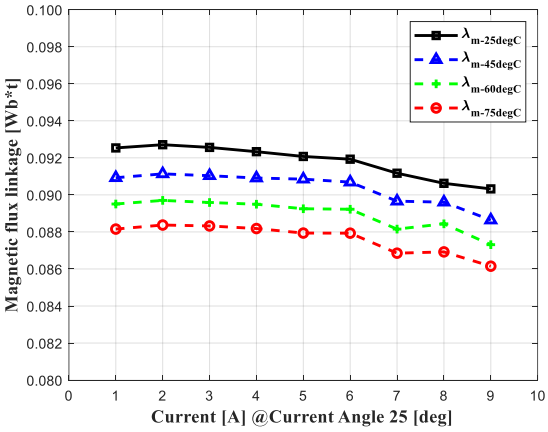

(b) Estimated flux linkage of magnet at Current angle 25deg

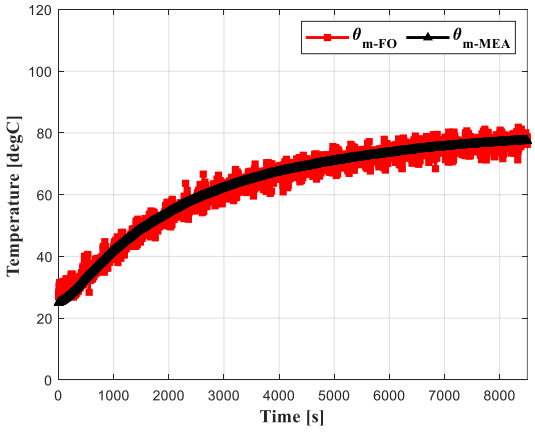

(c) Estimated magnet temperature at Current 7A, Current angle 25deg

Fig. 4.10 The experimental result of motor parameter and magnet temperature estimation at 2500min^{-1}

Chapter 5 Magnet temperature estimation using Thermal Equivalent Circuit

5.1 Thermal Equivalent Circuit

The thermal analysis techniques of motors include Thermal Equivalent Circuit (TEC) using the Lumped Parameter Method, and Finite Element Analysis (FEA), Finite Difference Method (FDM) using the Distributed Parameter Method [9]-[13]. Thermal analysis using FEA of FDM usually requires a huge matrix because they are divided into fine elements to analysis complex structure. This huge matrix has the disadvantage of longer computation time for temperature analysis. On the other hand, thermal analysis by thermal equivalent circuit method using lumped parameter method is simple to calculate because the matrix size is small. Therefore, the advantage is that the overall temperature analysis in various parts of the motor can be easily estimated in real time.

In this paper, the complex heat transfer of the motor is equivalent to a simple thermal resistance and heat source to perform thermal analysis using a thermal equivalent circuit method. This thermal equivalent circuit is constructed according to the shape of the target motor to calculate conduction and convection thermal resistance, and the temperature change over time is estimated.

5.1.1 Heat transfer theory

Heat transfer is thermal energy in transit due to a spatial temperature difference. As shown in Table 5.1, heat transfer takes place in three ways: conduction, convection, and radiation [38]. Conduction is caused by energy of irregular molecular motion, and when there is a temperature gradient in a stationary medium, such as solid and liquid, it occurs through the medium. Convection is caused by the diffusion of energy by flow convection and occurs between moving fluids and surfaces with different temperatures. Finally, thermal radiation means that all surfaces of finite temperatures emit energy in the form of electromagnetic waves. Therefore, heat transfer occurs between two surfaces with different temperatures even without an intermediate medium.

Where,

q'' $[W/m^2]$: Heat flux, Heat transfer rate per unit area

q $[W]$: Heat transfer rate

T $[K]$: Absolute temperature

T_s : Temperature of surface

T_∞ : Temperature of fluid

ϵ_t : Emissivity

σ_t $[W/m^2 \cdot K]$: Stefan-Boltzmann's constant

In this paper, heat transfer by convection and conduction is considered. In the case of radiant heat transfer, the absolute temperature is low, so it is not considered in the target motor.

Table 5.1 Theory of heat transfer

method	mechanism	heat flux equation	material property
Conduction	Energy diffusion by irregular molecular motion 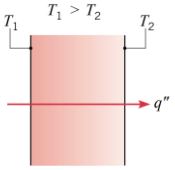	Fourier's law $q''_x = -k\frac{dT}{dx}$	thermal conductivity k $[W/m \cdot K]$
Convection	Energy diffusion by irregular molecular motion + bulk fluid motion 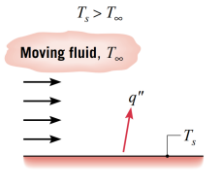	Newton's law of cooling $q''_x = h(T_s - T_\infty)$	convection heat transfer coefficient h $[W/m^2 \cdot K]$
Radiation	Energy Transfer by Electromagnetic Wave 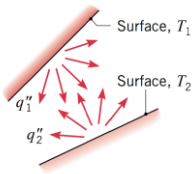	Stefan-Boltzmann's law $q'' = \epsilon_t \sigma_t (T_s - T_s^4)$	radiation heat transfer coefficient h_r $[W/m^2 \cdot K]$

5.1.2 Calculation of thermal resistance and heat capacity

In this paper, the structure of the motor for applying the thermal equivalent circuit is shown in Fig. 5.1. In the PMSM, as main heat sources, electric losses such as copper loss and iron loss are the heat generation sources. Temperature rising occurs due to conduct heat energy from the sources. Firstly, the proposed method calculates electric losses of each parts using FEA, copper loss, iron loss and eddy current loss. Electric losses of each part are calculated each driving conditions such as the rotational speed and the current. Secondly, the magnet temperature is calculated using thermal equivalent circuit by heat generations and initial temperature. From heat transfer theory, each component of thermal equivalent circuit is calculated as following equations.

$$C_{th} = \rho V c \tag{5.1}$$

$$R_{cond} = \frac{l}{kA} \tag{5.2}$$

$$R_{conv} = \frac{1}{hA} \tag{5.3}$$

Where, C_{th} is thermal capacitance, ρ is density, V is volume, c is specific heat. R_{cond} is thermal resistance of conduction, k is thermal conductivity, l is length and A is area. R_{conv} is

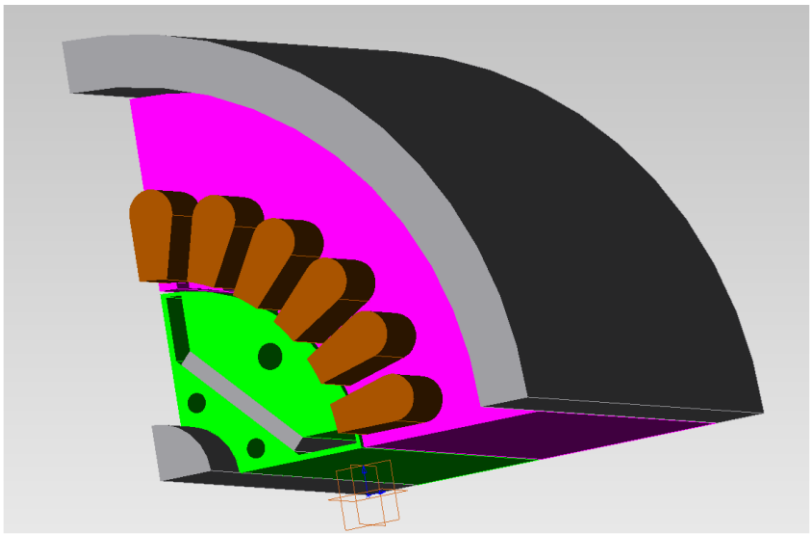

Fig. 5.1 Structure of the target motor

thermal resistance of convection, h is heat transfer coefficient. As shown in Fig. 5.2 , a simple thermal equivalent circuit constructed using the above equations.

Convection is a heat transfer that occurs between a solid plane and a fluid or gas flowing in it, with a combination of conduction and fluid flow. The flow between the solid surface and the fluid enhances the heat transfer, but the heat transfer coefficient varies depending on the flow rate of the fluid, making it difficult to calculate the heat transfer rate. The points at which convection occurs in the motor are the outside of the frame, the air gap, the air inside the end cap, etc. In the above three points, natural convection occurs outside the frame and inside the endcap, and in the air gap, the rotor rotates and forced convection occurs. First, the natural convection heat transfer coefficient outside the frame and inside the endcap are calculated as follows [39],

$$h = 15.5\left(0.29V_{air} + 1\right) \tag{5.4}$$

Where V_{air} is the velocity of airflow.

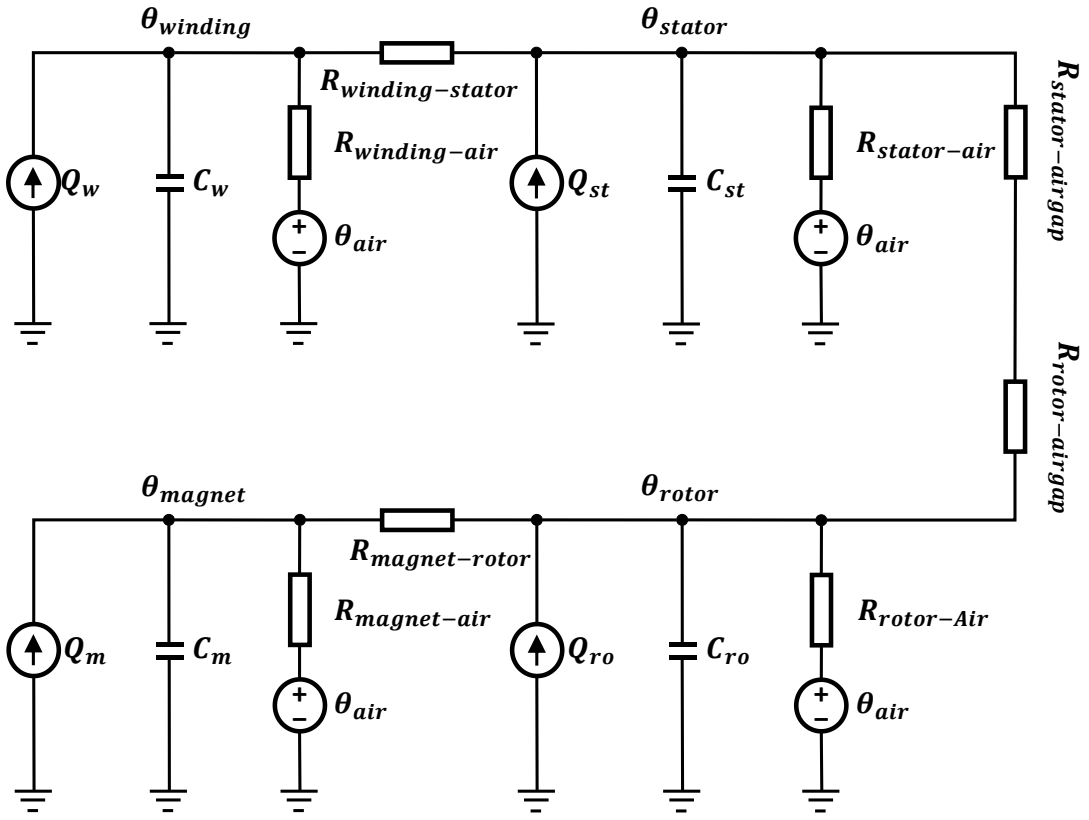

Fig. 5.2 Thermal equivalent circuit for magnet temperature estimation

On the other hand, in the airgap, convection heat transfer is caused by the relative rotational motion of the stator and the rotor. The convective heat transfer coefficient in the air gap h_{airgap} is expressed as Nusselt Number N_{Nu}, the length of the airgap l_g, and the thermal conductivity of the air k_{air}, as shown as follows.

$$h_{airgap} = \frac{N_{Nu} k_{air}}{l_g} \tag{5.5}$$

$$N_{Nu} = \begin{cases} 2.2 & \left(N_{Ta} \le 41.1\right) \\ 0.23 N_{Ta}^{0.63} N_{\Pr}^{0.23} & \left(N_{Ta} \ge 41.1\right) \end{cases} \tag{5.6}$$

$$N_{Ta} = \frac{l_g V_{rotor}}{v_a}, \quad N_{\Pr} = \frac{c_p v_a}{k_{air}} \tag{5.7}$$

Where, N_{Ta} is Taylor Number and N_{Pr} is Prandtl Number. V_{rotor} is the velocity of rotor, v_a is the dynamic viscosity of air and c_p is the specific heat of air. Thus, the convection heat transfer coefficient in the air gap can be calculated based on the above equations.

5.2 Temperature estimation using Thermal Equivalent Circuit

5.2.1 Calculation of thermal matrix

The thermal equivalent circuit can be mathematically converted into a differential matrix equation through the Nodal analysis can be used to define a relationship between the node temperature vector $\vec{\boldsymbol{\theta}}$, heat generation vector $\vec{\mathbf{Q}}_{\mathbf{th}}$, the node conductance matrix $[\mathbf{G}_{\mathbf{th}}]$ and the thermal capacitance matrix $[\mathbf{C}_{\mathbf{th}}]$. The estimated temperature of each node can be obtained through the Euler method or the Runge–Kutta method. As shown below, thermal capacitances and thermal resistances can be calculated of both the geometric structure of a motor and material specification.

$$\frac{d\vec{\boldsymbol{\theta}}}{dt} = \mathbf{C}_{th}^{-1} \times \left(\vec{\mathbf{Q}}_{th} - \mathbf{G}_{th} \times \vec{\boldsymbol{\theta}} \right) \tag{5.8}$$

Where $\vec{\boldsymbol{\theta}}$ is temperature vector, $\mathbf{C}_{\mathbf{th}}$ is thermal capacitance matrix, $\vec{\mathbf{Q}}_{\mathbf{th}}$ is motor loss vector and $\mathbf{G}_{\mathbf{th}}$ is thermal permeance matrix.

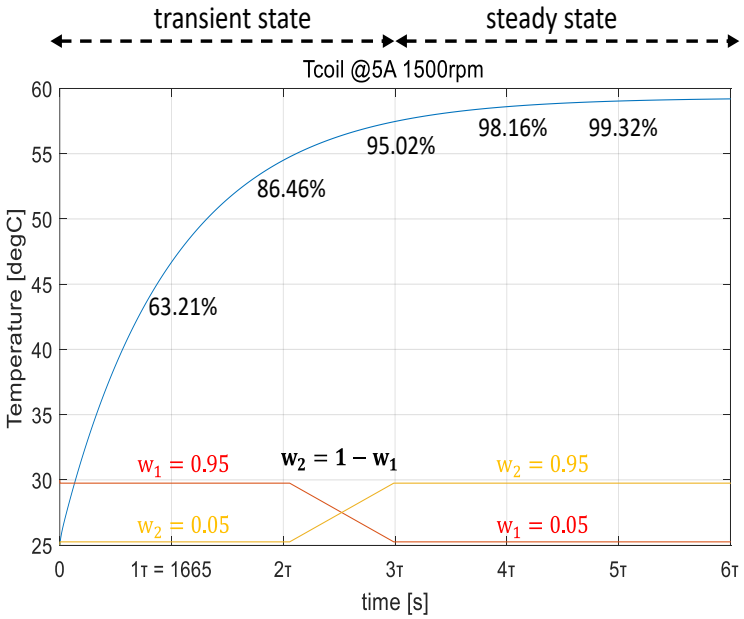

Fig. 5.3 Weight coefficients for the estimated thermal capacitance and heat transfer coefficient

5.2.2 Optimization of heat capacitance and heat transfer coefficient

Despite its many advantages, thermal models are highly dependent on the geometry of the motor and cooling system and operating speed. Therefore, specific design and calibration are often required to increase the accuracy of temperature estimates [40]. The block diagram of the optimization of heat capacitance and heat transfer coefficient is shown in Fig. 5.4. The proposed method is that measured temperature of the stator winding is used to compensate for the thermal capacitances C_{th}, in a transient state and the heat transfer coefficient h, in a steady state for the thermal equivalent circuit. In a transient state, thermal capacitances are important because of the large amount of temperature change. On the other hand, the thermal resistances are important in the steady state because the temperature change is very small. Therefore, it is effective to compensate thermal capacitance C_{th}, for transient responses and convective heat transfer coefficient h, for steady-state responses. The updated laws are as follows.

$$\begin{bmatrix} \hat{k}_{capa}^{n+1} \\ \hat{k}_{conv}^{n+1} \end{bmatrix} = \begin{bmatrix} \hat{k}_{capa}^{n} \\ \hat{k}_{conv}^{n} \end{bmatrix} + \begin{bmatrix} g_1 w_1 & 0 \\ 0 & g_2 w_2 \end{bmatrix} \begin{bmatrix} \Delta\dot{\theta}_W \\ \Delta\theta_W \end{bmatrix} \tag{5.9}$$

Where the error between the measured and estimated coil temperature is expressed as $\Delta\theta_w = \theta_w - \hat{\theta}_w$ and the differential error is expressed as $\Delta\dot{\theta}_w = \dot{\theta}_w - \hat{\dot{\theta}}_w$. $\hat{k}_{capa}$ is the estimated thermal capacitance ratio, $\hat{k}_{conv}$ is the estimated heat transfer coefficient ratio, g_1, g_2 are integral gains

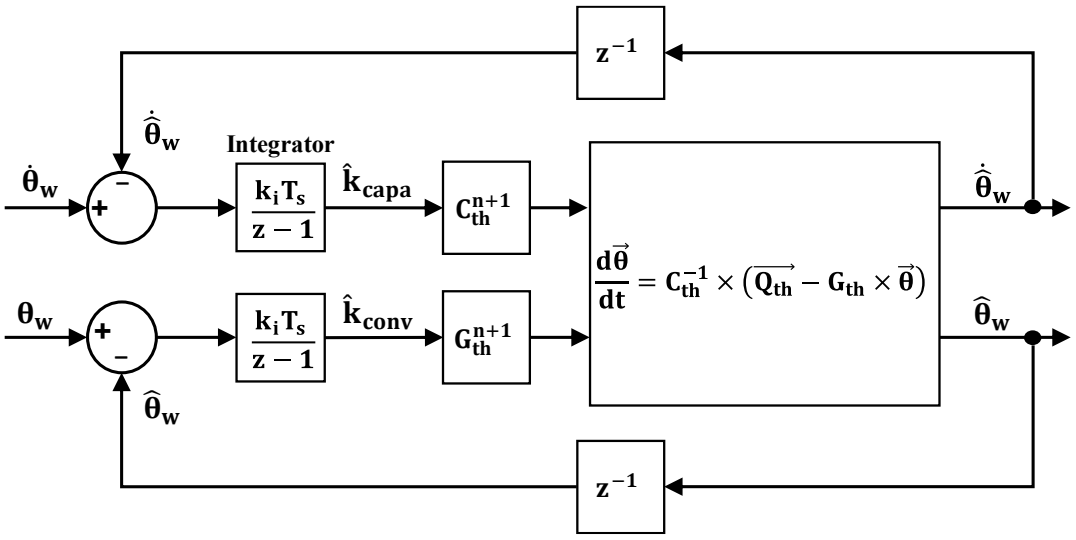

Fig. 5.4 Optimization of heat capacitance and heat transfer coefficient

of the observer and w_1, w_2 are weight coefficients for the estimated thermal capacitance and heat transfer coefficient respectively. For smooth conversion of these weight coefficients, the time constant ratio is obtained using the following equations according to the winding temperature.

$$\theta(t)-\theta(0)=\left(\theta(\infty)-\theta(0)\right)\left(1-e^{-\frac{t}{\tau}}\right) \tag{5.10}$$

$$\frac{d\theta(t)}{dt}=\left(\theta(\infty)-\theta(0)\right)\left(\frac{t}{\tau}e^{-\frac{t}{\tau}}\right) \tag{5.11}$$

$$x=\frac{t}{\tau}=\log\left(\frac{1}{\tau}\left(\frac{\theta(t)-\theta(0)}{d\theta(t)/dt}+1\right)\right) \tag{5.12}$$

Where τ is the time constant of the thermal equivalent circuit and x is the time constant ratio which is divided by time constant τ. As shown in Fig. 5.3, the weight coefficients are changed when the section of the time constant ratio from 2τ to 3τ. In this way, thermal capacitance is compensated for the transient response, and heat transfer coefficient is compensated for the steady-state response. Therefore, the weight coefficients (w_1, w_2) are applied separately in the transient and steady-state responses. Finally, the thermal capacitance ratio and heat transfer coefficient ratio are estimated through an observer with the weight values.

Fig. 5.5 shows a comparison between the estimated temperature and the measured temperature with parameter optimization. The proposed method using thermal component ratio observer has been found to reduce the temperature error. As shown in Fig. 5.5 (b) and (d), the maximum temperature error is $|\theta_{err}| < 5.0$ degC or less. It is confirmed that both transient and steady-state errors are reduced. The result of thermal component ratios and weight coefficients are shown in Fig. 5.5 (e) and (f). These results mean that the measured temperature of the stator winding is used to compensate for the thermal capacitances C_{th}, in a transient-state and the convective heat transfer coefficient h_{conv}, in steady-state for the thermal equivalent circuit. Also, it is confirmed that the weight coefficients (w_1, w_2) are applied separately in the transient and steady-state responses. In terms of temperature estimation performance, the optimization method has less error than the non- optimization method. Therefore, in this paper, the transient and steady-state temperature errors are reduced by adding the initial modeling task, which optimizes the parameters heat capacity ratio $\hat{k}_{capa}$ and heat transfer coefficient ratio $\hat{k}_{conv}$ of the thermal equivalent circuit.

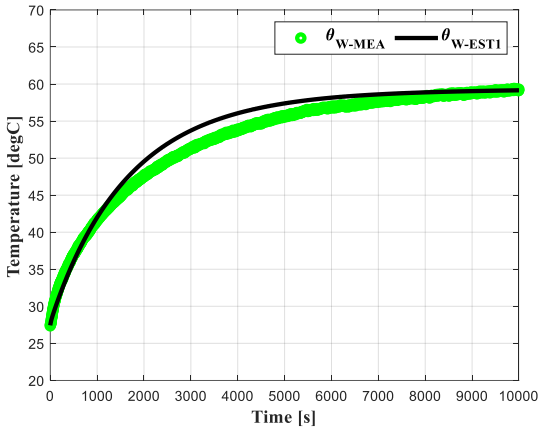

(a) winding temperature estmation (optimization x)

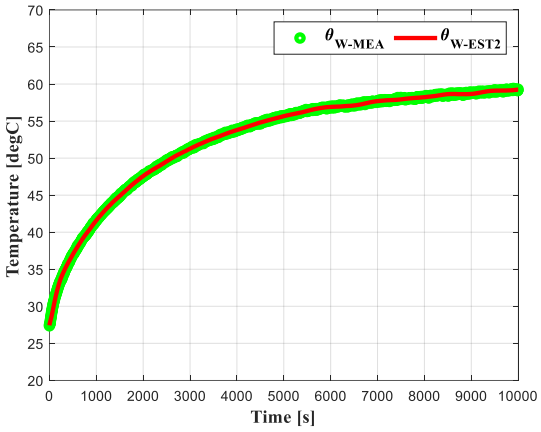

(b) winding temperature estmation (optimization o)

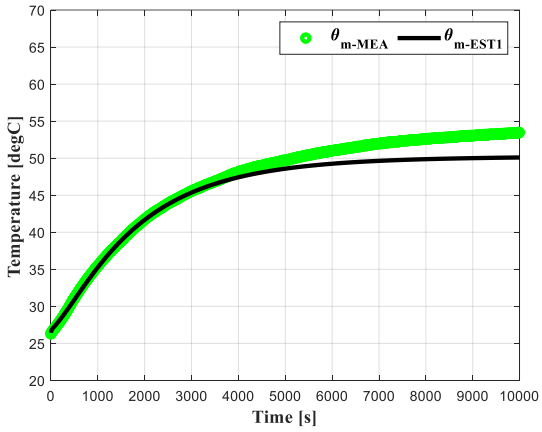

(c) magnet temperature estmation (optimization x)

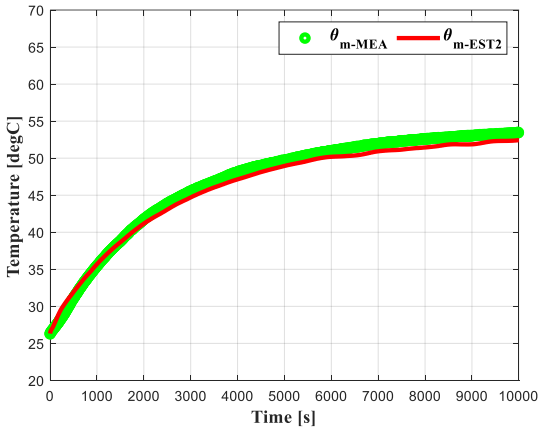

(d) magnet temperature estmation (optimization o)

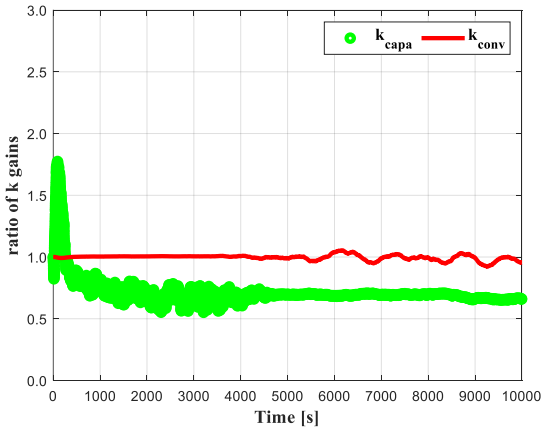

(e) Result of thermal component ratios

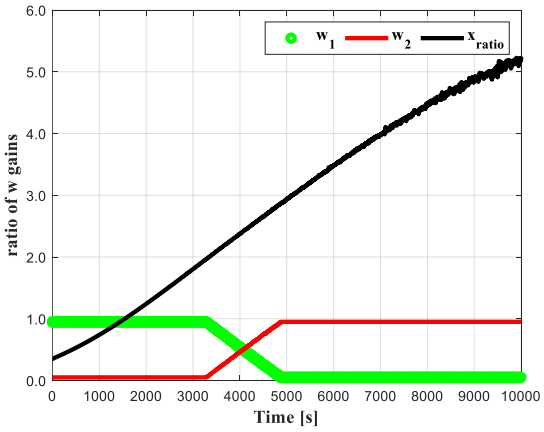

(f) Result of weight coefficients

Fig. 5.5 The experimental result of optimization of heat capacitance and heat transfer coefficient at Current 5A, Current angle 25deg, 1500min^{-1}

5.3 Experimental result of Thermal Equivalent Circuit

When estimating temperature using the thermal equivalent circuit, the accuracy of motor loss, which is the element of heat generation vector $\vec{\mathbf{Q}}_{\mathbf{th}}$, is very important. However, it is hard to obtain iron losses accurately in studies that use the magnetic circuit method or rules of thumb. One needs to find the distribution and time variations of the magnetic flux density in each part of motor after accounting for a fine geometry and the material's nonlinear magnetic properties. Iron losses are greatly changed in stator with large changes in magnetic flux density. The iron loss density is the largest at the end of the rotor core and the teeth of the stator, which are located close to the air gap. Unlike coil losses, iron loss has a small difference even if the current changes from 3 to 7A as shown in Fig. 5.6. The electric losses such as copper loss and iron losses are calculated for each driving condition such as the rotational speed and the stator current using the FEA, and the motor used in this paper is assumed to have no fan inside and no airflow outside the frame. Therefore, the convection heat transfer coefficients of outside the frame and inside the endcap, h_{frame} and h_{endcap}, are $16.5[W/m^2K]$ respectively.

Table 5.2 shows the parameters of proposed thermal equivalent circuit and Table 5.3 shows the experimental test condition of thermal equivalent circuit. The motor speed conditions are 1500 / 2000 / 2500 min^{-1} and the control current is 7A and current angle is from 25deg.

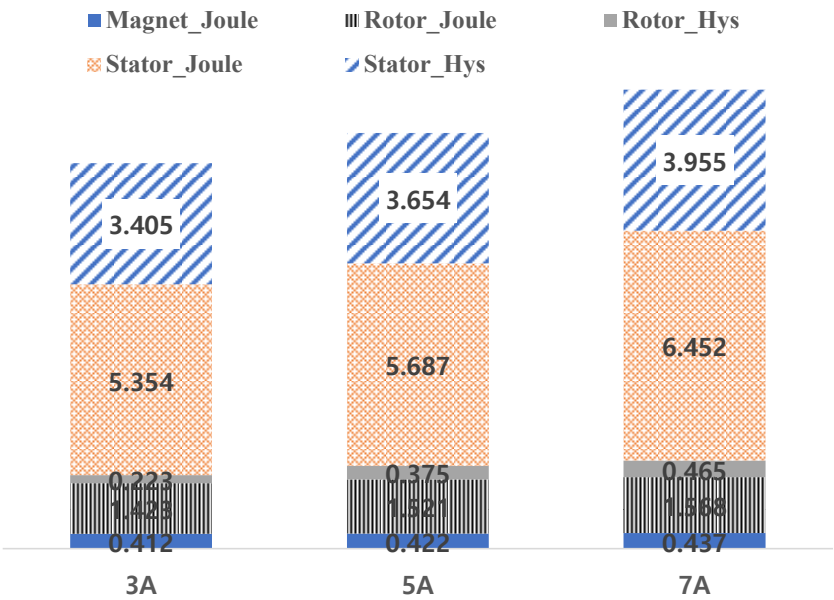

Fig. 5.6 The simulation result of iron loss using FEA, Current 3 / 5 / 7A, Current angle 25deg, 1500 min^{-1}

Fig. 5.7 shows the experimental result of thermal equivalent circuit at current 7A, current angle 25deg, 1500 / 2000 / 2500 min^{-1}. Even if FEA analysis creates a motor loss table, as shown in Fig. 5.6, the temperature error at 1500 min^{-1} increases by more than 5degC under transient conditions. The actual loss value needs to be slightly smaller than the simulated value. This thermal equivalent circuit needs to compensate for losses. This leads to the idea of combining flux linkage observer and thermal equivalent circuit. In the next chapter, the idea of combination method to estimate motor loss is described.

Table 5.2 Parameters of proposed thermal equivalent circuit

Parameters	**Value**
node	4
Heat capacitance PM / Rotor / Stator / Winding	44.17 / 340.2 / 1151 / 707.5 J/K
Heat transfer coefficient, h	16.5 W/m^2K
Heat capacitance ratio, k_{capa}	0.7073
Heat transfer coefficient ratio, k_{conv}	0.996
Motor loss at 1500 min^{-1}, PM / Rotor / Stator / Winding	3.955 / 0.2 / 6.452 / 66.15W

Table 5.3 Experimental Test Condition of thermal equivalent circuit

Condition	**Value**
Speed	1500 / 2000 / 2500 min^{-1}
Control current	7Amax
Current angle	25degree
Ambient temperature	25degC
Initial temperature	25degC

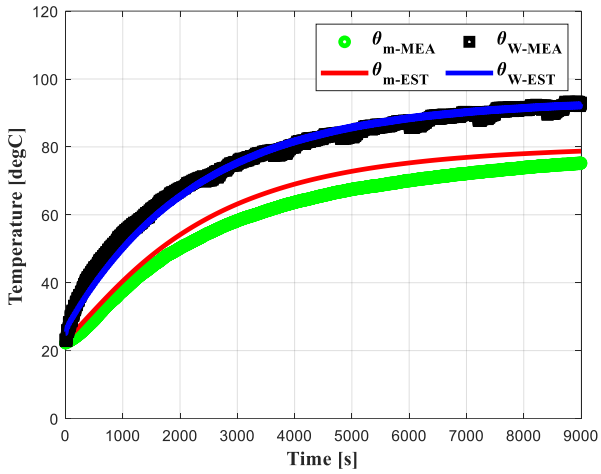

(a) Temperautre estimation of TEC at 1500 min^{-1}

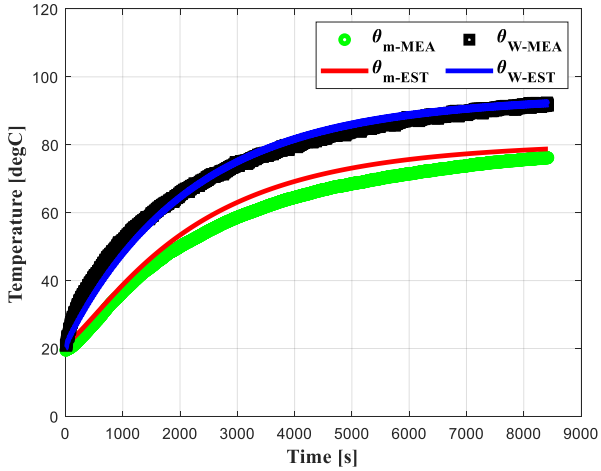

(b) Temperautre estimation of TEC at 2000 min^{-1}

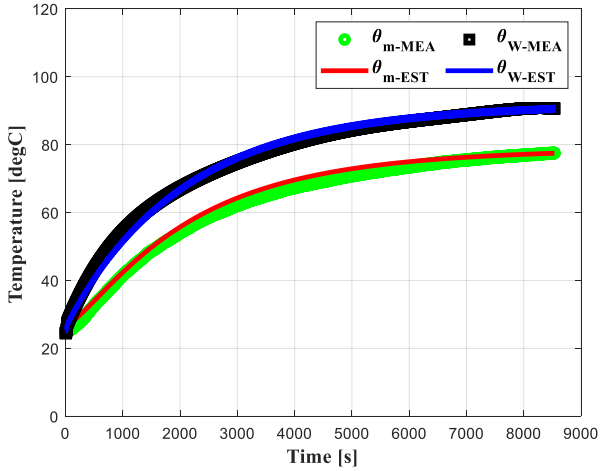

(c) Temperautre estimation of TEC at 2500 min^{-1}

Fig. 5.7 The experimental result of thermal equivalent circuit at Current 7A, Current angle 25deg, 1500 / 2000 / 2500 min^{-1}

Chapter 6 Proposed Magnet Operating Point Estimation

6.1 Magnet and stator iron loss estimation

In this chapter, the idea of combination method to estimate motor loss is described. The magnet loss and stator iron loss estimation are proposed as shown in Fig. 6.1. Since the computation of motor loss is difficult in real time, it has been proposed to estimate the losses by comparing the estimated magnet temperature of the flux linkage observer and the measured winding temperature with the estimate values of the thermal equivalent circuit.

(1) The estimated magnet temperature by Flux linkage observer $\hat{\theta}_{m-FO}$ and the estimated magnet temperature by thermal equivalent circuit $\hat{\theta}_m$ are compared.
(2) The measured winding temperature θ_w and the estimated winding temperature by thermal equivalent circuit $\hat{\theta}_w$ are compared.

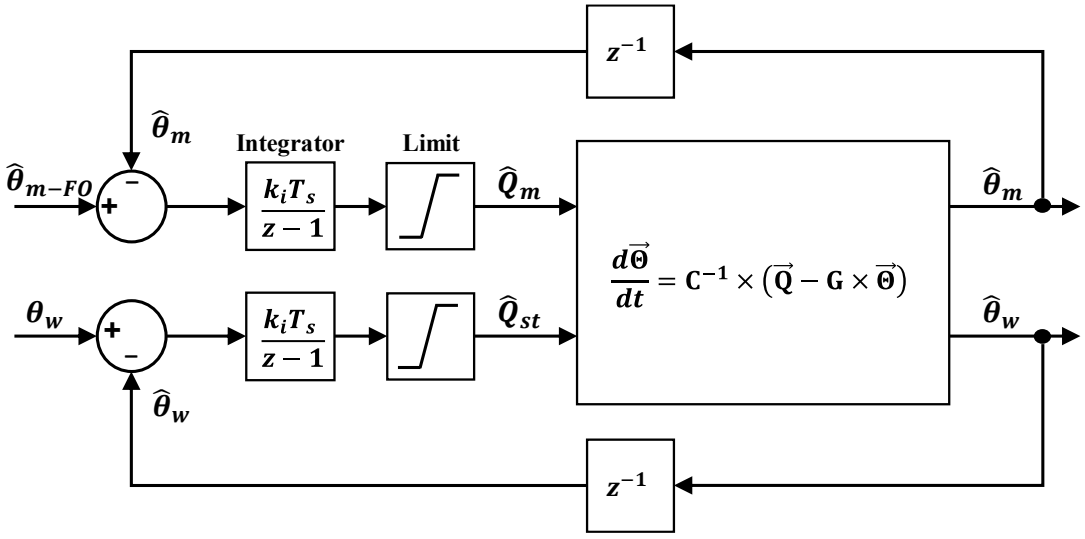

Fig. 6.1 Proposed magnet loss and stator iron loss estimation

(3) The magnet loss, $\hat{Q}_m$, is estimated by integrator and limit function of difference between $\hat{\theta}_{m-FO}$ and $\hat{\theta}_m$.

(4) The stator iron loss, $\hat{Q}_s$, is estimated by integrator and limit function of difference between θ_w and $\hat{\theta}_w$.

(5) The estimated magnet loss $\hat{Q}_m$ and estimated stator iron loss $\hat{Q}_s$ are updated into a differential matrix equation Eq. (5.8).

(6) Finally, the estimated temperatures of thermal equivalent circuit, $\hat{\theta}_m$ and $\hat{\theta}_w$ are compensated by estimated loss values.

6.2 Proposed Magnet Operating Point Estimation

In this paper, using the measured winding temperature, the magnet operation point estimation can be designed as a more accurate and error-resistant estimation method. In a thermal equivalent circuit, thermal capacitance, and thermal resistance, which are components of the circuit, may not be the correct or fixed values. To overcome these drawbacks, an easily measurable temperature of the stator winding is used in this paper.

The combination of three methods to estimate the operating point of permanent magnet is proposed as shown Fig. 6.2. To avoid interference, the flux link observer and the equivalent circuits are combined independently. First, the magnet temperature estimation is compensated for the initial temperature and magnet loss by using the error between the estimated temperature by thermal equivalent circuit and the estimated temperature by flux observer. In addition, stator iron loss is also compensated using the error between the measured temperature and the estimated temperature by thermal equivalent circuit. The method of estimating the magnetic flux density of a permanent magnet is designed to estimate the magnetic flux density of the motor using a magnetic equivalent circuit reflecting the value of the measured magnet temperature and magnetic flux density on the permanent magnet's B-H curve. The proposed method can estimate the magnet operating point in real time, considering the magnetic nonlinearity, motor losses and temperature variation of the IPMSM.

The overall process of proposed magnet operating point estimation is described below.

■ Magnet temperature estimation $\hat{\theta}_m$

(1) Initial modeling task: heat capacity ratio $\hat{k}_{capa}$ and heat transfer coefficient ratio $\hat{k}_{conv}$ of the thermal equivalent circuit (Optimization) and the initial flux linkage of magnet λ_{m0} is stored and used in the look-up table (LUT).

(2) The voltage is compensated using dead-time compensation.

(3) The currents are sampled additionally at T_s and T_1.

(4) The resistance $\hat{R}_s$ is calculated by measured winding temperature θ_w .

(5) The flux linkage of magnet $\hat{\lambda}_m$ are estimated by estimated current from Eq. (4.11).

(6) using Eq. (4.22), the magnet temperature $\hat{\theta}_{m-FO}$ is estimated by estimated flux linkage of magnet.

(7) The estimated magnet temperatures, $\hat{\theta}_{m-FO}$(FO) and $\hat{\theta}_m$(TEC), are compared, and the measured winding temperature θ_w and the estimated winding temperature by thermal equivalent circuit $\hat{\theta}_w$ are compared.

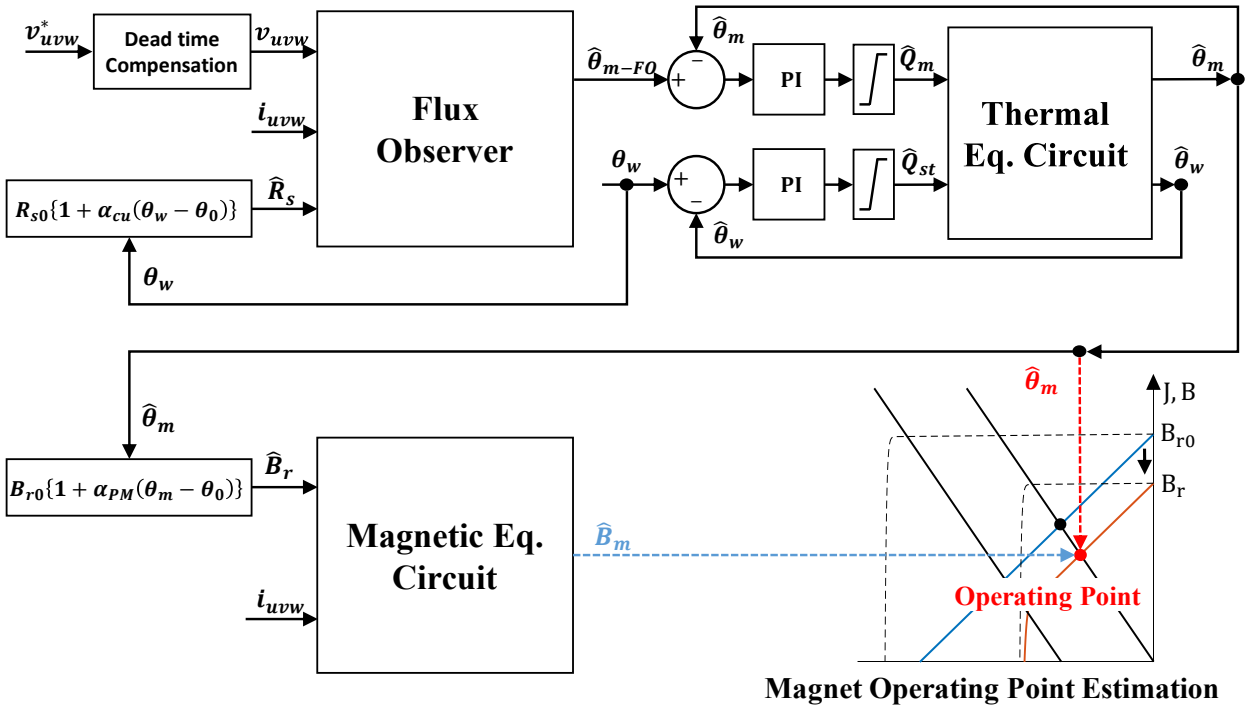

Fig. 6.2 Block diagram of proposed magnet operating point Estimation

(8) The magnet loss $\hat{Q}_m$ and the stator iron loss $\hat{Q}_s$ are estimated by integrator and limit function and they are updated into a differential matrix equation Eq. (5.8).

(9) The estimated temperatures of thermal equivalent circuit, $\hat{\theta}_m$ and $\hat{\theta}_w$ are compensated by estimated loss values.

■ Magnetic flux density of magnet estimation $\hat{B}_m$

(1) Solve the inverse of the obtained magnetic permeance matrix $\mathbf{P^{-1}}$.

(2) Convert to magnetic flux source by instantaneous current of stator winding $\boldsymbol{\phi_{s,w}}$.

(3) Convert to magnetic flux source by permanent magnet $\boldsymbol{\phi_{s,m}}$ using the residual flux density $\boldsymbol{B_r}$ changed by the magnet temperature $\hat{\theta}_m$.

(4) Magnetic potential of each node $\overrightarrow{\mathbf{F}}$ is obtained by multiplying the magnetic flux source vector $\overrightarrow{\boldsymbol{\Phi}_\mathbf{s}}$ by the inverse permeance matrix $\mathbf{P^{-1}}$.

(5) Calculate the magnetic flux $\phi_{i,j}$ and the magnetic flux density $B_{i,j}$ flowing through each branch.

(6) Determine the magnetic permeability $\mu_{i,j}$ according to this magnetic flux density $B_{i,j}$ (using the B-H curve of the stator core and rotor core).

(7) Recalculate the magnetic permanence matrix **P** using the magnetic permeability obtained $\{\mu\}$.

(8) Repeat 1 to 7 until the residuals of magnetic permeability are satisfied.

■ Magnet operating point estimation

(1) The magnetic flux density of magnet, $\hat{B}_m$, estimated by the magnetic equivalent circuit

(2) The magnet temperature, $\hat{\theta}_m$, estimated by the thermal equivalent circuit compensated with magnet loss and stator iron loss

(3) The magnet operating point is a value on the demagnetization B-H Curve, as defined by the temperature.

6.3 Experimental result of proposed magnet operating point estimation

In this section, the effectiveness of the proposed method is verified by experimental result. The temperature measurement system is necessary for rotating magnet. The motor temperatures measured on the 4 points of the rotor and the 4 points of the stator. Initial modeling task is completed. It is that optimization of heat capacity ratio $\hat{k}_{capa}$ and heat transfer coefficient ratio $\hat{k}_{conv}$ of the thermal equivalent circuit and the storage look-up table of initial flux linkage of magnet λ_{m0}. The specification and test condition are shown in Table 6.1 and Table 6.2. The motor speed conditions are 1500 / 2000 / 2500 min^{-1} and the control current is 7A and current angle is 25deg. Fig. 6.3 shows the back-emf voltage measured with temperature at no load.

Table 6.1 Motor Specification of magnet operating point estimation

Parameters	**Value**
Winding form	Distributed
Phase connection	Wye
Slots / Poles	24 / 4
Number of turns	140
Phase resistance	0.9 Ω
B_r	1.018 T
B_r - α_{PM} (measured)	-0.08384 · 10^{-2}
λ_m - α_m (measured)	-0.09125 · 10^{-2}
Magnetic flux linkage (no load)	0.08970 Wb

Table 6.2 Experimental Test Condition of magnet operating point estimation

Condition	**Value**
Speed	1500 / 2000 / 2500 min^{-1}
Control current	7Amax
Current angle	25degree
Ambient temperature	25degC
Initial temperature	25degC

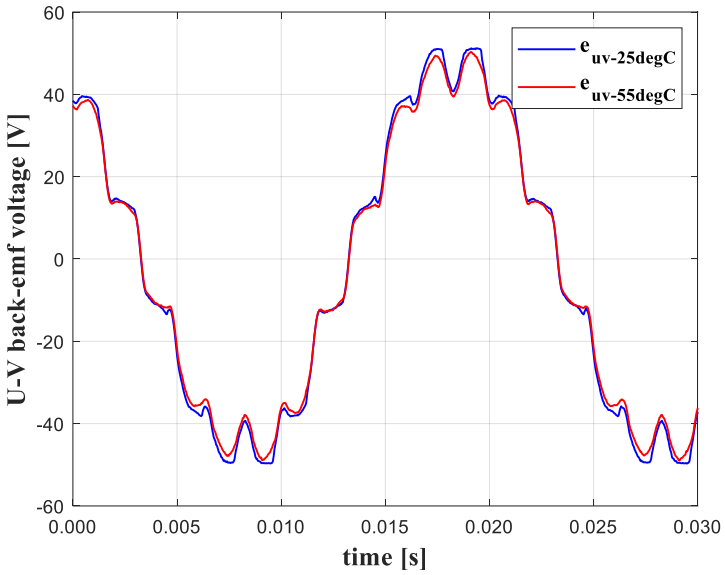

Fig. 6.3 The measured back-emf voltages with temperature at no load

6.3.1 Magnetic Flux Density Estimation Result

The estimated magnetic flux density of magnet $\hat{B}_m$ and the estimated residual magnetic flux density of magnet, $\hat{B}_r$ are shown in Fig. 6.4. As expected, the magnetic flux density of permanent magnet decreases as magnet temperature increases. Analysis based on the magnetic equivalent circuit has the advantage of being able to estimate magnetic flux in real time. The proposed magnetic equivalent circuit reflected changes in the residual flux density according to the magnet temperature, using the temperature estimated by the thermal equivalent circuit, to consider the effect on the magnet temperature.

6.3.2 Magnetic Flux Linkage Observer Result

As shown in Fig. 6.5, the magnetic flux linkage of magnet $\hat{\lambda}_m$ decreases proportionally as magnet temperature increases. Fig. 6.5 (a), (c) and (e) show the experimental results of the estimated inductance. The inductance values rise slightly at magnet temperature 75degC. Fig. 6.5 (b), (d) and (f) show the results of experiments in estimated magnetic flux linkage of magnet. These results confirm that the reduction in flux linkage of magnet due to temperature is large and proportional, as shown in Eq. (4.20). As a result, the estimated magnetic flux linkage of magnet is converted to the temperature of the permanent magnet using Eq. (4.22).

6.3.3 Magnet Temperature Estimation Result

An additional advantage of the proposed method is that it is possible to estimate the loss of magnets and iron cores that are not easy to obtain accurately. Fig. 6.6 (a), (c) and (e) show the result of the loss estimation. It is confirmed that the estimated stator loss oscillates in a particular frequency form in the transient response state and the steady-state response confirms that the estimated loss differs from the value computed by FEA. These results show that the magnet loss should be less than the simulation value.

Despite its many advantages, thermal models are highly dependent on the geometry of the motor and cooling system and operating speed. Therefore, specific design and calibration are often required to increase the accuracy of temperature estimates. Especially in transient state, thermal capacitances are important because of the large amount of change in temperature. This vibration can occur because of the error in the thermal capacitance of thermal equivalent circuit. On the other hand, the change in temperature is small in steady-state responses and the thermal resistance is important. Therefore, it is necessary to identify exact thermal capacitance C_{th} for transient response and exact heat transfer coefficient h for steady-state response. In this paper, the optimization of heat capacity ratio and heat transfer coefficient ratio is proposed for the initial modeling task.

The estimated temperature and the measured temperature of magnet, θ_m and loss estimation results are shown in Fig. 6.6 (b), (d) and (f). As the speed increases, the temperature of the stator and magnet can be seen to increase. The error of temperature is $|\Delta\boldsymbol{\theta}_m| < 2.0\ \mathrm{degC}$ and appears to be following the trend of slope. This result means that the magnetic flux linkage λ_m estimation is equivalent to indirectly measuring the magnet temperature using look-up table of initial flux linkage of magnet and it demonstrates the effectiveness of magnet and stator loss estimation.

6.3.4 Magnet Operating Point Estimation Result

Finally, the estimation result of the magnet operating points is shown in Fig. 6.7. The operating point of the measured temperature are compared with the estimated result to determine the performance of the operating point estimation. Compared to the FEA results, the error of magnetic flux density $|\Delta\boldsymbol{B}_m| < 0.05$ [T]. Since magnetic equivalent circuit is a lumped method, magnetic flux calculation is approximate. On the other hand, finite element analysis has precise meshes and many iterations number. In addition, it considers nonlinear behavior, skin effect and etc. Therefore, it is reasonable that the FEA results differ by about 5% from the estimated magnet operating point results.

The magnet operating point is a value on the demagnetization B-H Curve, as defined by the temperature. Using the proposed method, the magnetic flux density of magnet $\hat{B}_m$ and magnet temperature $\hat{\theta}_m$ are estimated in real time. As a result, the proposed method has been experimentally verified to estimate magnetic operating points in real time, considering the magnetic nonlinearity and temperature changes of IPMSM.

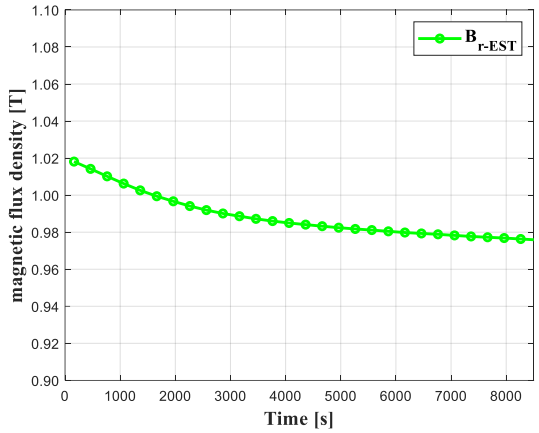

(a) Estmated residual magnetic flux density of PM at 1500 min^{-1}

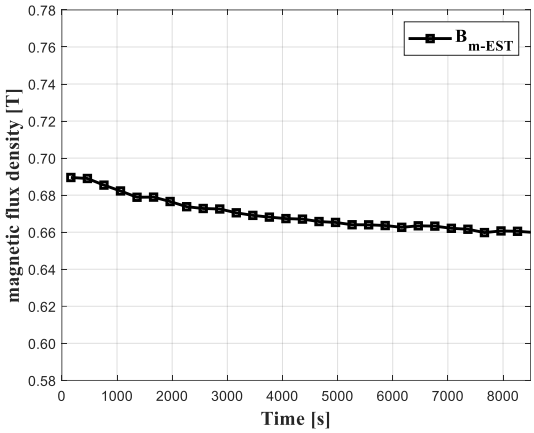

(b) Estmated magnetic flux density of PM at 1500 min^{-1}

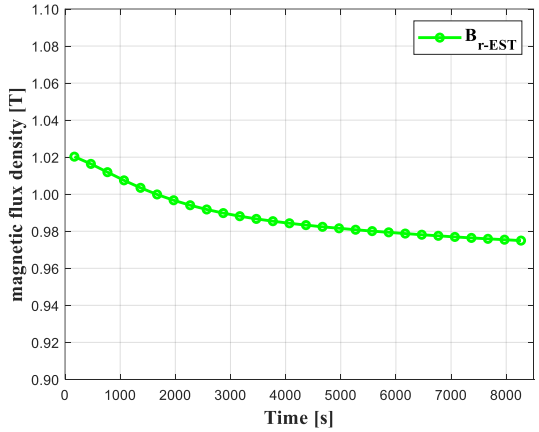

(c) Estmated residual magnetic flux density of PM at 2000 min^{-1}

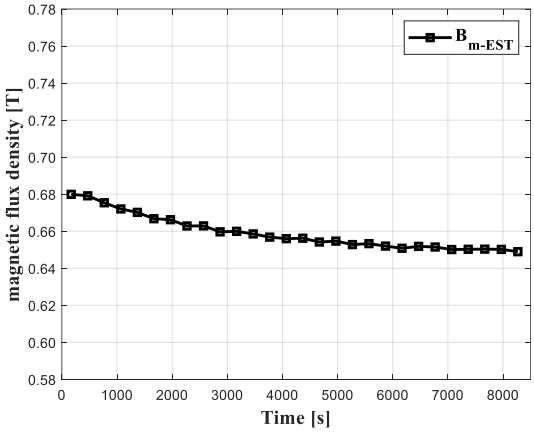

(d) Estmated magnetic flux density of PM at 2000 min^{-1}

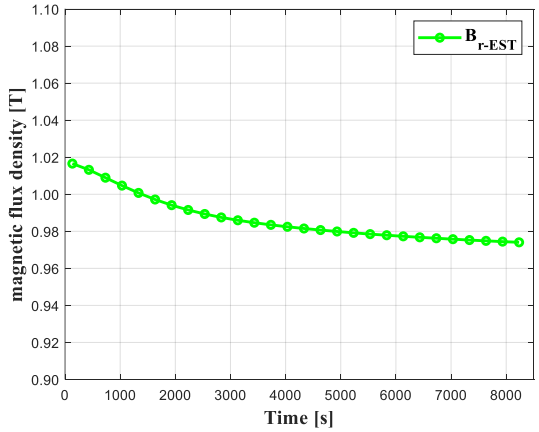

(e) Estmated residual magnetic flux density of PM at 2500 min^{-1}

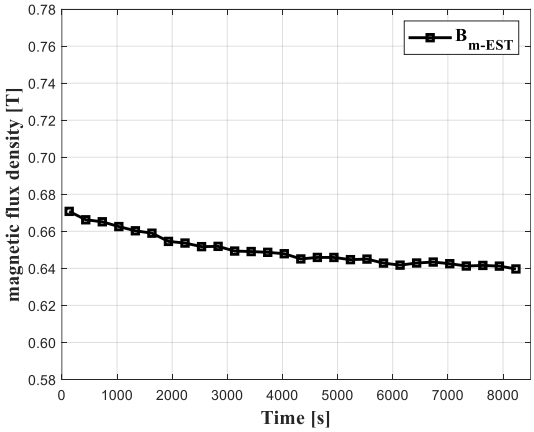

(f) Estmated magnetic flux density of PM at 2500 min^{-1}

Fig. 6.4 The experimental result of the proposed magnetic flux density estimation at Current 7A, Current angle 25deg, 1500 / 2000 / 2500 min^{-1}

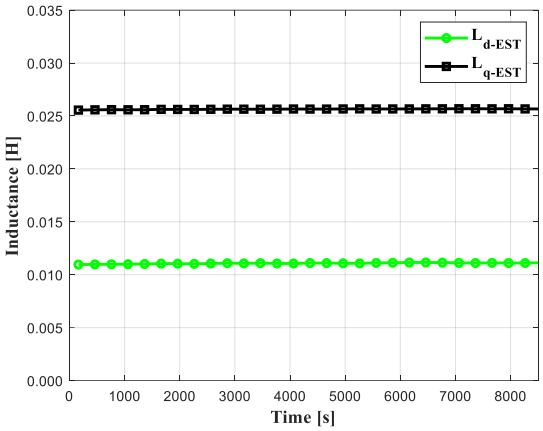

(a) Estmated inductance at 1500 min^{-1}

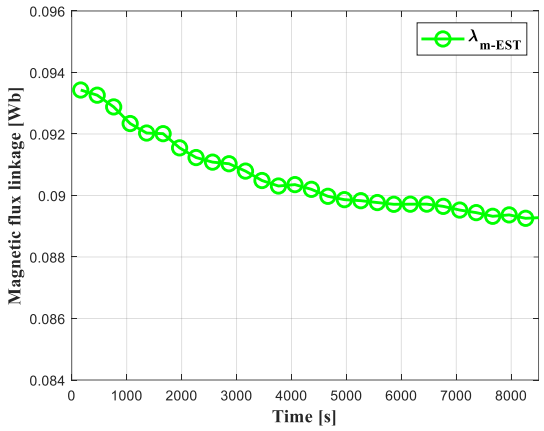

(b) Estmated flux linkage of magnet at 1500 min^{-1}

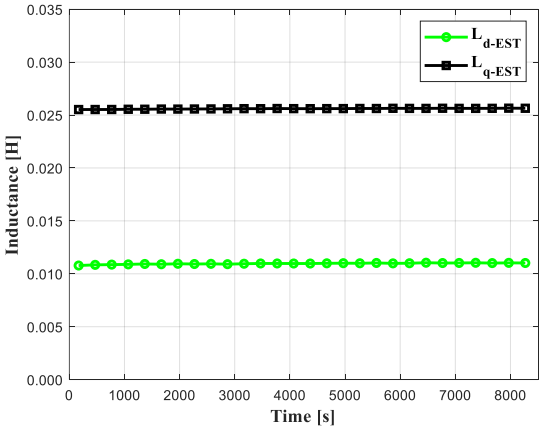

(c) Estmated inductance at 2000 min^{-1}

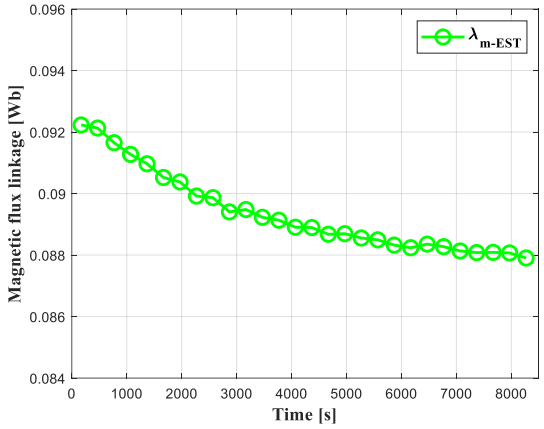

(d) Estmated flux linkage of magnet at 2000 min^{-1}

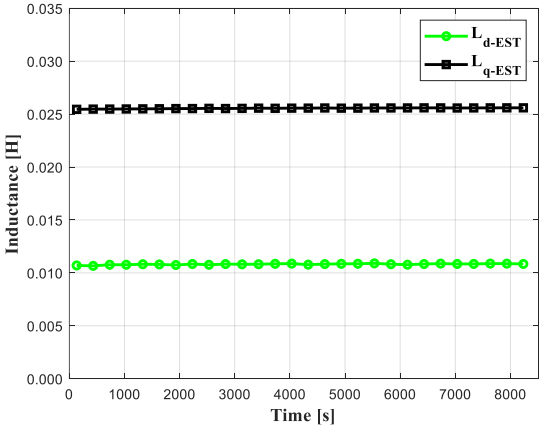

(e) Estmated inductance at 2500 min^{-1}

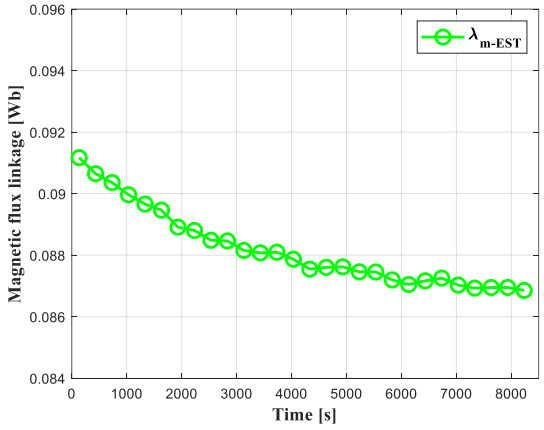

(f) Estmated flux linkage of magnet at 2500 min^{-1}

Fig. 6.5 The experimental result of the magnetic flux linkage observer at Current 7A, Current angle 25deg, 1500 / 2000 / 2500 min^{-1}

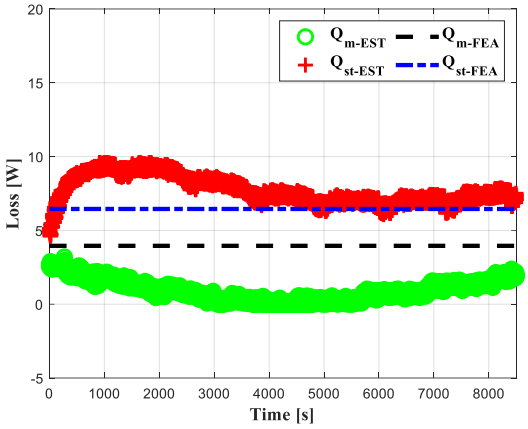

(a) Estmated losses at 1500 min^{-1}

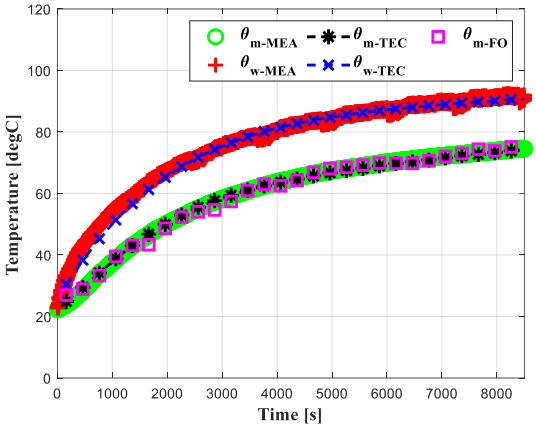

(b) Estmated temperature at 1500 min^{-1}

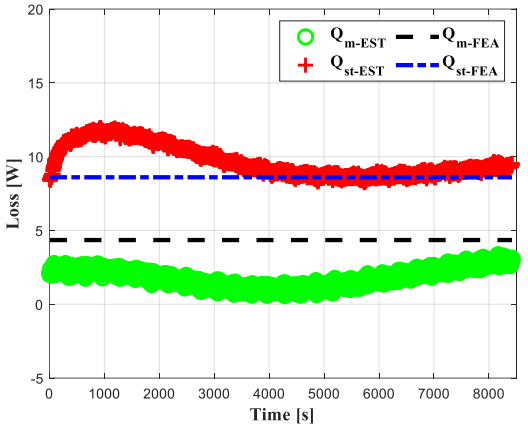

(c) Estmated losses at 2000 min^{-1}

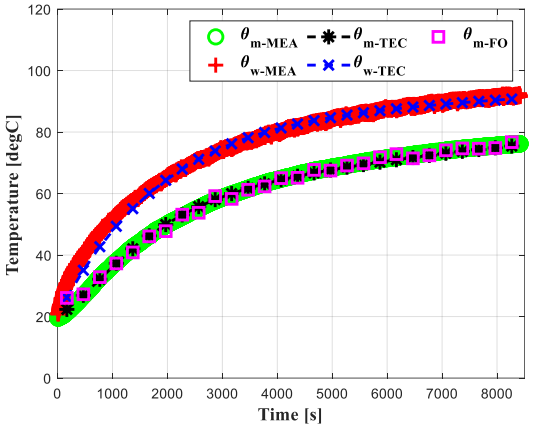

(d) Estmated temperature at 2000 min^{-1}

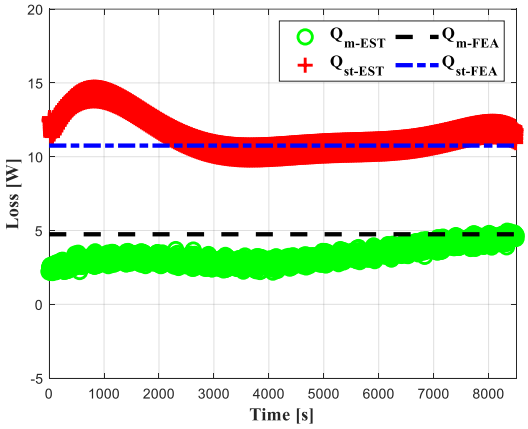

(e) Estmated losses at 2500 min^{-1}

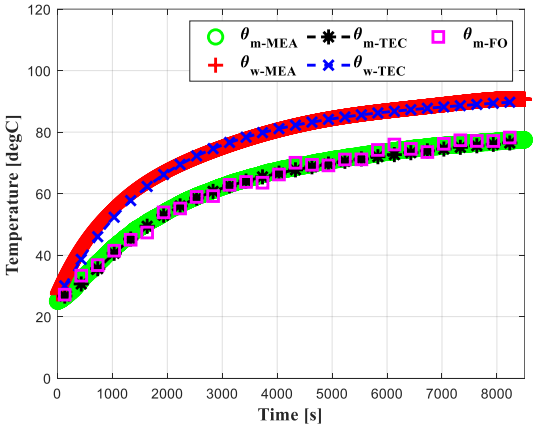

(f) Estmated temperature at 2500 min^{-1}

Fig. 6.6 The experimental result of the proposed magnet temperature estimation at Current 7A, Current angle 25deg, 1500 / 2000 / 2500 min^{-1}

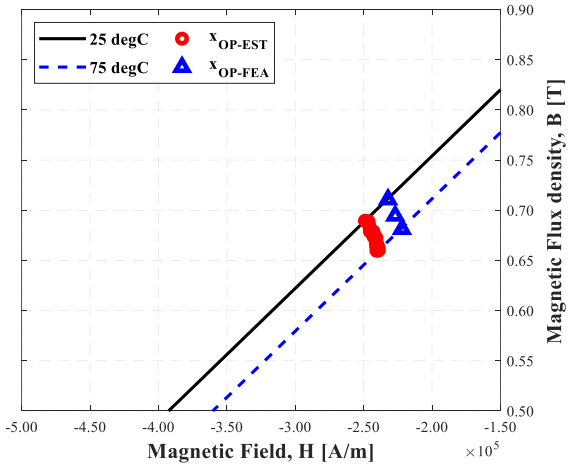

(a) Estmated magnet operating point estimation at 1500 min^{-1}

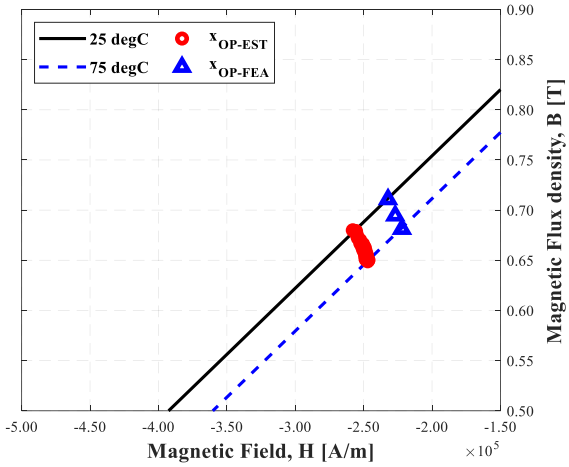

(b) Estmated magnet operating point estimation at 2000 min^{-1}

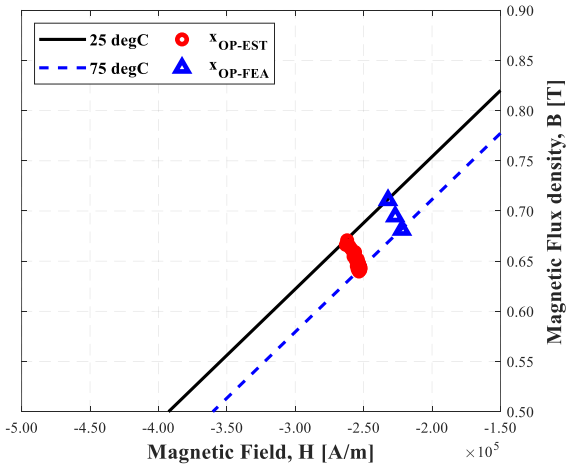

(c) Estmated magnet operating point estimation at 2500 min^{-1}

Fig. 6.7 The experiment result of proposed magnet operating point estimation at Current 7A, Current angle 25deg, 1500 / 2000 / 2500 min^{-1}

Chapter 7 Conclusion

7.1 Conclusion of this paper

For the stable and efficient operation of IPMSM, a new method of the magnet operating point estimation has been proposed in this paper. An effective combination of the methods to estimate the magnet operating points has been introduced for more accurate estimation performance. The special features are that all of three methods, which are magnetic equivalent circuit, thermal equivalent circuit, and flux linkage observer are connected with magnetic flux linkage of magnet.

First, a method of estimating the magnetic flux density of a permanent magnet is designed to estimate using a magnetic equivalent circuit reflecting the value of the estimated magnet temperature. Second, the proposed flux linkage observer is that motor parameters can be estimated independently using the modified model reference adaptive system with additional current sampling points. Finally, the magnet temperature estimation is compensated with the estimated magnet loss based on the error between the estimated magnet temperature obtained using the thermal equivalent circuit and the estimated magnet temperature obtained using the flux linkage observer. The stator iron loss is also compensated based on the error between the measured winding temperature and estimated winding temperature obtained using the thermal equivalent circuit.

Unlike the rotor temperature, the stator and winding temperature can be easily measured, and the magnet operating point estimation can be designed as a more accurate and error-resistant estimation method. The effect of the change in the stator resistance, which varies with winding temperature, is essentially eliminated, and the effect from inverter nonlinearity is also minimized by dead-time compensation. In addition, proposed method compensates nonlinearity problem of magnetic characteristics and magnet temperature characteristics using magnetic and thermal equivalent circuit. Therefore, the magnet operating point is estimated in real-time at the estimated magnetic flux density $\hat{B}_m$, and the estimated temperature $\hat{\theta}_m$. The proposed method in this paper aims at estimating in medium and high-speed region above 1500 min^{-1}, 50Hz. Thus, the magnet operating point estimation performance at speeds of 1500 / 2000 / 2500 min^{-1} has been confirmed by experimental results. The simulation and experimental verification demonstrate the

effectiveness of the proposed method. The error of temperature is $|\Delta\boldsymbol{\theta}_m| < 2.0$ deg (< 5%) and appears to be following the trend of slope. The error of magnetic flux density $|\Delta\boldsymbol{B}_m| < 0.05$ [T] (< 5%).

7.2 Complementary points and the future task

In this paper, the complementary points for the next study are as follows.

(1) The proposed magnet operating point estimation has been demonstrated on constant current and speed conditions. The effectiveness of the proposed method may require more verification of other conditions, such as various loads or temperature conditions. Further studies are needed to satisfy the estimation performance of low-speed region under 1500 min^{-1}.

(2) The temperature of the permanent magnet is measured by non-contact measurement data transmission device using RF communication, but the magnetic flux density could not be measured directly. To verify the magnetic flux density of permanent magnet, additional sensing devices, such as non-contact device of magnetic flux sensor, should be supplemented.

(3) It is assumed that the B-H characteristics of electrical steel plates are constant according to temperature. However, in practice, temperature estimation may be necessary considering the B-H characteristics change slightly depending on the temperature of the electric steel plate.

Based on this study, the future tasks are as follows.

(1) The proposed method is relatively simple and can identify the operating point of the permanent magnet in real time. Therefore, it is expected that this study will help in terms of the protective logic design for permanent magnet and an improvement of efficiency in PMSM.

(2) Using the estimated temperature and magnetic flux density of the magnet, moving the magnet operating point can improve the precision of the torque control and the efficiency of the system.

(3) Deep learning can be used to optimize magnet temperature and flux density estimation methods. This learning technology enables the development of accurate and simple methods of temperature estimation. This requires the development of data and appropriate models that require sufficient learning.

Appendix

■ Inverse Permeance Matrix for Magnetic Equivalent Circuit

The magnetic equivalent circuit used in this paper can be represented as shown in Fig. A1. where p is the magnetic permeance, F_m is the MMF of the magnet, F_w is the MMF by the flowing current to the armature winding. p_y is the magnetic permeance of stator back yoke, and p_t is that of stator teeth, p_g is that of airgap. p_{cd} and p_{cq} are the magnetic permeance of rotor core in the d-q reference frame, and p_m is that of the magnet. p_{tt} is the magnetic permeance between stator

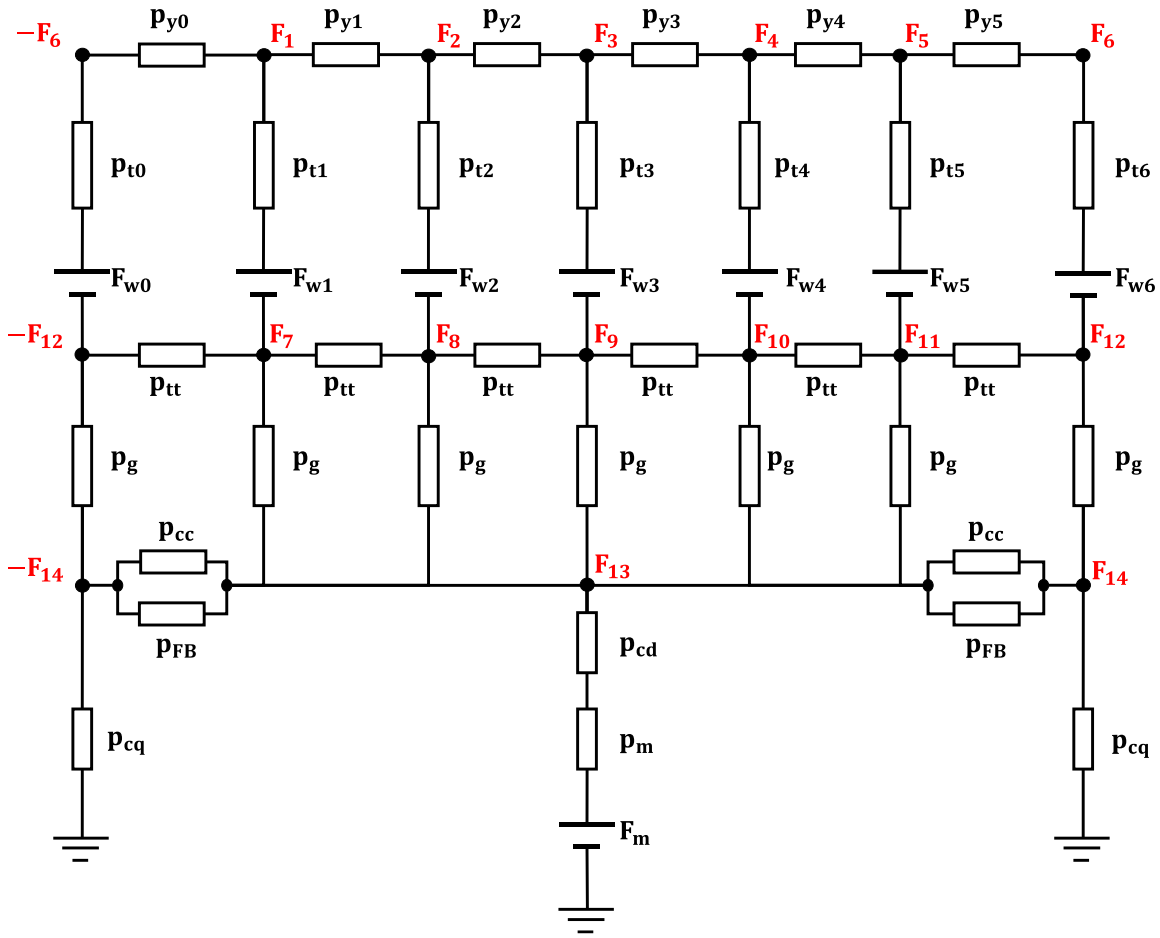

Fig. A1. Magnetic Equivalent Circuit for IPMSM

teeth and teeth, p_{cc} is the value between rotor core and core, and p_{FB} is the value of the rotor flux barrier. To solve this circuit in real time, the magnetic equivalent circuit can be mathematically converted into a matrix equation through the Nodal-analysis.

$$\mathbf{P} \times \vec{\mathbf{F}} = \vec{\mathbf{\Phi}}_{\mathbf{s}} \tag{0.1}$$

Where $\mathbf{P}$ is the magnetic permeance matrix, $\vec{\mathbf{F}}$ is the magnetic potential (MMF) vector of the nodes, and $\vec{\mathbf{\Phi}}_{\mathbf{s}}$ is the magnetic flux source vector.

$$\mathbf{P} = \mathbf{P}^{\mathrm{T}} = \begin{bmatrix} \vec{\mathbf{p}}_{\mathbf{1}} & \vec{\mathbf{p}}_{\mathbf{2}} & \cdots & \vec{\mathbf{p}}_{\mathbf{14}} \end{bmatrix}, \quad \vec{\mathbf{F}} = \begin{bmatrix} F_1 \\ F_1 \\ \vdots \\ F_{13} \\ F_{14} \end{bmatrix}, \quad \vec{\mathbf{\Phi}}_{\mathbf{s}} = \begin{bmatrix} \Phi_{s1} \\ \Phi_{s2} \\ \vdots \\ \Phi_{s13} \\ \Phi_{s14} \end{bmatrix} = \begin{bmatrix} p_{t1} \cdot F_{w1} \\ p_{t2} \cdot F_{w2} \\ \vdots \\ p_m \cdot F_m \\ 0 \end{bmatrix}$$

The magnetic flux density is calculated to solve inverse permeance matrix $\mathbf{P^{-1}}$ and solving magnetic potential and flux values. To solve this inverse matrix, the direct inverse matrix solution, Gauss-Jordan elimination method, which is generally used when there are fewer nodes, are used, whereas when there are many nodes and complex calculations are required, Gauss-Seidel methods are used using repetition and residuals. In this paper, the number of nodes is 14, which is relatively small, so Gauss-Jordan elimination method is used.

$$\vec{\mathbf{F}} = \mathbf{P}^{-1} \times \vec{\mathbf{\Phi}}_{\mathbf{s}} \tag{0.2}$$

In order to obtain the inverse matrix of $\mathbf{P}$ using Gauss-Jordan elimination method, the singularity of the matrix must be determined. As shown in Fig. A2, it is easy to confirm that permeance matrix $\mathbf{P}$ is the square matrix of order 14, and it is symmetric with the dominant diagonal component and linearly independent.

$$\begin{aligned} &\alpha_1 \vec{\mathbf{p}}_{\mathbf{1}} + \alpha_2 \vec{\mathbf{p}}_2 + \cdots + \alpha_{14} \vec{\mathbf{p}}_{14} = 0 \ \left(\alpha_k \in \mathbb{R}\right) \\ &\rightarrow \alpha_1 = \alpha_2 = \cdots = \alpha_{14} = 0 \end{aligned} \tag{0.3}$$

Therefore, the rank of **P** is as follows.

$$\mathrm{rank}\left(\mathbf{P}\right)=14 \tag{0.4}$$

The order is 14, so it is equivalent as below [41].

$$\det\left(\mathbf{P}\right)\neq 0 \tag{0.5}$$

Therefore, it is confirmed that P is not singularity in this paper and the inverse matrix can be obtained as Gaussian-Jordan elimination method.

$$
\begin{bmatrix}
p_{y1}+p_{y0}+p_{t1} & -p_{y1} & & & & +p_{y0} & -p_{t1} & & & & & & & & & & & & & \\
-p_{y1} & p_{y2}+p_{y1}+p_{t2} & -p_{y2} & & & & & -p_{t2} & & & & & & & & & & & & \\
 & -p_{y2} & p_{y3}+p_{y2}+p_{t3} & -p_{y3} & & & & & -p_{t3} & & & & & & & & & & & \\
 & & -p_{y3} & p_{y4}+p_{y3}+p_{t4} & -p_{y4} & & & & & -p_{t4} & & & & & & & & & & \\
 & & & -p_{y4} & p_{y5}+p_{y4}+p_{t5} & -p_{y5} & & & & & -p_{t5} & & & & & & & & & \\
+p_{y0} & & & & -p_{y5} & p_{y0}+p_{y5}+p_{t6} & & & & & & -p_{t6} & & & & & & & & \\
-p_{t1} & & & & & & p_{t1}+2p_{tt}+p_g & -p_{tt} & & & & & +p_{tt} & -p_g & & & & & & \\
 & -p_{t2} & & & & & -p_{tt} & p_{t2}+2p_{tt}+p_g & -p_{tt} & & & & & -p_g & & & & & & \\
 & & -p_{t3} & & & & & -p_{tt} & p_{t3}+2p_{tt}+p_g & -p_{tt} & & & & -p_g & & & & & \\
 & & & -p_{t4} & & & & & -p_{tt} & p_{t4}+2p_{tt}+p_g & -p_{tt} & & & -p_g & & & & \\
 & & & & -p_{t5} & & & & & -p_{tt} & p_{t5}+2p_{tt}+p_g & -p_{tt} & & -p_g & & & \\
 & & & & & -p_{t6} & +p_{tt} & & & & -p_{tt} & p_{t6}+2p_{tt}+p_g & & & -p_g & & \\
 & & & & & & -p_g & -p_g & -p_g & -p_g & -p_g & & 5p_g+2p_{cc}+2p_{FB}+p_m & & & \\
 & & & & & & & & & & & -p_g & & p_g+2p_{cc}+2p_{FB}+p_{cq} & &
\end{bmatrix}
$$

Fig. A2. Permeance matrix of magnetic equivalent circuit

References

[1] Amount of spent lithium-ion batteries from electric vehicles and storage in the Sustainable Development Scenario, 2020-2040, www.iea.org/t_c/termsandconditions/

[2] Y. Shimizu, S. Morimoto, M. Sanada, Y. Inoue, "Influence of Permanent Magnet Properties and Arrangement on Performance of IPMSMs for Automotive Applications", IEEJ Transactions on Industry Applications, Vol. 6, No. 6, pp. 401-408 (2017)

[3] K. Rajashekara, "Present status and future trends in electric vehicle propulsion technologies", IEEE J. Emerg. Sel. Topics Power Electron., vol. 1, no. 1, pp. 3-10, Mar. 2013

[4] Chen-Yen Yu, Takashi Fukushige, Natee Limsuwan, Takashi Kato, David Diaz Reigosa, Robert D. Lorenz, "Variable-flux machine torque estimation and pulsating torque mitigation during magnetization state manipulation", IEEE Trans. Ind Applications, Vol. 50, No. 5, pp. 3414-3422 (2014)

[5] P. Zhou, D. Lin, Y. Xiao, N. Lambert, M. A. Rahman, "Temperature-dependent demagnetization model of permanent magnets for finite element analysis", IEEE Trans. on Magnetics, Vol. 48, No. 2, pp. 1031-1034 (2012)

[6] Howard C. Lovatt, Peter A. Watterson, "Energy stored in permanent magnets", IEEE Trans. on Magnetics, Vol. 35, No. 1, pp. 505-507 (1991)

[7] S. Ruoho, J. Kolehmainen, J. Ikaheimo, A. Arkkio, "Interdependence of demagnetization, loading, and temperature rise in a permanent-magnet synchronous motor", IEEE Trans. on Magnetics, Vol. 46, No. 3, pp. 949- 953 (2010)

[8] M.-D. Calin and E. Helerea, "Temperature Influence on Magnetic Characteristics of NdFeB Permanent Magnets", in International Symposium on Advanced Topics in Electrical Engineering (ATEE) (2011)

[9] G. D. Demetriades, H. Z. D. L. Parra, E. Andersson, and H. Olsson, "A Real-Time Thermal Model of a Permanent-Magnet Synchronous Motor", IEEE Transactions on Power Electronics, Vol. 25, No. 2, pp. 463–474 (2010)

[10] S. Nategh, O. Wallmark, M. Leksell, and S. Zhao, "Thermal Analysis of a PMaSRM Using Partial FEA and Lumped Parameter Modeling," IEEE Transactions on Energy Conversion, Vol. 27, No. 2, pp. 477–488 (2012)

[11] T. Huber, W. Peters and J. Böcker, “A Low-Order Thermal Model for Monitoring Critical Temperatures in Permanent Magnet Synchronous Motors”, in International Conference on Power Electronics, Machines and Drives (PEMD) (2014)

[12] N. Simpson, R. Wrobel, and P. H. Mellor, “An accurate mesh-based equivalent circuit approach to thermal modeling,” IEEE Trans. Magnetics., vol. 50, no. 2, Art. no. 7006504 (2014)

[13] W. Wang, Y. Zhou, Y. Chen, “Investigation of Lumped-parameter Thermal Model and Thermal Parameters Test for IPMSM”, International Conference on Electrical Machines and Systems (ICEMS) (2014)

[14] A. Specht and J. B¨ocker, “Observer for the rotor temperature of IPMSM”, in Proc. IEEE Power Electron. Motion Control Conf., pp. T4-12–T4-15, 2010.

[15] A. Specht, O. Wallscheid, and J. B¨ocker, “Determination of rotor temperature for an interior permanent magnet synchronous machine using a precise flux observer”, in Proc. Int. Power Elect. Conf., pp. 1501–1507 (2014)

[16] O. Wallscheid, A. Specht, J. Böcker, “Observing the Permanent-Magnet Temperature of Synchronous Motors Based on Electrical Fundamental Wave Model Quantities”, IEEE Transactions on Industrial Electronics, Vol. 64, No. 5, pp. 3921-3929 (2017)

[17] D. D. Reigosa, F. Briz, P. Garcia, J. M. Guerrero, and M.W. Degner, “Magnet temperature estimation in surface PM machines using high-frequency signal injection,” IEEE Trans. Ind. Appl., Vol. 46, No. 4, pp. 1468–1475 (2010)

[18] D. Reigosa, D. Fernandez, H. Yoshida, T. Kato, and F. Briz, “Permanent magnet temperature estimation in PMSMs using pulsating high frequency current injection,” IEEE Trans. Ind. Appl., Vol. 51, No. 4, pp. 3159–3168 (2015)

[19] R. Mocanu, A. Onea, “Determination of stator temperature for thermal protection in a Permanent Magnet Synchronous Machine”, Mediterranean Conference on Control and Automation (MED) (2017)

[20] Min-Fu Hsieh, You-Chiuan Hsu, "A generalized magnetic circuit modeling approach for design of surface permanent-magnet machines," Industrial Electronics, IEEE Transactions on , vol.59, no.2, pp.779,792, Feb. 2012

[21] Zhu, Z.Q., Pang, Y., Howe, D., Iwasaki, S., Deodhar, R., Pride, A., "Analysis of electromagnetic performance of flux-switching permanent-magnet Machines by nonlinear adaptive lumped parameter magnetic circuit model," Magnetics, IEEE Transactions on , vol.41, no.11, pp.4277,4287, Nov. 2005

[22] Leboeuf N., Boileau T., Nahid-Mobarakeh B., Takorabet N., Meibody-Tabar F., Clerc G., "Inductance calculations in permanent-magnet motors under fault conditions," Magnetics, IEEE Transactions on , vol.48, no.10, pp.2605,2616, Oct. 2012

[23] Tangudu J.K., Jahns T.M., EL-Refaie A., Zhu Z.Q., "Lumped parameter magnetic circuit model for fractional-slot concentrated winding interior permanent magnet machines," Energy Conversion Congress and Exposition, 2009. ECCE 2009. IEEE , vol., no., pp.2423,2430, 20-24 Sept. 2009

[24] Rasmussen C.B., Ritchie E., "A magnetic equivalent circuit approach for predicting PM motor performance," Industry Applications Conference, 1997. Thirty-Second IAS Annual Meeting, IAS '97., Conference Record of the 1997 IEEE , vol.1, no., pp.10,17 vol.1, 5-9 Oct 1997

[25] D. J. Gómez, A. L. Rodríguez, I. Villar, A. López-de-Heredia, I. Etxeberria-Otadui, Z. Q. Zhu, "Improved permeance network model for embedded magnet synchronous machines", 2014 International Conference on Electrical Machines (ICEM), Vol., No., pp.1231-1237 (2014)

[26] P. Pillay and R. Krishnan, "Application characteristics of permanent magnet synchronous and brushless dc motors for servo drives", IEEE Transactions on Industry Applications, vol 27, no. 5, pp. 1005-1011, Sept./Oct. 1991.

[27] P. Pillay and R. Krishnan, "Application characteristics of permanent magnet synchronous and brushless dc motors for servo drives", in Conf. Rec. IEEEIAS Annual. Meeting, vol. 3, pp. 1814-1819, 2000

[28] Stephen J. Chapman, "Electric machinery fundamentals", 2005

[29] Ioan Dore Landau, Rogelio Lozano, Mohammed M'Saad, Alireza Karimi, "Adaptive Control, Algorithms, Analysis and Applications", Second Edition, pp 1-5, 2011

[30] T. Boileau, B. Nahid-Mobarakeh, F. Meibody-Tabar, "On-Line Identification of PMSM Parameters: Model-Reference vs EKF", 2008 IEEE Industry Applications Society Annual Meeting (2014)

[31] D. C. Lim and D. M. Lee, "A Noble Parameter Estimation Algorithm for Interior Permanent Magnet Synchronous Motors," The Trans. of KIPE vol. 18, no. 3, pp. 289-295, June 2013

[32] T. Boileau, N. Leboeuf, and B. Nahid-Mobarakeh, "Online identification of PMSM parameters: Parameter identifiability and estimator comparative study," IEEE Trans. on Ind. Appl. vol.47, no.4, pp. 1944-1957, July 2011.

[33] Hyunsuk Yang, “Parameter estimation of permanent magnet synchronous motor and adaptive control by MRAS”, Journal of the Korea Academia-Industrial cooperation Society, Vol. 17, No. 2 pp. 697-702, 2016

[34] S.Y. Kim, W. Lee, M. S. Rho, S. Y. Park, “Effective Dead-Time Compensation Using a Simple Vectorial Disturbance Estimator in PMSM Drives”, IEEE Transactions on Industrial Electronics, Vol. 52, No. 5, pp. 1609-1614, May 2010

[35] Tengfei Qiu, Xuhui Wen, Feng Zhao, “Adaptive-Linear-Neuron-Based Dead-Time Effects Compensation Scheme for PMSM Drives”, IEEE Transactions on Power Electronics, Vol. 31, No. 3, pp. 2530-2538, April 2015

[36] N. Urasaki, T. Senjyu, K. Uezato, T. Funabashi, “Adaptive Dead-Time Compensation Strategy for Permanent Magnet Synchronous Motor Drive”, IEEE Transactions on Energy Conversion, Vol. 22, No. 2, pp. 271-280, June 2007

[37] M. Calin and E. Helerea, "Temperature influence on magnetic characteristics of NdFeB permanent magnets," International Symposium On Advanced Topics In Electrical Engineering (ATEE), Bucharest, pp. 1-6 (2011)

[38] Frank P. Incropera, David P. Dewitt, Theodore L. Bergman, Adrienne S. Lavine, “Fundamentals of Heat and Mass Transfer”, Sixth Edition, pp. 2-12, 2005

[39] S.K. Chowdhury, P.K Baski, “A Simple Lumped Parameter Thermal Model for Electrical machine of TEFC Design”, Power Electronics, Drives and Energy Systems (PEDES) & 2010 Power India, 2010 Joint International Conference on, pp. 1~7 (2010)

[40] Z. J. Liu, K. J. Binns, and T. S. Low, “Analysis of eddy current and thermal problems in permanent magnet machines with radial-field topologies,” IEEE Trans. on Magnetics, vol. 31, no. 3, pp. 1912–1915 (1995)

[41] David C. Lay, Steven R. Lay, Judi J. McDonald, “Linear Algebra”, Fifth Edition, pp. 114~120, 2016

[42] Katsuya Yoneyama, Kan Akatsu, “Operating point estimation for permanent magnet of electric motor under load-condition”, 2016 19th International Conference on Electrical Machines and Systems (ICEMS), Nov. 2021.

[43] Minho Jang, Kan Akatsu, “The Magnet Operating Point Estimation using Motor Parameter Estimation and Magnetic Equivalent Circuit in PMSM”, 2020 IEEE 9th International Power Electronics and Motion Control Conference (IPEMC2020-ECCE Asia), pp. 73–78, 2020.

[44] Minho Jang, Kan Akatsu, “The Magnet Operating Point Estimation using Thermal Component Ratio Observer in PMSM”, 2021 IEEE 12th Energy Conversion Congress & Exposition - Asia (ECCE-Asia), pp. 526–530, 2021.

Research Achievement

■ Journal Paper

(1) Minho Jang, Kan Akatsu, “Magnet Operating Point Estimation Using Flux Linkage Observer and Magnetic and Thermal Equivalent Circuit in PMSM”, IEEJ Journal of Industry Applications, vol., pages, Accepted on July 21, 2021

■ International Conference (with review)

(2) Minho Jang, Kan Akatsu, “The Magnet Operating Point Estimation using Motor Parameter Estimation and Magnetic Equivalent Circuit in PMSM”, 2020 IEEE 9th International Power Electronics and Motion Control Conference (IPEMC2020-ECCE Asia), pp. 73–78, 2020.

(3) Minho Jang, Kan Akatsu, “The Magnet Operating Point Estimation using Thermal Component Ratio Observer in PMSM”, 2021 IEEE 12th Energy Conversion Congress & Exposition - Asia (ECCE-Asia), pp. 526–530, 2021.